Abstract

Title of Dissertation: A Search for First Generation Scalar Leptoquarks at $\sqrt{s} = 1.8$ TeV with the DØ Detector

Douglas Milton Norman, Doctor of Philosophy, 1993

Dissertation directed by: Nick Hadley, Associate Professor, Department of Physics

A search for first generation scalar leptoquarks was done at the DØ detector at Fermi National Accelerator Laboratory from 15 pb^{-1} of data taken during the 1992-1993 collider run. At Fermilab's $p\bar{p}$ collider with a center-of-mass energy of 1.8 TeV, leptoquarks are produced mostly by the strong force in pairs. Leptoquarks carry fractional charge, color, and also lepton and baryon quantum numbers. First generation leptoquarks couple exclusively to the electron, electron neutrino, and the u and d quarks; such a leptoquark would decay into, for example, an electron plus a quark. Signatures for leptoquarks at $p\bar{p}$ colliders that have been investigated at DØ are two electrons plus two jets and one electron plus missing energy (from an electron neutrino) plus two jets.

The dominant backgrounds for these channels are Z° plus two jet and Drell Yan γ^{*} plus two jet events for the two electron leptoquark signal and W plus two jet events for the electron plus missing energy leptoquark signal. After eliminating these and other smaller backgrounds from the data samples, no leptoquark signal was observed. A lower limit on the mass of a first generation leptoquark was determined to be 139 GeV/c^2 for the 100% branching of the leptoquark into electron plus quark and 129 GeV/c^2 for the 50% branching into electron plus quark.

A Search for First Generation Scalar Leptoquarks at $\sqrt{s} = 1.8$ TeV with the DØ Detector

by

Douglas Milton Norman

Dissertation submitted to the Faculty of the Graduate School
of The University of Maryland in partial fulfillment
of the requirements for the degree of
Doctor of Philosophy
1993

Advisory Committee:

Associate Professor Nicholas J. Hadley, Chairman/Advisor
Assistant Professor Andrew Baden
Associate Professor Abolhassan Jawahery
Professor Jogesh C. Pati
Professor Andrew S. Wilson

Dedication

to my parents

Garland P. and Martha A. Norman

Acknowledgements

There are many people who have helped me to this apex of my academic career that I would like to thank. I feel fortunate for having Nick Hadley for my advisor. I thank him for his guidance and advice. I'd like to thank Kathy Streets, Amber Boehnlein and Marc Paterno for getting me through some tough times with DØ 's software as well as lending me their ears from time to time. I'd like to thank Wyatt Merritt for her enormous efforts in getting the data filtered into workable subsets and for her help with the analysis. Amber Boehnlein and Bill Cobau were very helpful in proofing this thesis, and I'd like to thank them for taking the time to read it. I'd like to thank Drew Baden, Hassan Jawehery, Jogesh Pati, and Andrew Wilson for serving on my dissertation committee. I'd like to thank to the entire DØ collaboration for a job well done. Without Fermi National Accelerator Laboratory the DØ experiment could not exist; therefore, I thank Fermilab and its staff for their support. And finally, I wish to express my appreciation for the support from my family.

Contents

Section **Page**

1 Introduction **1**

1.1 Theory 5

1.1.1 The Leptoquark Coupling and Single Production 6

1.1.2 Pair Production 9

1.2 Leptoquark Signatures 20

1.3 Experimental Limits So Far 21

2 The DØ Detector **23**

2.1 Vertex Detector 26

2.2 Transition Radiation Detector 29

2.3 Tracking 31

2.3.1 Central Tracking 32

2.3.2 Forward Tracking 33

2.4 Calorimetry 35

2.4.1 Central Calorimeter 36

2.4.2 End Calorimeter 39

2.4.3 Inter Cryostat Detector 41

2.4.4 Calorimeter Electronics and Signal Routing 42

2.5 Muon Detector 44

2.5.1 Wide Angle Muon Spectrometer 45

2.5.2 Small Angle Muon Spectrometer 48

2.6 Level 0 Hodoscopes 49

3 Calibration of Calorimeter **51**

3.1 Response 54

3.2 Energy Resolution 60

3.3 Position Resolution for Electrons and Pions 63

3.4 e/π Ratio 64

3.5 Shower Shape 65

3.6 Systematics and the Transferring the Calibration 68

3.7 Summary of Calorimeter Calibration 70

4 Data Selection **71**

4.1 The DØ Trigger and Filter Scheme 72

4.1.1 Level One 73

4.1.2 Level Two 75

4.1.3 Triggers Used for Leptoquark Search 79

4.2 Measurement of Electrons, Jets, and $\not{E}_T$ 80

4.2.1 Electrons 81

4.2.2 Jets 85

4.2.3 Missing Transverse Energy 88

4.3 Off-line Selection 90

5 Analysis **99**

5.1 Monte Carlo 100

5.1.1 Distributions for Electrons, Jets, and $\not{E}_T$ 101

5.2 Efficiencies for a Leptoquark Signal 106

5.2.1 Trigger Efficiencies 107

5.2.2 Reconstruction Efficiencies 110

5.3 Error Analysis 126

5.4 Upper Limit on leptoquark Cross Section 128

5.5 Lower Limit on Leptoquark Mass 129

5.6 Backgrounds 135

5.6.1 Monte Carlo Generated Backgrounds 137

5.6.2 Background Studies from Data 139

5.6.3 Summary of Backgrounds 141

6 Conclusion **142**

A Parameterization of the Longitudinal Development of Hadron Showers in the D0 Calorimeter **144**

List of Tables

Number **Page**

1.1 Standard Model elementary particles 1

4.1 Level One and Level 1.5 variables 74

4.2 List of trigger used and their terms 80

4.3 Off-line cuts used for the two electron plus two jet sample . . . 94

4.4 Off-line cuts used for one electron plus $\not\!\!E_T$ plus two jet sample . 98

5.1 Level One plus Level Two trigger kinematic efficiencies expressed as percent; errors are about 1% 108

5.2 The total trigger efficiencies in percent for the two electron and electron plus $\not\!\!E_T$ signal searches 110

5.3 Parameters for the fit of the Breit-Wigner function to two electron data for various electron quality cuts 113

5.4 Parameters for the fit of Breit-Wigner to two electron data with reduced number of parameters 115

5.5 Efficiency for electron quality cuts applied to both electrons in the two electron sample given in percent 116

5.6 Parameters of fit of equation 5.2 to two electron and one electron plus one photon data 117

5.7 Parameters from refit of equation 5.2 to the two electron and one electron plus one photon data with reduced number of parameters 117

5.8 The fraction of events in the R < 0.7 part of the W sample with detector background cuts and 20 GeV E_t cut on electron, jets and $\not{E}_T$ for each successive quality cut and efficiency for each cut 121

5.9 The (off-line and trigger) kinematic efficiency for leptoquark samples with weighting of portions of samples according to geometric isolation of electrons 124

5.10 Final efficiencies with total statistical errors for the leptoquark signal samples 125

5.11 Total errors for leptoquark signal samples in percent 127

5.12 The upper limit at a 95% CL for the number of events expected and the leptoquark production cross section times β^2 for each two electron plus two jet signal samples and the leptoquark production cross section times $2\beta(1-\beta)$ for the electron plus $\not{E}_T$ plus two jet signal samples 130

5.13 Lower limits on the mass of the leptoquark for various values of the branching ratio β 134

A.1 Fitted parameters at various energies 150

A.2 Parameter $= C_1 + C_2 \times E + C_3 \times E^2 + C_4 \times E^3$ 150

List of Figures

Number **Page**

1.1 Single leptoquark production in $p\bar{p}$ collision 7

1.2 Decay of $\pi^+ \rightarrow e^+\nu$ 9

1.3 Pair production of leptoquarks in $p\bar{p}$ collisions 10

1.4 Gluino t-channel exchange in the pair production of squarks . . 11

1.5 Squark pair production cross section vs mass of gluino, mass of squark=50 GeV/c^2 14

1.6 Squark pair production cross section vs mass of gluino, mass of squark=80 GeV/c^2 15

1.7 Squark pair production cross section vs mass of gluino, mass of squark=90 GeV/c^2 15

1.8 Squark pair production cross section vs mass of gluino, mass of squark=100 GeV/c^2 16

1.9 Squark pair production cross section vs mass of gluino, mass of squark=120 GeV/c^2 16

1.10 Squark pair production cross section vs mass of gluino, mass of squark=140 GeV/c^2 17

1.11 Squark pair production cross section vs mass of gluino, mass of squark=160 GeV/c^2 17

1.12 Leptoquark pair production cross section (Normalized to the cross section calculated with EHLQ1 structure functions) vs mass of the leptoquark for several structure function sets 19

2.1 The DØ Detector 27

2.2 The DØ Vertex Detector 28

2.3 The DØ TRD 31

2.4 The Forward Drift Chambers 34

2.5 The DØ Calorimeter 37

2.6 The DØ Calorimeter: plate level structure 39

2.7 The DØ ICD detector mounted on an EC 42

2.8 Side View of DØ Detector 45

2.9 The DØ Muon Detector: WAMUS PDT cross section 47

2.10 One plane of a DØ Hodoscope 49

3.1 Load One Configuration; beam coming from the left 52

3.2 Load Two Configuration 53

3.3 Uniformity of Response of Load One for Pions: a)Response vs η, b)Response vs ϕ 59

4.1 Invariant mass distribution of two electron data sample with 25 GeV cut on the electrons 92

4.2 Invariant mass distribution of two electron data sample with 25 GeV cut on the electrons and jets 93

4.3 Transverse mass distribution of electron-$\not\!\!E_T$ data sample with 20 GeV E_t cut on electron, 20 GeV cut on $\not\!\!E_T$, and two jets with E_t of 15 and 10 GeV 96

4.4 Transverse mass distribution of electron-$\not\!\!E_T$ data sample with 20 GeV E_t cut on electron and two jets and 40 GeV E_t cut on $\not\!\!E_T$ 97

5.1 The 100 GeV, two electron plus two jet, Monte Carlo and two electron data distributions for the first two highest E_t electrons and jets 103

5.2 The 100 GeV, one electron plus $\not\!\!E_T$ plus two jet, Monte Carlo and electron plus $\not\!\!E_T$ data distributions for electron, $\not\!\!E_T$, and first two highest E_t jets 104

5.3 The invariant and transverse masses for the respective two electron and electron plus $\not\!\!E_T$, 100 GeV, Monte Carlo leptoquark and data samples 105

5.4 Breit-Wigner fit of two electron data before electron quality cuts 112

5.5 Breit-Wigner fit of two electron data after electron quality cuts . 112

5.6 Z° mass plots used in tracking efficiency study: a) Two electron invariant mass distribution, b) One electron plus one photon invariant mass distribution 118

5.7 The upper limit on the cross section for the pair production of scalar leptoquarks for a 100% branching into electrons, $\beta = 1.0$, (for the two electron signature) vs the mass of the leptoquark is plotted as the solid line. Also plotted is the theoretical cross section as the dashed line. 131

5.8 The upper limit on the cross section for the pair production of scalar leptoquarks for $\beta = 0.5$ (for the electron - $\not\!\!E_T$ signature) vs the mass of the leptoquark is plotted as the solid line. Also plotted is the theoretical cross section as the dashed line. 133

5.9 The branching ratio of leptoquark into electron plus jet vs leptoquark mass excluded region 136

A.1 Distribution of shower origins as a function of interaction lengths 146

A.2 Distribution of shower length rescaling factors: a) f_1, b) f_2 . . . 147

A.3 Values of the parameters A, C and D as a function of energy . . 149

A.4 Longitudinal development of hadronic shower 151

A.5 IH layer one: comparison of data and parameterization 153

A.6 IH layer two: comparison of data and parameterization 153

Chapter 1

Introduction

Establishing symmetries plays a major part in the modeling of the physical universe. Symmetries can be seen in biological systems such as the patterns in flowers or the double helix structure of the DNA molecule. The structure of crystals of ionic compounds also exhibit many types of symmetry. There seems to be explicit symmetries on many of the size scales of matter; this is apparent on the scale of elementary particles. These particles can be classified as in table 1.1. The electron and the lightest two quarks, u and d, of the first

Table 1.1: Standard Model elementary particles

Fermion: Spin = 1/2			
Leptons	e, ν_e	μ ,ν_μ	τ ,ν_τ
Quarks	u, d	s, c	b, t
Boson: Spin= 0,1			
Spin=0	H°		
Spin=1	Z°, γ	$W^\pm$	g^i, i=1,8

family of fermions make up normal matter with small contributions from the other quarks only in the form of virtual $q\bar{q}$ pairs. These higher mass quarks s, c, b, and t are found as single valence partons in unstable hadronic matter such as mesons or heavy baryons produced in high energy interactions. The heavier leptons are also produced directly in high energy interactions or the subsequent decay of heavy baryons or mesons. The spin 1 bosons mediate the forces between the fermions. The neutral ($\Delta Q=0$) current interactions are mediated by the Z° and γ (photon); the Z° mediates weak interactions, and the γ mediates electromagnetic interactions. The $W^\pm$ mediate the charged weak current interactions. And the eight gluons, g^i, mediate the strong or 'color' [1] force between the quarks, which have 'color' charges. This color force binds three quarks of different colors inside colorless baryons like protons or neutrons. It also binds one quark and one antiquark of a given color and anti-color respectively inside of colorless mesons. A colorless particle does not experience the strong force; however, the nuclear binding force between protons and neutrons, for example, can be considered a type of Van der Waals derivative of the strong force. Of the particles in table 1.1 the H°, the t quark, and the tau neutrino have not yet been observed directly. Only the particles in table 1.1 and their charge conjugates are present in the Standard Model.

[1] Color is a designation for the book keeping of a quantum number and has nothing to do with spectral color.

The Standard Model (SM) [1] is based on the symmetry group SU(2)$\otimes$U(1)$\otimes$SU(3). Each subgroup is associated with a quantum number(s) or generator(s) of that group. SU(2)'s generators are the three components of the isospin 'charge' (I), which in the fundamental representation of the SU(2) group can be represented by the Pauli matrices. The good or conserved quantum numbers are $I = 1/2$ and $I_3 = \pm 1/2$. These SU(2) generators basically map one I_3 state into the other or itself. The generator of the U(1) group is called the hypercharge (Y) which is a conserved quantum number since Y only produces a shift in the phase of the state function, $\psi \rightarrow e^{iY\alpha}\psi$. The electric charge (Q) is equal $I_3 + \frac{Y}{2}$ which is therefore conserved. The SU(2)$\otimes$U(1) part of the SM describes the interactions between particles with electric and/or weak charges. The SU(3) group describes the strong interactions among colored particles such as quarks and is usually termed as $SU(3)_{color}$. Quarks are assigned one of three colors, hence the use of the SU(3) group. One convention is red, green, and blue. A combination of one each of the three colors is colorless as in the proton. There are eight generators in the fundamental representation of this group, and the generators can be represented by what are known as the Gell-Mann matrices, which map one color state into another color state or into the same state. Each of the generators of the SU(2)$\otimes$U(1)$\otimes$SU(3) symmetry represent a mediating 'particle' which mediates the forces between the state functions representing fermion matter particles. Each of the mediating

'particles' is represented by a massless spin = 1 field. These massless fields in the SU(2)$\otimes$U(1) sector of the SM do not represent the physical particles which mediate the forces in this subgroup; not all of the physical particles are massless. To generate the physical fields, a mechanism known as spontaneous symmetry breaking is invoked.

The scalar boson H° in table 1.1 is the Higgs boson, and it is responsible for the symmetry breaking of the SU(2)$\otimes$U(1) part of the SM. This symmetry breaking starts with the introduction of a massless scalar particle ϕ. This field is introduced with a kinematic interaction term and a symmetric potential term which are added to the SU(2)$\times$U(1) part of the SM interaction Lagrangian. The parameters of the potential are then selected so that the potential's symmetry is 'broken'. The scalar field ϕ then acquires a non-zero vacuum expectation value. This symmetry breaking generates the masses of the spin = 1 bosons with the exception of the gluons through the coupling of the scalar ϕ to these spin = 1 bosons in the kinematic interaction term of the scalar ϕ, and it generates the the masses of the fermions through Yukawa couplings between the fermions and the massless scalar ϕ, which after symmetry breaking acquires the Higgs mass. The masses of the fermions and bosons are not explicitly determined in the theory of the SM since they are expressed in terms of the unknown vacuum expectation value of the broken Higgs field and the unknown Yukawa and gauge coupling strengths; only the mechanism for

their generation is provided. The unknown parameters need to be provided by experimental data.

In the nomenclature of elementary particles described in table 1.1, there seems to be a symmetry between the leptonic sector and the quark sector. In the SM if one applies a symmetry group such as SU(2)$\otimes$U(1) to the members of the quark sector, the same symmetry group can be applied to the leptonic sector because, in a given family, the number of quark species is equal to the number of lepton species. This symmetry leads, for example, to the cancellation of anomalies such as triangular anomalies found in chiral theories. This implies that there may exist some coupling between the leptons and quarks, and there may exist a mediating particle that couples particles from one sector to the other. This thesis describes a search for a first generation leptoquark, as these particles have been called, that couple to electrons, electron neutrinos, and u and d quarks.

1.1 Theory

Leptoquarks are found in many models beyond the SM. They appear as bound states of leptons and quarks in some models based on the SU(4) symmetry group [2]. They also appear in SU(5) symmetry based models, in supersymmetry, GUTs, technicolor, and superstring models as hybrid particles [3] [4] [5]. Leptoquarks have a variety of model dependent quantum numbers. Some of

these numbers include spin = 0, 1, or 2, electric charge = $-\frac{4}{3}$, $-\frac{1}{3}$, $\frac{2}{3}$, or $\frac{5}{3}$, isospin = 0, $\frac{1}{2}$, or 1, lepton number ± 1, and baron number $\pm\frac{1}{3}$. In what follows only the spin = 0 case will be presented; this is the simplest case and is most common in the literature.

1.1.1 The Leptoquark Coupling and Single Production

The production of single scalar leptoquarks in hadron-hadron colliders occurs through the reaction depicted in figure 1.1. The leptoquark-lepton-quark vertex has the general form show in equation 1.1 with the unknown couplings λ_1^{ij} and λ_2^{ij}. The indices i, j represent the generations of quarks and leptons.

$$\mathcal{L} = \bar{l}^i(\lambda_1^{ij} + \lambda_2^{ij}\gamma_5)q^j S + H.C. \tag{1.1}$$

With $(g^{ij})^2 = \mid \lambda_1^{ij} \mid^2 + \mid \lambda_2^{ij} \mid^2$, the coupling can be scaled to the electromagnetic coupling e , ie. $(g^{ij})^2/4\pi = k\alpha$. Limits on the value of this coupling have been determined. By calculating the 5% deviation in the $e^+e^- \rightarrow q\bar{q}$ predicted total cross section and forward - backward asymmetry due to the contribution of a t channel exchange of a leptoquark, the authors of reference [6] give a constraint on the value of the mass of the leptoquark as a function of the parameter k. For a value of k equal one, leptoquarks are ruled out for masses less than about 300 GeV/c^2. For a value of k equal 0.5, leptoquarks are ruled out for masses less than about 200 GeV/c^2. Leptoquark masses less than 50 GeV/c^2

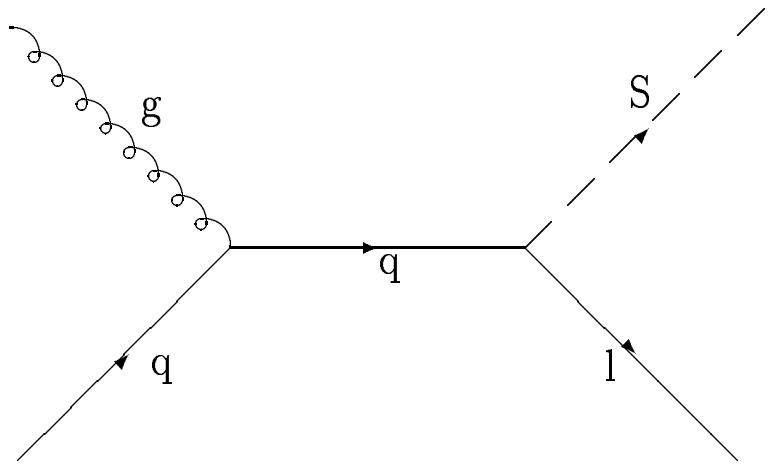

Figure 1.1: Single leptoquark production in $p\bar{p}$ collision

can be ruled out if one assumes a value of k of 0.045. In order for leptoquarks to be detected at DØ with optimal efficiency, the leptoquarks need to decay before they travel about 1 mm after they are produced. This translates to a lower bound on k of about 10^{-12} for detection at DØ.

The existence of leptoquarks that couple unconstrained to any lepton-quark pair would produce flavor changing neutral currents such as $\pi^0 \to \mu^{\pm} e^{\mp}$, and give large contributions to decays such as $K^{\pm} \to e\nu$, $\pi^{\pm} \to e\nu$, and $K^{+} \to \pi^{+}\nu\bar{\nu}$. This would then require severe constraints on the leptoquark mass. To relax this mass constraint, the coupling can be constrained as follows. Consider the decay represented in figure 1.2. Equation 1.1 can be rewritten in the Dirac-Pauli representation.

$$\mathcal{L} = \bar{l}_{R,L} \begin{pmatrix} \lambda_1 & \lambda_2 \\ \lambda_2 & \lambda_1 \end{pmatrix} q_{R,L} S + h.c. \tag{1.2}$$

$$\bar{l}_{R,L} = \bar{l}(1 \mp \gamma_5)$$

$$q_{R,L} = (1 \pm \gamma_5)q$$

Here the E>>m limit is assumed. If the incoming quark and the outgoing lepton are of the same helicity state, then $\mathcal{L}$ for that vertex is zero. Taking the case of figure 1.2, the $u_R - S - \nu_L$ vertex has an amplitude of

$$\bar{U}_{\nu_L} \begin{pmatrix} \lambda_1 & \lambda_2 \\ \lambda_2 & \lambda_1 \end{pmatrix} U_{u_R} S = \frac{1}{2} \bar{U}_\nu \begin{pmatrix} \lambda_1 + \lambda_2 & \lambda_1 + \lambda_2 \\ \lambda_1 + \lambda_2 & \lambda_1 + \lambda_2 \end{pmatrix} U_u \, S \tag{1.3}$$

and the $\bar{d}_R - S - e_L^+$ vertex has the amplitude

$$\bar{V}_{e_L^+} \begin{pmatrix} \lambda_1 & \lambda_2 \\ \lambda_2 & \lambda_1 \end{pmatrix} V_{d_R} S = \frac{1}{2} \bar{V}_{e^+} \begin{pmatrix} \lambda_1 - \lambda_2 & \lambda_1 - \lambda_2 \\ \lambda_1 - \lambda_2 & \lambda_1 - \lambda_2 \end{pmatrix} V_d \, S \tag{1.4}$$

Therefore, to suppress such decays the leptoquark couplings can be restricted to chiral couplings, i.e. $\lambda_1 = \lambda_2$ or $\lambda_1 = -\lambda_2$. In addition to this restriction, generation mixing can be forbidden, i=j for λ^{ij}, and a given leptoquark can be restricted to couple to only one generation.

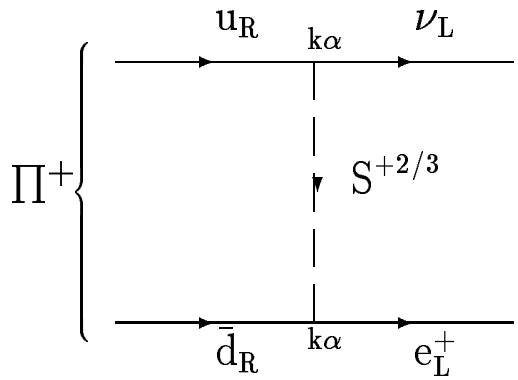

Figure 1.2: Decay of $\pi^+ \rightarrow e^+\nu$

1.1.2 Pair Production

Pair production of leptoquarks in $p\bar{p}$ colliders occurs through the interactions depicted in figure 1.3. The quark and gluon fusion processes do not depend on the unknown coupling of the leptoquark; however, the lepton exchange process does. Provided that the coupling is small, single leptoquark production and pair production via lepton t-channel exchange can be ignored. This is the case for leptoquark masses up to about 200 GeV/c^2, which is roughly the upper limit for discovery at the Fermilab Tevatron with center of momentum energy of 1800 GeV, within the next five years before Fermilab's main injector comes on-line, which will boost the instantaneous luminosity. Therefore, for the purposes of calculating the cross section for leptoquark production, only gluon and quark fusion processes will be considered.

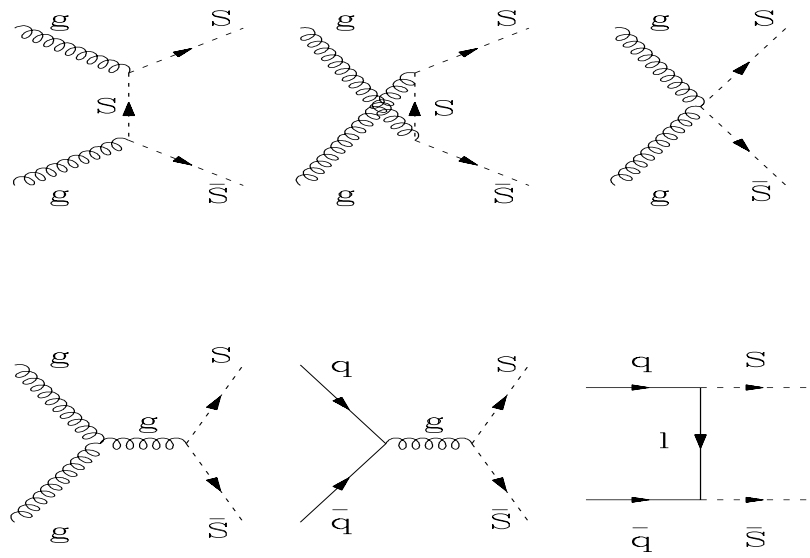

Figure 1.3: Pair production of leptoquarks in $p\bar{p}$ collisions

The pair production of all scalar color triplet particles in $p\bar{p}$ collisions are similar. The gluon fusion and quark-antiquark annihilation processes of figure 1.3 are the same for squark-antisquark pair production. In addition to these processes for squark production, however, is the possibility of gluino exchange as seen in figure 1.4.

The production cross section for supersymmetric squarks have been calculated [7] [8]. Rewriting the formula in reference [8], the contributions to the cross section are as follows. For gluon fusion the cross section is

$$\hat{\sigma}^1 = \frac{F\pi\alpha_{\hat{s}}^2}{3\hat{s}}\left[\left(\frac{5}{8}+\frac{31\,m^2}{4\,\hat{s}}\right)\zeta+\left(4+\frac{m^2}{\hat{s}}\right)\frac{m^2}{\hat{s}}\ln\left(\frac{1-\zeta}{1+\zeta}\right)\right] \tag{1.5}$$

$$\zeta = \sqrt{1-4\frac{m^2}{\hat{s}}}.$$

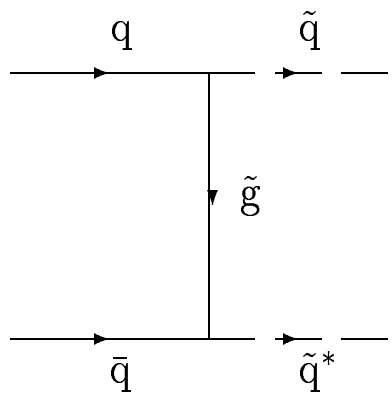

Figure 1.4: Gluino t-channel exchange in the pair production of squarks

Here m is the mass of the squark and F is the number of squark flavors. The quark scattering contribution to the cross section where the quark and antiquark are of the same flavor is

$$\begin{aligned}
\hat{\sigma}^2 &= \frac{4\pi\alpha_{\hat{s}}^2}{9\hat{s}}\left[\left(1-\frac{2\delta}{\hat{s}}-\frac{2}{3}\frac{\delta^2}{\hat{s}^2}-\frac{2}{3}\frac{M_{\tilde{g}}^2}{\hat{s}}\right)\ln\left(\frac{\hat{s}(1+\zeta)-2\delta}{\hat{s}(1-\zeta)-2\delta}\right)+\right. \\
&\quad \left.\zeta\left(\frac{F-5}{3}-\frac{4}{3}F\frac{m^2}{\hat{s}}-\frac{2}{3}\frac{\delta}{\hat{s}}+\frac{\hat{s}M_{\tilde{g}}^2}{\delta^2+\hat{s}M_{\tilde{g}}^2}\right)\right] \qquad (1.6) \\
\delta &= m^2-M_{\tilde{g}}^2.
\end{aligned}$$

When the quark and antiquark are of different flavors the contribution is

$$\hat{\sigma}^3=\frac{4\pi\alpha_{\hat{s}}^2}{3\hat{s}}\left[\left(1-\frac{2\delta}{\hat{s}}\right)\ln\left(\frac{\hat{s}(1+\zeta)-2\delta}{\hat{s}(1-\zeta)-2\delta}\right)+\zeta\left(\frac{\hat{s}M_{\tilde{g}}^2}{\hat{s}M_{\tilde{g}}^2+\delta^2}-2\right)\right]. \qquad (1.7)$$

$M_{\tilde{g}}^2$ in equations 1.6 and 1.7 is the gluino mass. The formula found in reference [7] are the same or very similar. If the mass of the gluino is set to a large enough value, the gluino t-channel exchange contribution to the above cross sections is suppressed, and the squark pair production cross section with F=1 is equal to twice the leptoquark pair production cross section. The factor of two arises from the left-right handed squark mass degeneracy assumed in the above cross sections.

The above cross sections can be folded with the proton structure functions using the following equation[2] [9]:

$$\begin{aligned}
\sigma &= \sum_{a,b} \int_0^1 d\tau \int_\tau^1 \frac{dx_a}{x_a} \left[f_{a/A}(x_a, \hat{s}) f_{b/B}(\tau/x_a, \hat{s}) \right. \\
&\quad \left. + (A \leftrightarrow B; a \neq b) \right] \hat{\sigma}(\hat{s}) \qquad (1.8) \\
\tau &= x_a x_b \\
\hat{s} &= x_a x_b s = \tau s
\end{aligned}$$

where x_a and x_b are the Feynman x's, $a = x_a A$ and $b = x_b B$. A, B indicate the proton or antiproton and their 4-momentum, and a and b are the associated

[2] The color-averaging factor found in reference [9] is not included in equation 1.8 since the above cross sections have been averaged over initial and final state colors.

parton's 4-momentum. The center of mass energy of the $p\bar{p}$ system is $\sqrt{s}$. Hence, the total cross section can be written

$$\sigma = \sum_{n=1}^{3} \int_0^1 d\tau \int_\tau^1 \frac{dx}{x} \left[f^n(x,\hat{s}) f^n(\tau/x,\hat{s}) \right] \hat{\sigma}^n(\hat{s}) \tag{1.9}$$

$$f^1(x,\hat{s}) f^1(y,\hat{s}) = g(x,\hat{s}) g(y,\hat{s}) \tag{1.10}$$

$$\begin{aligned} f^2(x,\hat{s}) f^2(y,\hat{s}) &= u(x,\hat{s}) u(y,\hat{s}) + d(x,\hat{s}) d(y,\hat{s}) + \\ & 2st(x,\hat{s}) st(y,\hat{s}) + 2sea(x,\hat{s})\, sea(y,\hat{s}) \end{aligned} \tag{1.11}$$

$$\begin{aligned} f^3(x,\hat{s}) f^3(y,\hat{s}) &= u(x,\hat{s}) d(y,\hat{s}) + d(x,\hat{s}) u(y,\hat{s}) + \\ & u(x,\hat{s}) st(y,\hat{s}) + st(x,\hat{s}) u(y,\hat{s}) + \\ & d(x,\hat{s}) st(y,\hat{s}) + st(x,\hat{s}) d(y,\hat{s}) + \\ & 2sea(x,\hat{s}) st(y,\hat{s}) + 2st(x,\hat{s}) sea(y,\hat{s}) + \\ & 2sea(x,\hat{s})\, sea(y,\hat{s}) \end{aligned} \tag{1.12}$$

Here $g(x,\hat{s})$, $u(x,\hat{s})$, $d(x,\hat{s})$, $st(x,\hat{s})$, and $sea(x,\hat{s})$ are respectively the gluon, up, down, strange, and sea, Q^2-dependent, distributions for the proton. $sea(x,\hat{s})$ is equal the sea distribution of u, and d; sea = u_{sea} = d_{sea}. $u(x,\hat{s})$ and $d(x,\hat{s})$ are actually the sum of valence and sea distributions.

Equation 1.9 was numerically integrated using the EHLQ set one structure functions [10]. For $\sqrt{s}$ = 1800 GeV and F = 2, the total cross section plotted

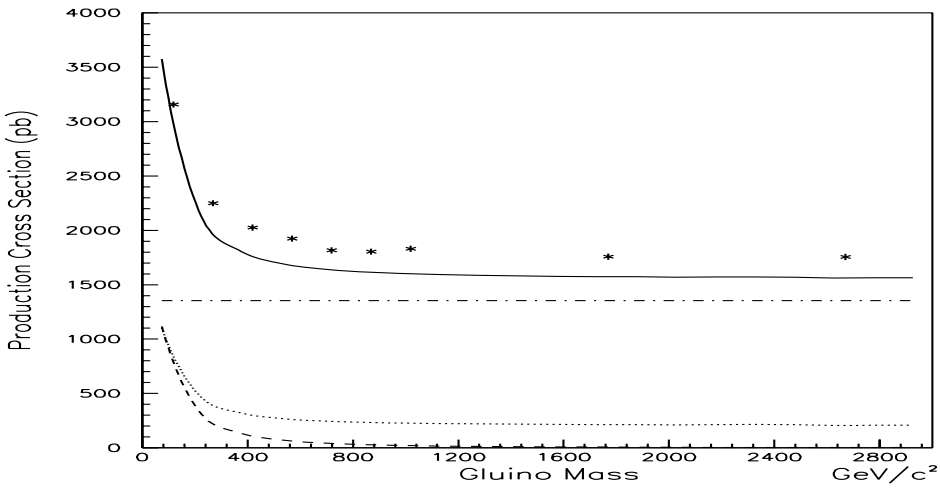

Figure 1.5: Squark pair production cross section vs mass of gluino, mass of squark=50 GeV/c^2

against the gluino mass for several values of the squark mass is given in figures 1.5 - 1.11. The horizontal dot-dashed line is the gluon fusion contribution to the total cross section which is represented by the solid line. The dotted line is the contribution from quark-antiquark scattering (annihilation) where the quarks are of the same flavor, and the dashed line represents scattering of quarks of different flavors. The asterisk are the cross sections calculated by ISAJET [11], which is a Monte Carlo physics generator; see the section on Monte Carlo in chapter 5. The structure functions used in ISAJET were EHLQ set one. These ISAJET values have an uncertainty of about seven percent.

It can be seen from figures 1.5–1.11 that at the lower values of squark (leptoquark) mass, the major contributor to the total pair production is gluon fusion.

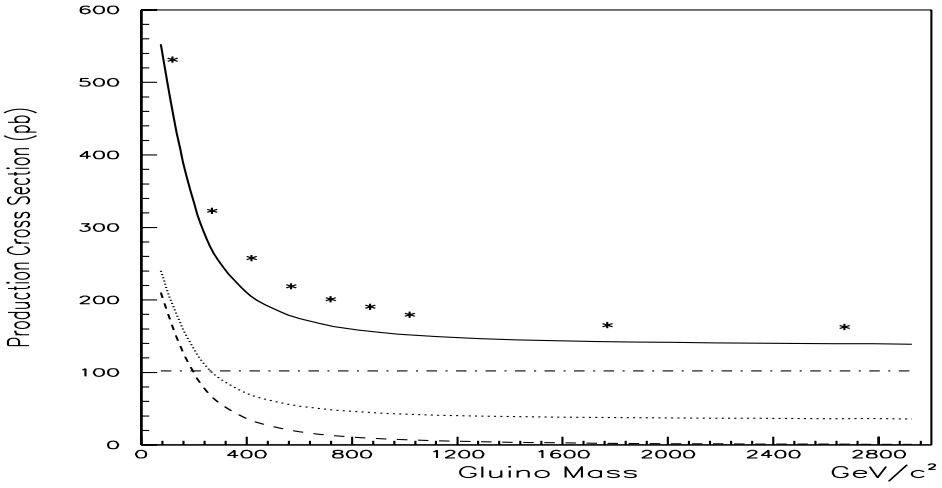

Figure 1.6: Squark pair production cross section vs mass of gluino, mass of squark=80 GeV/c^2

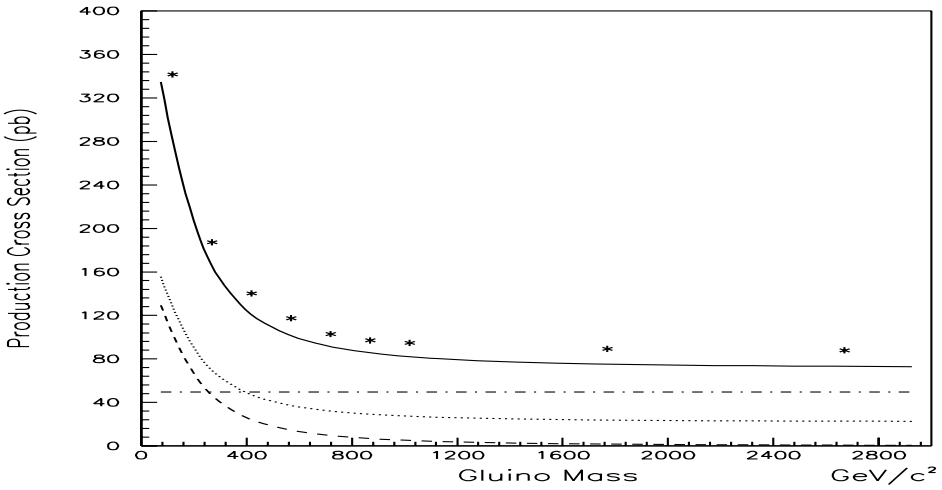

Figure 1.7: Squark pair production cross section vs mass of gluino, mass of squark=90 GeV/c^2

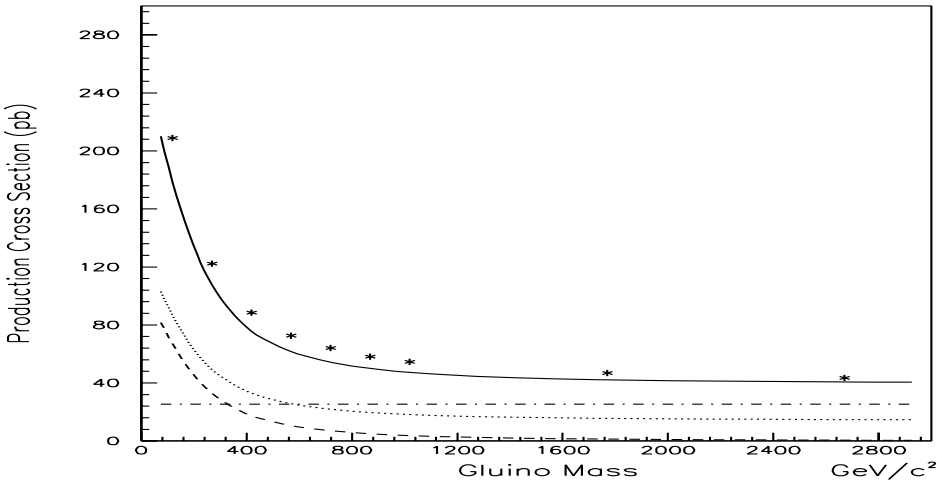

Figure 1.8: Squark pair production cross section vs mass of gluino, mass of squark=100 GeV/c^2

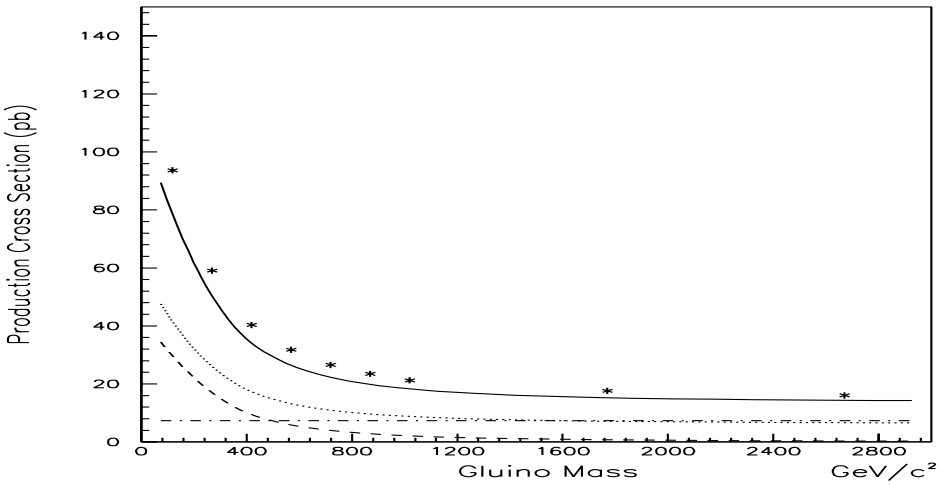

Figure 1.9: Squark pair production cross section vs mass of gluino, mass of squark=120 GeV/c^2

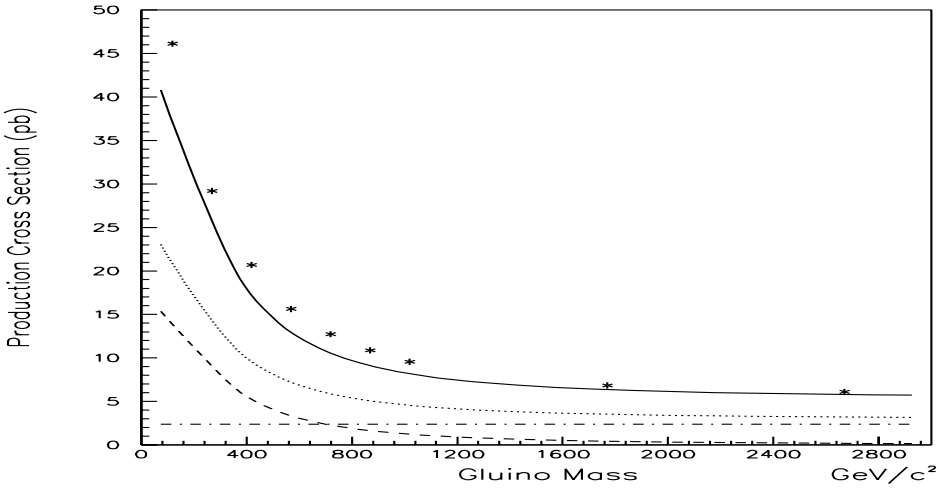

Figure 1.10: Squark pair production cross section vs mass of gluino, mass of squark=140 GeV/c^2

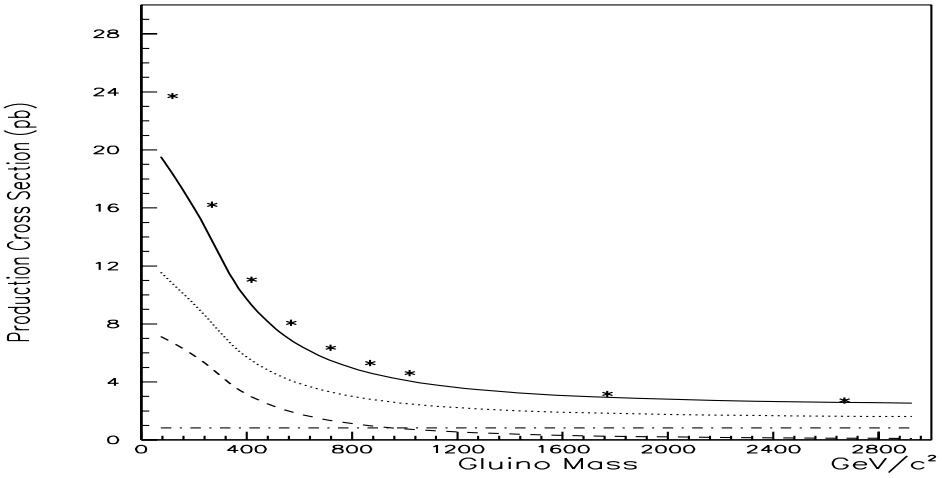

Figure 1.11: Squark pair production cross section vs mass of gluino, mass of squark=160 GeV/c^2

Gluon fusion becomes the minor contributor compared to quark-antiquark annihilation at larger values of the squark mass. It is also apparent that the contribution from the scattering of two quarks of different flavors becomes insignificant at large gluino masses; this process occurs only through the exchange of a gluino. The cross section is reasonably constant above a gluino mass of 2000 GeV/c^2. The ISAJET calculated cross section agrees well with the calculation described above with a $\leq 15\%$ difference in the values.

The cross sections were also calculated using more recent and better next to leading order structure functions calculated with the Next Leading Log (NLL) method. The normalized cross section verses squark mass for the Morfin and Tung set one (MTS1), Glück *et al* (GRVH0), and Kwiecinski *et al* (KMRSB0) structure functions is given in figure 1.12. Calculations with the Eichten *et al* sets one and two (EHLQ1 and EHLQ2) and the Duke and Owen set one (DO1) structure functions are also plotted as representatives of leading order calculations. All of the cross sections in figure 1.12 were normalized to the cross section calculated with the EHLQ set one structure functions. At the lower leptoquark masses, considering the next leading order calculations, the uncertainty in the cross section due the uncertainty in the structure functions is around 20%. The uncertainty decreases to about 5% at the higher masses.

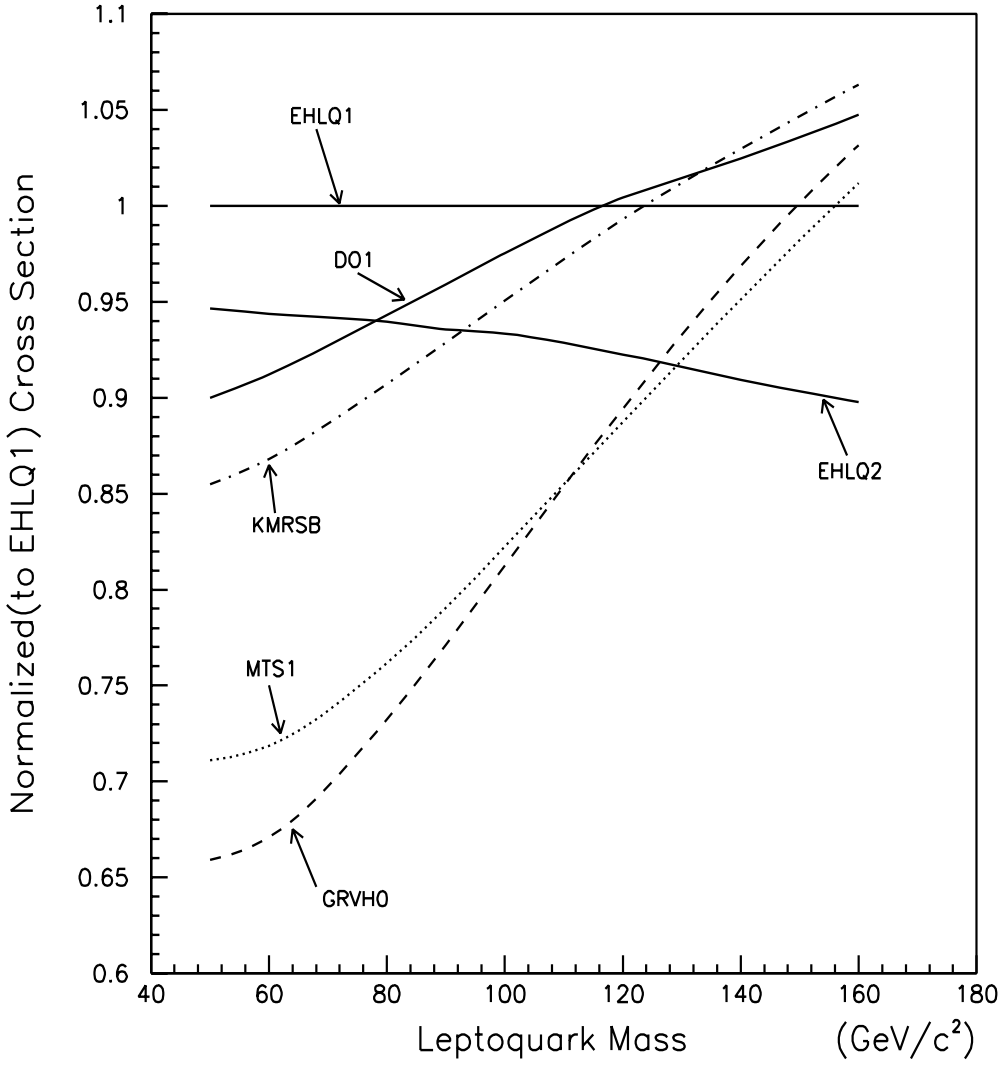

Figure 1.12: Leptoquark pair production cross section (Normalized to the cross section calculated with EHLQ1 structure functions) vs mass of the leptoquark for several structure function sets

1.2 Leptoquark Signatures

Since leptoquarks are produced predominantly in pairs at $p\bar{p}$ colliders, there are three distinct signals that can be looked for in a search for a first generation leptoquark. A first generation leptoquark as discussed above is restricted to couple to electrons, electron neutrinos, and the u and d quarks. Therefore, the expected signal for pair produced leptoquarks would be two electrons plus two jets, one electron plus missing transverse energy ($\not{E}_T$) plus two jets, or $\not{E}_T$ plus two jets. The electrons, jets, and $\not{E}_T$ should all be generally isolated from each other. The major background contribution to the two electron plus two jet leptoquark signal is Z° plus two jet events. The dominant background for the electron plus $\not{E}_T$ plus two jet leptoquark signal is W plus two jet events. The backgrounds to the $\not{E}_T$ plus two jets are numerous and very hard to eliminate. This last signal will not be considered in this analysis.

The percentage of leptoquark events that might be seen with the various signatures depends on the branching ratio of the leptoquark into charged leptons. The branching ratio of the first generation leptoquark into the electron plus jet is another unknown in addition to the mass. In the absence of any leptoquark signal an excluded region in the "Branching Ratio" vs "Mass" space can be established.

1.3 Experimental Limits So Far

The UA2 collaboration has searched for leptoquarks in data taken during the 1988/1989 and 1990 running periods [12]. The data corresponds to 13 pb^{-1} at a center of mass energy $\sqrt{s}$ = 620 GeV. UA2 analysed the data for two signal channels. One channel is the two electron plus two jet channel, and the other is the one electron plus two jets plus $\not{E}_T$ channel. UA2 reported at a 95% CL a lower limit on the mass of a first generation leptoquark of 67 GeV/c^2 taking together both signal channels. This limit was determined for an assumed branching ratio of 50% for leptoquark going to charged lepton plus quark. This mass limit increased to 74 GeV/c^2 for a branching ratio of 100%.

Leptoquarks have also been searched for through the decay of Z°. Searches were conducted by the OPAL, DELPHI, ALEPH and L3 collaborations at LEP [13], [14], [15], [16]. L3 reported a lower mass limit from 41 to 44 GeV/c^2, depending on the charge of the leptoquarks and decay channel, based on an integrated luminosity of 5.2 pb^{-1}. The L3 collaboration searched for leptoquarks through the channels $e^+e^- \rightarrow e^+e^-X$, $\mu^+\mu^-X$, $\tau^+\tau^-X$, $\nu\bar{\nu}X$. The OPAL collaboration made a search through the same channels plus the mixed lepton channels $e^+e^- \rightarrow e\nu X$, $\mu\nu X$, $\tau\nu X$. OPAL reported a lower mass limit from 41.4 to 46.4 GeV/c^2 based on an integrated luminosity of 6.3 pb^{-1}. DELPHI reported mass limits for first and second generation scalar leptoquarks of about

43 GeV/c^2 from the two electron or two muon channels. ALEPH reports a similar result for both first and second generation of 44 GeV/c^2. All data samples from L3, ALEPH, DELPHI, and OPAL were for $88.2 \leq \sqrt{s} \leq 94.2$ GeV.

One of the highest limits reported so far is by the CDF collaboration [17]. They assumed a small leptoquark coupling; hence, they looked for signatures of strongly produced pairs of leptoquarks. For a branching ratio of 100% into electron plus quark, the CDF collaboration reports a 95% CL upper limit of 113 GeV/c^2 for a first generation leptoquark and for 50% branching ratio they have a limit of 82 GeV/c^2.

Electron-proton machines have an advantage in the leptoquark search in that leptoquarks are produced in an s-channel resonance and hence have an enhanced cross section. However such cross sections are completely dependent on the unknown leptoquark coupling. The Zeus collaboration at Hera reports a 95% CL limit for a first generation leptoquark with left-handed coupling of 160 GeV/c^2 and 176 GeV/c^2 for a leptoquark with right-handed coupling. A leptoquark coupling approximately equal to α_{em} was assumed [18]. The H1 collaboration [19] has searched for many scalar leptoquarks of various multiplet assignments. Depending on these assignments, H1 obtained 95% CL mass limits ranging from 145 to 192 GeV/c^2 for a leptoquark coupling equal to the electromagnetic coupling.

Chapter 2

The DØ Detector

In order to search for leptoquarks, one needs a good detector. This present search for leptoquarks involves the DØ detector. The DØ detector is one of two large detectors for $p\bar{p}$ collisions at Fermi National Laboratory (Fermilab). Fermilab is located 30 miles west of Chicago. The Fermilab accelerator is a $p\bar{p}$ collider with a center of mass energy of 1.8 TeV where both proton and antiproton beams are accelerated to 900 GeV. It consists of five different accelerators. First in line is the Crockoft-Walton generator which accelerates with a dc voltage H^- ions to 750 keV. Next is the Linac which accelerates particles in a straight line using RF cavities. The Linac accelerates the ions to 2×10^5 keV. The ions are then stripped of their two electrons and injected into a synchrotron of radius 250 feet called the Booster. Here the protons are accelerated to a energy of 8 GeV. The protons are subsequently injected into the Main Ring which is a synchrotron of radius two kilometers. In the Main

Ring the protons are accelerated to 150 GeV. Finally the protons are injected into the Tevatron which is located under the Main Ring. The Tevatron uses superconducting magnets; whereas, the Main Ring uses conventional magnets. The protons are accelerated in the Tevatron to about 1 TeV. The antiprotons are produced when 120 GeV protons from the Main Ring are directed at a production target. The antiprotons produced from this interaction are collected in a Debuncher ring and are stochasticly cooled [20]. The cooled antiprotons are transferred to an Accumulator ring which runs just inside the Debuncher. The collection of antiprotons can last for many hours. Once enough antiprotons are collected, they are injected at 8 GeV along with the protons into the Main Ring where they are accelerated to 150 GeV and so on. The production of antiprotons can be and is generally done during the time when protons and antiprotons are being collided and data is being taken.

DØ has many distinguishing features. First, DØ has no central magnetic field for electron or charged hadron momentum measurements allowing for a more hermetic calorimeter due to the lack of field return yokes and a more compact central tracking system. The DØ calorimeter is finely segmented and is uniform throughout its entire volume. DØ has very good angular coverage for the detection and measurement of muons. DØ's large angular coverage will help in the search for new physics. One last feature of DØ is the Main Ring which goes through DØ. This presents a special challenge for DØ because

dead time must be inserted into the trigger during those parts of the Main Ring Cycle for the production of antiprotons when losses are high or main ring particles are passing through the detector. This issue is discussed more fully in chapter 4.

The DØ detector, figure 2.1, consists of several detector systems combined to create an almost complete coverage around the interaction point. Starting from the interaction point and working outward radially, there is a vertex detector, a transition radiation detector, a central tracking detector in the central region with forward tracking detectors in the forward and backward regions, a liquid Argon-Uranium calorimeter that is divided into three cryostat sections, and finally a muon detection system. In addition to these systems, there are scintillators on top of the DØ detector which helps to reject cosmic muons, and there are hodoscope detectors on each end of the detector near the beam pipe which supply a minimum bias trigger.

The coordinate system that will be referred to throughout this document is described as follows. The direction of the beam pipe is the direction of the line shown in figure 2.1 that goes through the center of the three calorimeters. This is the direction of the proton and antiproton in the accelerator and will be referred to as the z coordinate of the detector. The positive z axis points in the direction of the protons. The angle of rotation about this z direction is the azimuthal or ϕ coordinate. The angle measured from the positive z direction

is the polar or θ coordinate. This θ coordinate is more often expressed as the pseudo-rapidity, η; $\eta = -\ln(\tan(\theta/2))$. So, for $\theta = 0^\circ\,(180^\circ)$ $\eta = \infty\,(-\infty)$, and for $\theta = 90^\circ$ $\eta = 0.0$.

2.1 Vertex Detector

The DØ Vertex Detector [21] was designed to provide precise track measurements for the determination of secondary vertices and also provide a veto for photons which convert in the Transition Radiation Detector. It consists of three nested layers of drift chambers which are divided into azimuthal (ϕ) sectors of uniform field. The first layer is divided into 16 azimuthal sectors, and the second and third layers are divided into 32 sectors. Each sector is outlined by cathode wires, fine field wires, and course field pads as seen in figure 2.2. At the center of each of these sectors are eight sense wires separated radially by 4.57 cm and running parallel, with all the other wires of the vertex detector, to the beam pipe. These sense wires are staggered by 0.1 mm to help resolve ambiguities about which side of the sense wires the particle track was on. On each side of the sense wires are grid wires at ground separating the uniform drift region from the gas amplification region near the sense wires. The gas used in the vertex chambers is a mixture of CO_2 (95%) and ethane (5%) at atmospheric pressure. The coverage of the vertex chambers in η is $\mid \eta \mid < 2.3$ [22].

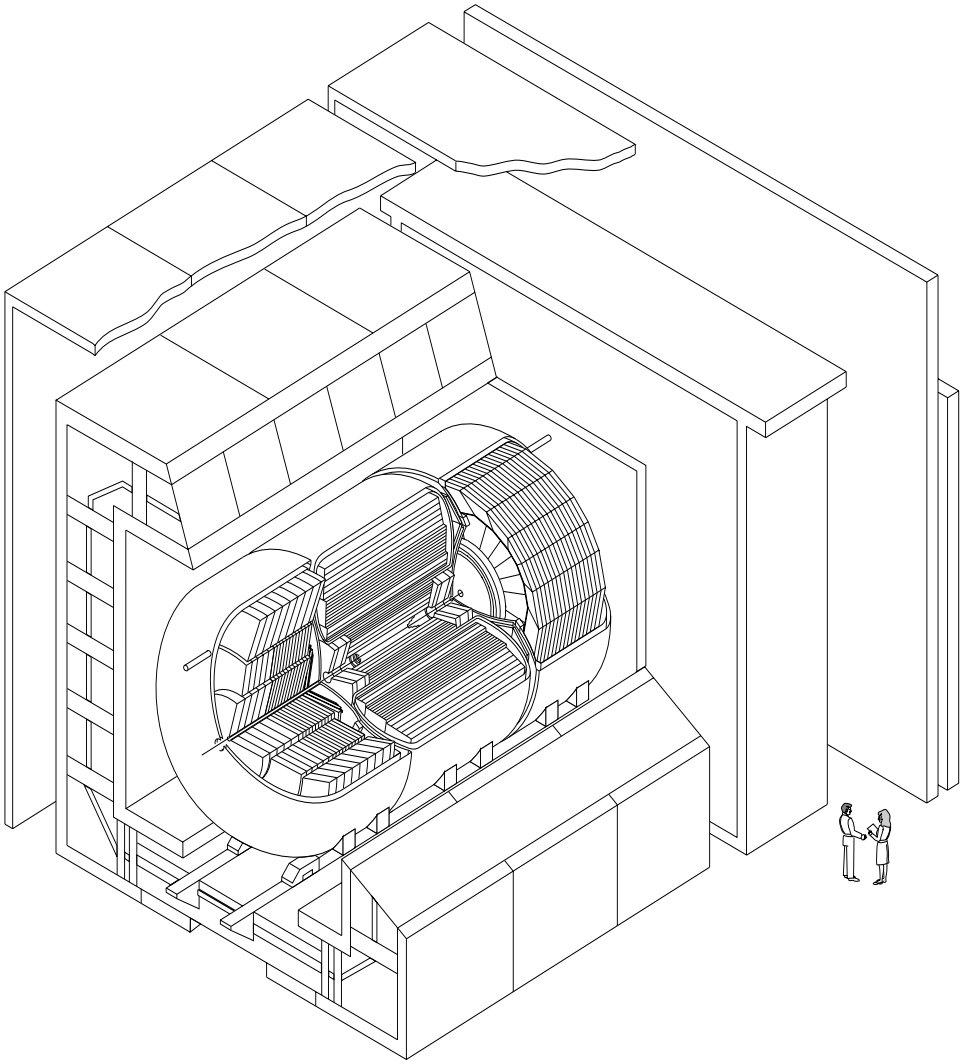

Figure 2.1: The DØ Detector

Figure 2.2: The DØ Vertex Detector

The chambers were tested at the 1990 Fixed target run at Fermilab in the Neutrino-west beamline. The summary of the results from reference [21] is as follows. The drift velocity was found to be $v_d = v_0 + \alpha(\mid E \mid - \mid \bar{E} \mid)$ where $v_0 = 9.74 \pm 0.02$ μm/nsec , $\alpha = 8.68 \pm 0.07$ μm/nsec/kV/cm, and $\mid \bar{E} \mid =$ 1.25 kV/cm. Using a field setting, $\mid E \mid$, of 1 kV/cm a spacial resolution of 60 μm or better was achieved for drift distances larger than 2 mm. Also the efficiency of finding a pair of tracks that are separated by at least 0.63 mm was 90%.

2.2 Transition Radiation Detector

A neutral pion can decay to a pair of photons which can shower electromagnetically in the calorimeter. This pion can mimic an electron if there is a track in the tracking chambers from a low energy charged particle pointing to the cluster of energy in the calorimeter produced by the neutral pion. A method of distinguishing these pions is needed when the neutral pion and its associated charged particle are close enough together so that the track for the charged particle satisfies the proximity requirement for an electron's calorimeter energy cluster and track. The Transition Radiation Detector (TRD) was included into the DØ detector to reject such neutral pions.

As predicted by Ginzburg and Frank [23] soft x-ray transition radiation is produced by charged high energy particles traversing the boundary between two materials of different dielectric constants. This radiation is emitted into a cone about the axis of the trajectory of the particle, and the cone has an angle on the order of $1/\gamma$, $\gamma = E/M$. The total energy radiated is proportional to γ; therefore, this transition radiation can be used to distinguish between electrons and pions. All that is needed is to increase the yield of soft x-ray photons by using several alternating layers of two materials of different dielectric constant and provide for a means to convert the photons into electric charge and then collect that charge. One can see then that an electron would produce a larger

collected charge since the amount of transition radiation produced is inversely proportional to the mass.

The TRD that is used at DØ is described briefly as follows [23] [24]. The TRD consists, as in the Vertex Detector, of three nested detectors. Each cylindrical layer consists of two chambers; see figure 2.3. The first, inner chamber, is the radiator. It consists of 400 layers of polypropylene of 18 μm thickness. Each layer is separated by 150 μm gaps. The gaps are filled with helium at atmospheric pressure. The outer chamber is the photon detector which is a time-expansion drift chamber with a 15 mm radial drift space. Each of the photon detectors has 256 readout channels in a projective geometry. The gas used in the drift chambers is a mixture of Xe, for conversion of x-rays to electrons, and methane (CH_4) as a quencher. The two chambers are separated by two mylar windows which are separated by a 2 mm gap. This gap is flushed with nitrogen gas. Test of the DØ TRD give a pion rejection factor of about 50. These results were for an electron efficiency of 90%. The TRD gives a coverage in η of $\mid \eta \mid < 1.6$ [22].

Figure 2.3: The DØ TRD

2.3 Tracking

Tracking for the DØ detector, in addition to the Vertex Detector, is handled by a outer Central Drift Chamber (CDC), which surrounds the TRD, and two sets of Forward/Backward Drift Chambers (FDC). The CDC covers a η range of about $\mid \eta \mid \leq 1.2$. The FDC covers a range of about $1.4 < \mid \eta \mid \leq 3.1$ [22]. The drift chambers were designed for good spatial resolution and good two hit resolution. They were also designed for good dE/dx measurements to distinguish between singly and doubly ionized tracks. This is necessary in order to discriminate against photon conversions, particularly in the region of the detector outside the acceptance of the TRD and Vertex Chambers.

2.3.1 Central Tracking

The CDC [25] consists of four cylindrical layers each one divided in ϕ into thirty-two cells. Each cell contains seven sense wires, staggered by 0.2 mm, running parallel to the beam pipe and two delay lines which are embedded in the outer and inner walls of each layer next to the sense wires. There are also guard wires at ground in about the same configuration as in the Vertex Chambers. The field shaping electrodes are embedded in the walls of the chambers. The delay lines give a measurement of the z coordinate of the track.

Tests with cosmic rays and the 1990 Fermilab fixed target test beam were performed on the CDC. A summary of the test results [26] is as follows. The gas used in the CDC was a mixture of 93% Argon, 4% Methane, and 3% CO_2. With a drift field of about 650 V/cm, the drift velocity was determined to be about 37 μm/ns. The maximum drift distance is 7 cm with a sense wire resolution less than 230 μm for the five inner sense wires and less than 330 μm for the two outer sense wires, which are closest to the chamber walls. The two track efficiency was found to be 50% for tracks that were separated in time by 45 ns or 1.7 mm in distance and 90% for tracks separated by 65 ns or 2.5 mm. Measurements of dE/dx gave a 95 $\pm$ 13 rejection factor for simulated[1] double

[1]Two singly ionized tracks were overlaid to mimic a doubly ionized track.

MIP[2] tracks. Here a cut of 1.3 MIP was used on a 70% truncated mean, which is the mean of the 70% lowest sense wire charge measurements. These cuts give a 95% efficiency for a single MIP track.

2.3.2 Forward Tracking

The forward/backward tracking [25] is achieved by two sets of three drift chambers. These chambers are of two types as shown in figure 2.4. Two of the three chambers are designed to measure the θ coordinate and are rotated 45° with respect to one another. The third chamber is sandwiched between the two Theta chambers and is designed to measure the ϕ coordinate. The Phi chamber consists of sixteen layers of 50 cm length radial sense wires. Each layer has 36 sense wires, and between each sense wire is a guard wire at ground. The Theta chambers have eight layers of sense wires strung in the Cartesian x and y coordinates of the detector. In other words, each of the rectangular cells has eight sense wires strung along the longest dimension of the cells. Between each pair of these sense wires there is a pair of grounded guard wires. The Theta chambers also have delay lines for each of its cells to measure the coordinate parallel to the sense wires. Both types of chambers have a maximum drift distance of 5.3 cm and sense wire staggering of 0.2 mm.

[2] A MIP refers to a particle or the energy deposited by that particle via ionization. The particle has a particular combination of species and energy such that it minimally ionizes the detector material.

Figure 2.4: The Forward Drift Chambers

The FDC was tested during the summer of 1990 during the Fermilab fixed target run. The chambers were tested with both pion and electron beams. The results[27] are as follows. The spacial resolution of the Theta chambers varies from about 160 μm at a drift distance of 0.5 cm to about 240 μm at a drift distance of 5.0 cm. The spacial resolution of the Phi chambers varies from about 150 μm at a drift distance of 0.5 cm to about 200 μm at 4.0 cm. Both chambers had a sense wire efficiency of 95%. The delay line resolution of the Theta chamber was optimized to 2.0 mm at an efficiency of 95%. The two hit efficiency was 90% for hit separations of 2.5 mm. Using a photon beam, the rejection factor for photons that convert to e^+e^- pairs was found to be 31 with an efficiency of 91% for single electron tracks. This rejection/efficiency

was determined for busy events with a multiplicity of tracks greater than one. For single track events, the photon conversion rejection factor was 85 with an efficiency of 97% for single electron tracks.

2.4 Calorimetry

The DØ calorimeter is a Uranium - liquid Argon sampling calorimeter with a semi-projective geometry. It has a solid angle coverage of nearly 4π; $1.3^\circ \leq \theta \leq 180^\circ$ ($\mid \eta \mid \leq 4.5$). The calorimeter is divided into three separate sections, one Central Calorimeter (CC) and two End Calorimeters (EC); see figure 2.5. In the CC electrons are fully contained in a range of η of about $\mid \eta \mid \leq 1.0$, and pions are fully contained in a range of about $\mid \eta \mid \leq 0.8$. In the EC electrons and pions are fully contained in the range $1.5 \leq \eta \leq 4.5$. In the region $0.8 < \eta < 1.4$ the energy is shared between the CC and EC. Here, particles have to go through two sets of cryostat walls. Also, in a small angular region about $\eta = 1.35$, there is no coverage for electrons. There are also various support structures in this region.

Monte Carlo studies showed a 50% loss in the reconstructed energy in the region of η , $0.8 < \eta < 1.4$; therefore, a Inter Cryostat Detector (ICD) was put between the CC and EC cryostats to provide additional information about the energy of particles traversing the inter cryostat region. In addition to the ICD there are sampling detectors, Massless Gaps (MG), which sample the region

of liquid Argon between the ends of the CC and EC active detector elements and the cryostat walls. The coverage in η for these MG's is about the same as that of the ICD. The results of tests of various parts of the calorimeter will be presented in chapter 3.

2.4.1 Central Calorimeter

The CC is of modular construction. It consists of three concentric cylinders of modules of about nine feet in length. The first ring of thirty-two modules is the Electromagnetic (EM) section for the energy measurement of electrons and photons. Each EM module is subdivided in radial depth into four readout layers. The next ring of sixteen modules is the Fine Hadronic (FH) section. These modules are divided in radial depth into three readout layers. The last ring of sixteen modules is the Course Hadronic (CH) section; each module has only one readout layer. The EM section has a total depth in radiation lengths of 20.5, and the EM, FH, and CH sections together present a total of 7.16 nuclear interaction lengths to hadronic showers [28]. The EM and FH modules use uranium as an absorber material, while the CH uses copper. The CC has a segmentation in η and ϕ of $\delta\eta = \delta\phi = 0.1$ in most of the readout layers of the calorimeter. The exception is the third layer of the EM modules where the shower maximum for electromagnetic showers is expected. It has transverse segmentation $\delta\eta = \delta\phi = 0.05$. This allows for better position resolution.

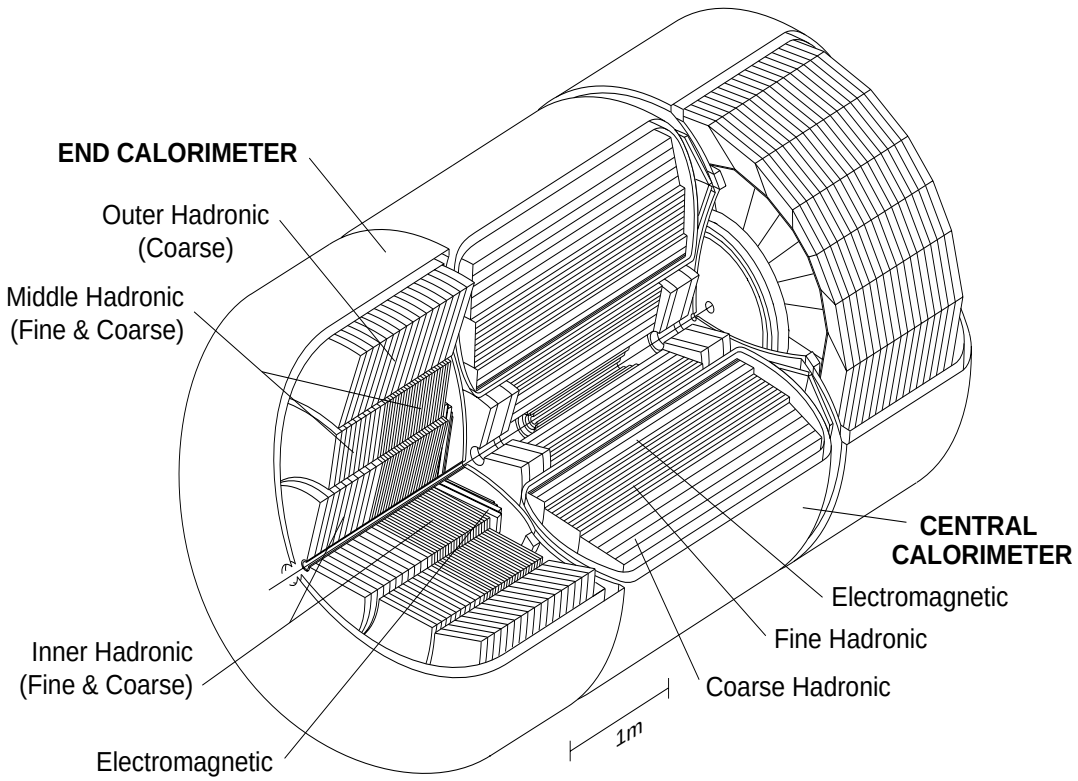

Figure 2.5: The DØ Calorimeter

A detailed view of the plate level construction of the calorimeter can be seen in figure 2.6. The absorber plates are separated by about 4.6 mm from the surface of one plate to the next surface of the next plate. The EM modules have 3 mm thick plates while the FH modules use 6 mm thick plates[28]. In the middle of the gap between two absorber plates are the signal boards. Each signal board consists of copper signal pads, on each side of which is a sheet of G-10[3]. The G-10 is coated on the side of the gap with a carbon based resistive epoxy. The gaps between the signal boards and absorber plates are 2.3 mm wide and filled with liquid Argon. As a particle traverses the argon gap, it ionizes the argon. The resistive coating on the signal boards is kept at a high positive voltage[4] while the absorber plates are grounded. The ionization electrons drift in the uniform field of the gap inducing a current in the copper signal pads. This induced current is the signal out of the calorimeter. The signal from all signal boards in a given layer for a given η and ϕ are ganged together into a readout board which carries the signal to the ends of each module.

The Massless Gaps [29] use the same type of signal boards and consist of a few alternating layers of signal boards and 1.5 mm copper clad G-10 boards. There is one readout board per MG. Each MG conforms to the η, ϕ segmentation of the calorimeter modules and has 20 readout channels. The

[3]G-10 is a composite of glass and epoxy

[4]High negative voltage was initially tried, but it produced discharges in the liquid argon. This was probably due to the build up of positive ionic charge on the resistive coat.

Figure 2.6: The DØ Calorimeter: plate level structure

argon gap is the same as that for the rest of the calorimeter. The MG as its name implies has very little absorber material and serves to sample the energy of particles just before it enters the cryostat wall (or in the case of the EC, just after the cryostat wall). In essence the cryostat wall serves as the absorber material for the MG.

2.4.2 End Calorimeter

The construction of one of the EC can be seen in figure 2.5. It, like the CC, is modular in construction. The EC EM module faces toward the center of the detector. Behind the EC EM and centered is the Inner Hadronic (IH) module. In a concentric ring around the IH module are the sixteen Middle

Hadronic (MH) modules. And in a concentric ring around the MH modules are the sixteen Outer Hadronic (OH) modules. The EC EM has a total of 23.3 radiation lengths divided into four readout layers. The IH and EM combine to give a total of 8.2 nuclear interaction lengths. The MH and OH rings were designed to give with the IH and EC EM the same number of interaction lengths over the full containment range of the EC. The EC EM uses 4 mm thick Uranium plates. The IH and MH use 6mm thick plates in their first four readout layers and 4.65 cm thick stainless steel plates in the last readout layer. The OH uses 4.65 cm stainless steel throughout. The segmentation in η and ϕ is the same as in the CC except at the higher values of η , $|\eta| > 3.2$ ($|\eta| > 2.6$ for third EM layer[30]), where the segmentation is more coarse to keep the minimum pad size at least as large as the Moliere radius.[5] The liquid Argon gap size is the same as in the CC.

[5] The Moliere radius M_R is the characteristic length of the transverse shower development and is scaled to the number of radiation lengths by $R_M \simeq 1.9X_0 \simeq 1.14cm$ for the DØ calorimeter.

2.4.3 Inter Cryostat Detector

The Inter Cryostat Detector (ICD) consists of two rows of boxes mounted on the EC wall as shown in figure 2.7. Each box contains three scintillating tiles, wave shifting light guides, three photo multiplier tubes (PMT) with base, and a preamp for each tube. The tiles are layed side by side along the length of each box. The size of the tiles is such that they conform to the transverse segmentation of the calorimeter. The electronics are mounted on top of the tiles.

Due to the variations in the quantum efficiencies of the PMT's, variations in the tile-fiber couplings, and changes in the response of the tile and electronics over time, a time dependent relative calibration of the ICD is needed. This is achieved by the use of a nitrogen UV laser. Laser light is conducted to each tile through a system of optical fibers, patch boxes, feedthroughs, and fanouts. The amount of light getting to the tiles is adjusted by use of filter wheels which can vary the amount of light from a few MIP's to 1000 MIP's. The laser light produces an ionization signal similar to that of a particle traversing the tiles; therefore, with a controlled input the relative, time dependent gains of the tiles can be determined [31].

Figure 2.7: The DØ ICD detector mounted on an EC

2.4.4 Calorimeter Electronics and Signal Routing

With the segmentation described above, there are approximately 63,000 channels coming out of the three cryostats. With this many channels, large amounts of electronics are needed to process the calorimeter signals. A more detailed description of the design and performance of the calorimeter electronics is given in references [32] and [33]. A brief overview is given here.

The electronics for the DØ calorimeter precision readout are built in three stages, each stage at a different physical location. The first stage is the preamplifier which amplifies the signal coming out of the cryostat. The charge sensitive preamps are housed in 12 shielded boxes mounted just outside the 12

cryostat ports (four for each cryostat) carrying the signal cables. Each channel has its own preamp. The signals coming from a given module of the calorimeter are organized so that many η and ϕ values for a given layer are carried by a single multi-coaxial cable. These cables are connected to feedthrough cards which feed the signals from inside of the cryostat to the outside. The cards also reorganize the signals into projective towers; all the layers for a given η and ϕ are read sequentially. Twisted pair cables carry the signal from the feedthrough to the preamps.

There is about 80 feet of twisted pair cable connecting the preamps to the next stage of the electronics, the BaseLine Subtractors (BLS), where the signals are shaped and sampled. The electronics for the BLS's are located underneath the detector platform and are inaccessible during collider running. After the signal is shaped and the base sample is subtracted from the peak sample, the signals are multiplexed 16 to 1 into analog cable drivers. Here if the signal is less than 1.25 volts then it is amplified by eight.

On the same BLS boards are electronics which perform coarse energy sums of the level one trigger towers (see chapter 4, section 4.1). These energy sums eventually get passed into the calorimeter trigger.

The signals from the BLS's are then carried via $\sim$ 300 ft of twisted pair cable to the Analog to Digital Converters (ADC) which are located in the Movable Counting House (MCH) located outside of the collision hall. In the ADC's the

analog signal is digitized into a 12 bit word which is then converted into a 15 bit right justified word. Those analog signals which were not amplified in the cable drivers are then shifted as ADC words three bits to the left; therefore, a 15 bit dynamic range with 12 bit accuracy is achieved.

The relative gain of each electronics channel is determined using a pulse generator that sends a charge pulse to a high precision resistor connected to the input of the preamplifiers. There is a pulse generator for each of the 12 preamp boxes. Each pulser is fanned out into 32 inputs in the backplane of its associated preamp box. Each input into the preamp box is connected to 144 channels. Variations in the calorimeter response due to variations in the electronics can be taken out by measuring the average signal out of each channel for a constant input pulse into the preamp.

2.5 Muon Detector

A side view of the DØ detector is shown in figure 2.8. The muon system consists of two subsystems, the Wide Angle Muon Spectrometer (WAMUS) and the Small Angle Muon Spectrometer (SAMUS). The WAMUS detector has an angular coverage of $10^\circ \leq \theta \leq 170^\circ$, and SAMUS has an angular coverage of $3.7^\circ \leq \theta < 10.0^\circ$ [34]. The contribution to the momentum resolution of the muon system from multiple scattering in the iron toroids is $\delta p/p = 18\%$. This is the major part of the resolution for momentum up to about 100 GeV.

Figure 2.8: Side View of DØ Detector

For higher momentum the contribution to the momentum resolution from the position resolution of the track measurements begins to overtake the multiple scattering term. This position resolution contribution becomes twice the multiple scattering term at about 250 GeV.

2.5.1 Wide Angle Muon Spectrometer

There are three large toroids in the WAMUS [35] detector. The central toroid (CF) has an angular coverage of 41° to 139°, and the two end wall toroids (EF) have a coverage of 9° to 43°. The CF iron has a thickness of about 110 cm, and the EF iron is about 150 cm thick. The CF and EF operate with a magnetic

field of about 2 tesla. Figure 2.8 is in the bend view of the muon detector. The field lines generally make a "circle" in the direction of ϕ. The position of the muons as they pass through the iron toroids is measured by three super-layers of proportional drift tubes (PDT). The first layer, layer A, measures the track of the muon just before it enters the toroid. Layers B and C measure the track after the toroid. The A layer consists of four planes of drift tubes, while the B and C layers consist of three planes each of drift tubes.

Each WAMUS PDT has a 10.1 cm wide $\times$ 5.5 cm high cross section. Each of these cells consist of a grounded aluminum shell with a centered sense wire and two vernier cathode pads mounted on the inside top and bottom surfaces as seen in figure 2.9. The sense wire and vernier pads are held at a potential of +4.54 and +2.6 kv respectively. The gas mixture used in these cells is 90% Ar, 5% CF_4, and 5% CO_2, which has a drift speed of 70.5 mm/μs for electric fields above 0.7 kv/cm [36]. The sense wires are perpendicular to the beam pipe direction; they run parallel to the magnetic field lines. The drift time to the sense wire gives the coordinate with respect to the cell which is perpendicular to the sense wire for the charged track of a muon which, with similar measurements from PDT's above and below, will translate into the η coordinate of the muon. The sense wire is also used to give a coarse measurement of the cell coordinate parallel to the sense wire, and using this information, the vernier

Figure 2.9: The DØ Muon Detector: WAMUS PDT cross section

cathode pads give a refined measurement; see reference [35] for a more detailed description. These measurements translates into the ϕ coordinate.

The A layer with its four planes of PDT's is 17 cm from the innermost to the outermost sense wire. With a resolution, transverse to the sense wire, of 0.2 mm [6], the accuracy in the bend view is ± 0.6 mrad for the angle of the incident particle into the toroid and $\pm 0.2/\sqrt{4} = 0.1$ mm for the entrance position of the particle. The distance between the center of the B and C layers is about 136 cm; the position and angle of the outgoing particle is determined to ± 0.17 mm and ± 0.2 mrad respectively. For the longitudinal resolution, parallel to the sense wire, there is an accuracy of ± 2.0 mm.

[6] Survey inaccuracies actually limit this to 0.5mm

2.5.2 Small Angle Muon Spectrometer

The SAMUS consists of two plug toroids seen in figure 2.8. These toroids are about 150 cm thick and will maintain a magnetic field of about 2 tesla. At each end of the detector there are three stations of PDT tubes. One is before the SAMUS toroid, and two are after the toroid. The PDT tubes of each station are divided into three layers. The PDT's in a given layer are placed parallel. Two layers are positioned so that the tubes in one layer are perpendicular to the tubes in the other layer. The third layer is at a 45° angle to the other two layers. This third layer of PDT tubes is used for multi-track correlations to untangle the tracking information in this high multiplicity region of the detector. The PDT's used for the SAMUS detector are not of the same design as those used for the WAMUS detector; see reference [35] for a description.

Using a gas mixture of 90% CF_4 and 10% CH_4 test of the SAMUS PDT tubes were done with cosmic rays [37]. With an average drift velocity of 95 mm/μs, the minimum drift time was 150 ns. The average resolution perpendicular to the sense wire was 0.4 mm using one tube and 0.3 mm using one plane of tubes.

Figure 2.10: One plane of a DØ Hodoscope

2.6 Level 0 Hodoscopes

The information on whether $p\bar{p}$ collisions occurred during a beam crossing is supplied by two sets of scintillator plus PMT arrays (hodoscopes). This information consists of a comparison between the time of arrival of particles in the forward and backward directions as they interact with the hodoscopes. The hodoscopes are located in space between each of the two EC's and FDC's. Each consists of two planes. Each plane has four long scintillating tiles with PMT's on both ends and ten short tiles plus light guide, each connected to a PMT. The tiles are arranged as shown in figure 2.10. The two planes are placed perpendicular to each other giving a nearly complete coverage over $2.2 <| \eta |< 3.9$ and at least a partial coverage over $1.9 <| \eta |< 4.3$ [38].

The time response of the PMT's is calibrated [39] using a pulsed N_2 laser with a wavelength of 337 nm . The laser light is split and routed to the 72

PMT's. Since the hodoscopes are part of the trigger, it is important to maintain the calibration of the PMT's throughout the run; the effects from shifts in the time response of the PMT's can not be taken into account off-line. When calibrated, the resolution for the long counters is about 80 ps and about 120 ps for the short counters [38]. This translates to a position resolution of 3 cm for the locating of the z position of the vertex which is another function of the hodoscopes. They also detect multiple interactions, and provide monitoring of the luminosity.

Chapter 3

Calibration of Calorimeter

The response of various parts of the calorimeter to electron and pion beams was studied in two fixed target runs at Fermilab. For the first fixed target run in 1990, the configuration of calorimeter modules shown in figure 3.1 was used. This will be referred to as "Load One", which was for the calibration of the EC EM and IH modules. Both electron and pion beams with energies ranging from 10 GeV to 150 GeV were used. In the 1991 fixed target run, the configuration of figure 3.2 was studied. This "Load Two" was for calibrating the CC modules and for studying the transition region between the CC and EC, which has the ICD and massless gaps. Load Two had five CC EM modules, two each of CC FH and CH modules, and two each of EC MH and OH modules. In addition to the beams available in Load One, there were also low energy electron and pion beams with energies ranging from about 1 Gev to 10 Gev. For both fixed target runs proportional wire chambers (PWC) were used to give tracking

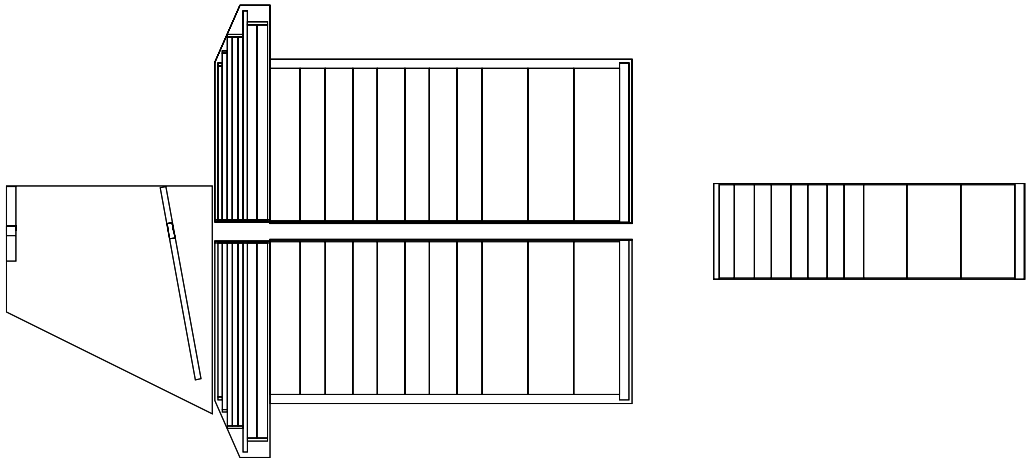

Figure 3.1: Load One Configuration; beam coming from the left

information on the test beam particles. There were also Cherenkov chambers which provided information on the particle type, which help to insure the purity of the data by providing a veto or tag against unwanted particle types. Scintillator counters placed behind the calorimeter provide a veto for muons and pions which travel through and out of the calorimeter without showering. Measurement of the beam momentum was provided by the use of a set of dipole magnets where a Hall probe was used to measure the magnetic field. What will be presented in this chapter are the results of various studies dealing with the issues of linearity of response, energy and position resolution, e/π ratio, uniformity, and shower shape. Many of the results between the two test beams will be similar; therefore, more attention to detail will be given for Load One. Also some sources of systematics will be discussed along with the transferring of the calibration to DØ.

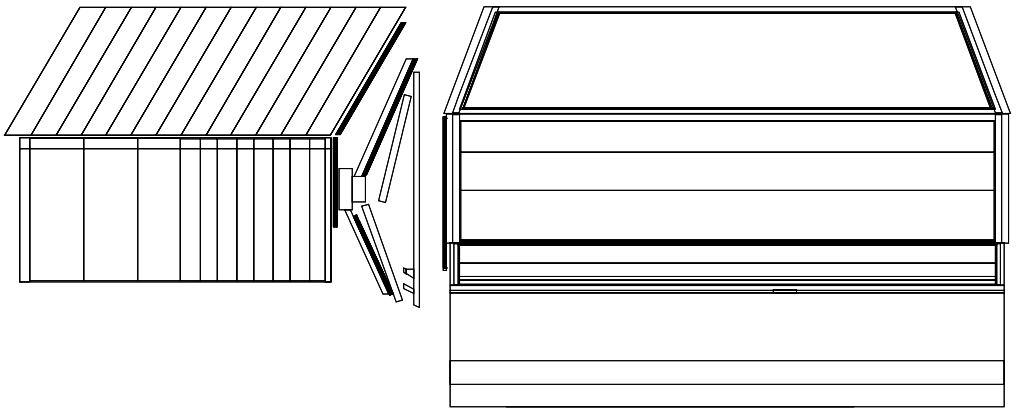

Figure 3.2: Load Two Configuration

Understanding the response of the calorimeter is important in understanding the systematics of energy fluctuations, energy scale and uniformity of response. The leptoquark analysis that follows in chapters 4 and 5 depends on a uniform calorimeter with good energy and spacial resolutions. A description of the systematics relevant to the leptoquark analysis will be given in chapter 5.

3.1 Response

In what follows the mean response of the calorimeter to a pion or electron beam of a given energy is the mean of the gaussian fit to the distribution of responses to individual particles. The data were pedestal subtracted, and variations in the channel to channel gain due to electronics were removed. The value of the pedestals was measured every eight hours, and the gains were measured every 24 hours. Events were screened by using information from the PWC's and Cherenkov chambers. Events (particles) of the wrong species were removed from the data sample. Events with too many hits in the PWC chambers mounted just before the calorimeter were removed to cut down on events where the beam particle began showering upstream of the calorimeter. The spread in the calorimeter response due to the spread in the beam momentum was removed on a event by event basis. Calorimeter fiducial volume cuts about the position of the beam were done. For electrons in most cases, the cut was 0.5×0.5 in η, ϕ, and only the four layers of an EM (EC or CC) module plus

the first layer of the following hadronic module (FH or IH) were included. For pions a 1.5×1.5 cut in η, ϕ was used summing all layers.

The linearity [40] of mean response for Load One to electrons and pions was determined by measuring the response in ADC counts of the calorimeter to a beam of electrons or pions of varying energies. Here ADC counts refers to the integer number obtained from the conversion of the analog signal from the detector to a digital signal. From a straight line fit of the plot of ADC counts vs beam energy, the conversion between ADC to GeV can be determined. For Load One electron data the slope of the fitted line is 267.4 $\pm$ 0.7 ADC counts/GeV with an offset (y intercept) of –80.2 $\pm$ 5.3 ADC counts. For Load One pions the slope is 257.1 $\pm$ 0.7 ADC counts/Gev with an offset of 565.6 $\pm$ 12.8 ADC counts. The larger offset for the pions is primarily due to the fact that pion showers require the summation of more channels and hence more uranium noise[1]. The deviation from linearity for the Load One electron data, when comparing the mean response and the energy calculated from the fit, was less than $\pm$ 0.3% over the range of beam momentum from 10 GeV/c to 150 GeV/c. For pions the deviation from linearity was less that $\pm$ 3.0% but typically was less than $\pm$ 0.5%.

For Load Two electrons and pions the linearity of the response [41] is similar but vary somewhat in their offsets. The linear function between ADC counts

[1]Uranium noise causes asymmetric pedestal distributions with a high positive tail.

and GeV for electrons had slope of 261 ADC counts/GeV with a y intercept of –75.7 ADC counts. For Load Two pions the slope of the fitted line was 262.4 ADC counts/GeV with an intercept of –143.7 which differs significantly with the Load One pion response. This variation may be accounted for by differences in the upstream material between Load One and Load Two or changes in the calorimeter BLS sampling times which occurred during the course of Load Two. In fact for electrons the value of the slope and intercept varied somewhat for Load Two with the value of η and ϕ. Much of this variation in ϕ in the response to electrons can be accounted for by variations in the thickness of the uranium plates and argon gaps and can be corrected [42] for by taking into account these variations in the sampling fractions (See below in Energy Resolution section.); an additional ϕ dependent multiplicative factor is introduced into the energy scale for the layers of the EM calorimeter. The remaining variation in η which was as much as about 4% for 100 GeV electrons going from η of 1.0 to 0.0 is not well understood. This variation can be reduced to about 1% if the sampling weights are optimized (See below on Energy Resolution section.) [43]. It is not certain that this variation in η is present in the actual detector, so at present this effect is not corrected.

In terms of the differences in the conversion factor between electrons and pions, it was observed that one could, first, ignore the offset for the electron response since it has a small effect. Secondly, if for the pion response the

offset is restrained to zero and the fitted slope for the electron response is used, the performance of the non-optimized sampling fractions with respect to pions was about as good as possible in terms of the linearity and resolution. Therefore, the conversion between ADC counts and GeV for the EC modules for both pions and electrons was set at 267.2 ADC counts/GeV and 261 ADC counts/GeV for the CC modules. The result of this approach is that the linearity is a little worse at the lower energies. The possibility of allowing the use of an offset is still under consideration and study.

The response for Load One to electrons was very uniform [30]. The response as a function of ϕ was found to deviate by $\pm$ 0.4% (rms) from the mean for electron scans taken in regions of the calorimeter (EC EM) with no structural cracks (gaps) or supports. In the same regions the response as a function of η varied by as much as $\pm$ 0.5%. For areas near cracks[2] in the uranium plates, the response increases by a maximum of 5% at the crack and was reduced to a 2.5% increase in response 1.4 cm from the crack. At the 1% level of deviation from uniformity, 2.5% of the EC EM active area is affected by the uranium plate cracks. The response near tie-rods, which are support structures for the EC EM, was found to decrease by as much as 15%. The response was degraded by half as much 18 mm away in the ϕ direction or 26 mm in the direction away

[2]Each uranium plate is actually constructed of two of three pieces of uranium. Where two of these pieces comes together, there is a small crack or gap in the uranium.

or toward the center ($\eta = \infty$) of the EC EM module. The total area affected by the tie-rods is 8% (1.5%) for a signal loss of 1% (5%).

The response of Load One to pions as a function of η and ϕ is shown in figure 3.3. The response as a function of η in figure 3.3-a shows a fall off for values of $\eta < 2.25$. This is an artifact of the Load One geometry. It is due to leakage out the side of the IH module which will be caught by the ring of MH and OH modules in the DØ calorimeter. The gradual fall off for $\eta > 2.5$ is due to lateral leakage into the beam pipe region. The amount of signal loss at $\eta = 3.7$ is about 3%. Assuming that this loss is corrected for, there remains a $\pm$ 0.4% deviation. For the response as a function of ϕ, there is a deviation of $\pm$ 0.5% except near the region of a crack in the uranium plate where the deviation is about 1.5%. This can be seen in figure 3.3-b at $\phi = 3.25$ where there is a crack in the uranium plates.

Load Two showed that the central calorimeter modules are uniform in response to electrons within about 1% except near the cracks between the EM modules where the response can drop by as much as 10% [43]. The response of the central calorimeter to pions is also uniform within 1% except near the cracks between the fine hadronic modules where the response decreases by as much as 10%.

Figure 3.3: Uniformity of Response of Load One for Pions: a)Response vs η, b)Response vs ϕ

3.2 Energy Resolution

The fractional resolution is defined as the standard deviation, σ, of the gaussian fit to the response distribution divided by the mean response μ. This fractional resolution can be parameterized by the equation 3.1.

$$(\sigma/\mu)^2 = C^2 + S^2/E + N^2/E^2 \tag{3.1}$$

Here C, S, N are the constant, sampling, and noise terms respectively that contribute to the resolution, and E is the measured energy (momentum) of the beam. The constant term comes from systematics such as residual variations in gains. The sampling contribution is due to the statistical error in sampling, and the noise term has contributions from energy independent sources such as uranium noise and electronic incoherent noise. The values [40] for these fitted parameters for electron data in Load One are as follows.

$$\begin{aligned} C &= 0.003 \pm 0.003 \\ S &= 0.157 \pm 0.006(\sqrt{GeV}) \\ N &= 0.29 \pm 0.03(GeV) \end{aligned}$$

The above numbers were determined from analysis for which the sampling fractions (sampling weights) were optimized with respect to electrons; the

weights for the four EM layers plus the first hadronic layer were optimized. Consider equation 3.2 where E_i is the energy in GeV of event i.

$$E_i = \alpha \sum_{j=1}^{n} \beta_j ADC_{ji} + \Delta \tag{3.2}$$

For electrons n equals five, and n equals eight (EC) or nine (CC) for pions. The parameters α and Δ are the overall scale and offset respectively, which are related to the slope and intercept of the fitted line to the linearity plot, i.e. $\alpha =$ 1/slope and $\Delta =$ –intercept/slope. The energy in each layer j expressed in ADC counts is ADC_{ji}. The parameter β_j is the sampling weight for layer j. These sampling weights are related to the sampling fractions, which are the fractions of live energy (energy loss of traversing particle due to ionization of liquid argon) to the total energy (energy loss due to ionization of argon, uranium, and signal boards) for a given layer. Initially, the weights are set equal to rescaled sampling fractions; the sampling fractions are normalized such that the sampling fraction for the EC EM layer three is equal one. The sampling weights are then optimized by minimizing χ^2, where χ^2 is the weighted difference, squared, of E_i and the beam momentum summed over a range of energies and averaged over a large number of events per energy. The weights used for minimizing χ^2 are 1/(fractional resolution) determined at each energy. The optimized sampling weights varied little from the initial values.

Equation 3.1 was fitted to Load One pion data [40]. The values for C, S, and N are as follows.

$$
\begin{aligned}
C &= 0.039 \pm 0.002 \\
S &= 0.446 \pm 0.009(\sqrt{GeV}) \\
N &= 0.975 \pm 0.03(GeV)
\end{aligned}
$$

These values were determined with a cut on the energy in the first EM layer to eliminate events which started showering (due to upstream material) before the first EM layer. These numbers reflect an intrinsic resolution. Without this cut the sampling term grew to $0.50\sqrt{GeV}$. This number is probably closer to what will be quoted for the DØ calorimeter due to the central tracking detector in front of the calorimeter. As before for electrons, these results were derived with optimized sampling weights. With the optimized electron sampling weights before mentioned fixed, the sampling weights for the rest of the layers were optimized with respect to pion data. As before the weights changed little from their initial values. The energy resolution for pions and electrons calculated from Load Two data was very similar to that determined for Load One. And as before mentioned, the resolution remained stable when fixing the overall scale α to that for electrons and requiring that the offset Δ be zero.

3.3 Position Resolution for Electrons and Pions

Good spacial resolution for electrons is important. A photon can mimic an electron if there is a low energy charged particle leaving a track pointing near the impact point of the photon. The finer the position resolution, the more likely that such an photon can be rejected as not being an electron candidate. The average position resolution for Load One electrons was found to be 2 mm at 25 GeV decreasing to 1 mm at 75 GeV [40]. These numbers were determined for the third EM layer where the pad size, $\Delta\eta \times \Delta\phi = 0.05 \times 0.05$, is finer than in other layers and where the most accurate shower position can be determined. The average resolution shows a slightly stronger than $1/\sqrt{E}$ energy dependence. The resolution near the pad edges tends to be better than that near the center of the pad. The above numbers for the resolution are for both transverse dimensions $r\Delta\phi$ and Δr, which are related to $\Delta\eta$ and $\Delta\phi$ in the EC calorimeter. Here $r\Delta\phi$ is the distance along the arc in ϕ and Δr is the distance perpendicular to the z axis.

The spacial resolution of pion showers in the EC was also determined to have about a $1/\sqrt{E}$ dependence. Specifically, $\sigma(r\Delta\phi) = (54.9 \pm 1.3)E^{-0.551\pm0.005}$ mm and $\sigma(\Delta r) = (49.4 \pm 1.9)E^{-5.02\pm0.008}$ mm; therefore, at 25 GeV the spacial resolutions is 9.3 mm in $r\Delta\phi$ and 9.8 mm in Δr. These values were determined by using all layers of calorimetry. [44]

3.4 e/π Ratio

An electron traversing a medium will lose energy initially through Bremsstrahlung radiation if its energy is great enough, and it will lose energy through the ionization of the medium. The Bremsstrahlung radiation produces a shower of electrons, and as the shower develops the energy loss eventually proceeds through ionization only. For the case of a charged hadron, Bremsstrahlung and ionization processes also apply. However, because hadrons can also interact strongly, there is the possibility that neutrons can be liberated from the medium. Low energy neutrons can then carry part of the energy of the hadron shower; this energy is in general undetectable. Therefore, a hadron will produce a smaller signal than an electron of equal energy. A π° decays mostly to a pair of photons, $\pi^\circ \rightarrow \gamma\gamma$. This pair of photons can then shower like an electron by pair converting. The energy content of a jet, produced by a quark of given energy, can then vary according to the neutral pion content of the jet. As a result the jet energy resolution is worse than the resolution expected from sampling fluctuations. This effect can be eliminated if the response of hadrons were equal to the response of electrons; e/π equals 1.0.

If a material like uranium is used as the absorber material in a sampling calorimeter, then energy lost to neutrons in hadronic showers can be regained by interactions of the neutrons with the uranium; a proton, for example, could be liberated, which could produce detectable energy. This compensation was

studied in Load One [40]. The e/π ratio was determined to be 1.09 for 5 GeV particles decreasing to 1.02 for 150 GeV particles.

3.5 Shower Shape

As mentioned above, a high energy charged particle will emit Bremsstrahlung radiation. These photons then pair convert into e^+e^- pairs, which will also emit Bremsstrahlung radiation if it has enough energy and so on. A shower of electrons is therefore produced. The shower develops primarily in the direction of the initial incident particle. For showers produced by particles that have electromagnetic interactions only, the longitudinal development of the shower (how deep it penetrates) occurs on a scale of the radiation length of the material. For particles that can have nuclear interactions, the shower develops on the scale of the nuclear interaction length of the material. Because of Coulomb scattering a particle shower develops transverse to the incident particle. This lateral spread can be characterized by the Moliere radius mention in chapter 2.

The longitudinal shower shape of electrons was parameterized [44] using the form:

$$\begin{aligned} \frac{dE}{dz} &= Az^{\alpha}e^{-bz} \qquad (3.3) \\ \alpha &= (0.91 \pm 1.2) + (.449 \pm 0.27)\ln E \\ b &= ((-0.382 \pm 0.15) + (-0.0049 \pm 0.034)\ln E)X_0^{-1} \end{aligned}$$

X_0 is the radiation length of the calorimeter material. The parameterization agrees well with the data and Monte Carlo.

The longitudinal shower shape of hadronic showers in Load One was parameterized using the Bock [77] parameterization; see appendix A. The parameterization was used to simulate the leakage out the side of the IH module and was shown in figure 3.3-a. It appears to do reasonably well in accounting for the leakage. The difference in the data and the parameterization is probably due to the transverse shower shape, which is not taken into account in the parameterization; cuts on the longitudinal shower shape are excluding energy that would have otherwise been visible if the parameterized shower had a transverse dimension.

The transverse shower profile for electrons and pions have been also parameterized [44] for Load One with good results using double exponential fits, one exponential term of the fit to describe the core of the shower and the other term to describe the tails of the shower. An electron shower at its maximum transverse spread is 95% contained within a radius of 2.5 cm, which is approximately 0.25 radians in ϕ or η. Pion showers are more diffused; 90% of the energy of a pion shower is contained within a distance of about 5 cm of the shower centroid; whereas, it requires about 10 cm to contain 95% of the energy.

Pions can be discriminated from electrons by looking at the energy deposited in the various layers of the calorimeter and/or by characterizing the

shape of the particle showers by applying a covariant matrix method [45]; see chapter 4 on the measurement of electrons. For Load One both methods were studied [30]. By cutting on the ratio of hadronic energy (energy summed over the five layers of the IH module) to electromagnetic energy (energy summed over the four layers of the EM module), a pion rejection of 300 for an electron efficiency of 95% was achieved. This means that one out of every 300 pions is identified as an electron, and 5% of the true electrons are rejected as pions. The cut used for this rejection was a hadronic to electromagnetic fraction less than 0.02. With the covariant-matrix method a 72×72 matrix was used. The 72 variables correspond to 3×3 towers $\times$ eight longitudinal read outs (the four EM layers with four cells in finer segmented layer three and the first IH layer) per tower. For a 95% electron efficiency a combination of the two methods yielded an total rejection of 900 to 3000 for particles in the momentum range of 50 to 150 GeV/c.

3.6 Systematics and the Transferring the Calibration

The transferring of the calibration from the test beam to the DØ calorimeter was achieved by the use of a portable pulser which supplied a standard amount of charge at both the DØ and test beam's preamps. By measuring the response of the electronics at the test beam and at DØ to this standard charge, the response of the DØ calorimeter to particles of known energy can be deduced. In equation 3.4 the calibration process is represented.

$$\mathrm{E}_i^{\mathrm{D}\emptyset} = \frac{\mathrm{R}_i^{std-\mathrm{D}\emptyset} \times \mathrm{G}_i^{\mathrm{D}\emptyset}}{\mathrm{R}_i^{std-tb} \times \mathrm{G}_i^{tb}} \times \mathrm{E}_i^{tb} \tag{3.4}$$

Here $\mathrm{E}_i^{\mathrm{D}\emptyset}$ and E_i^{tb} are the energies measured in cell i at DØ and the test beam respectively. R_i^{std-tb} and $\mathrm{R}_i^{std-\mathrm{D}\emptyset}$ are the respective responses at the test beam and DØ to the standard pulser. And G_i^{tb} and $\mathrm{G}_i^{\mathrm{D}\emptyset}$ are the gains measured at the test beam and DØ. [46]

From looking at Z° DØ collider data, the EM energy scale was determined to be about 5% low; the Z° mass was measured at 86 GeV/c^2. To account for this discrepancy with the LEP value for the Z° mass, many systematic effects were studied in the analysis of the Load One, Load Two and DØ collider data. Systematic offsets in the pedestals due to electronic and pile up effects were studied. Variations over time in the gains due to changes in such environmental

factors such as temperature were characterized. The loss of response from the detector due to contamination of the liquid argon was investigated and measured. Also the effects of zero suppression were studied. Errors in the determination of the test beam momentum and their effect on the energy scale were considered. The effect of corrections (η dependent, ϕ crack...) to the energy scale were also investigated. How the upstream material at the test beam and DØ effects the energy scale and linearity was studied. Errors in the transferring of the calibration discussed above were also considered. Finally, the high voltage of the DØ calorimeter was reduced during the collider run from 2500 to 2000 volts, and the effect of this change to the response was characterized. The contribution of most of these systematic effects is small in terms of the energy scale. Taking almost everything possible into account, it was determined that the EM scale was 1.1% to 4.3% short of the "true" EM scale depending on which of the three DØ cryostats is in question [47]. This results in an 87 GeV/c^2 mass for the Z$^\circ$. It was decided that the EM scale would be corrected for the change in the high voltage which is a factor of 1.015 in the CC cryostat and a factor of 1.016 in the EC cryostats. In addition to this, it was decided to apply a multiplicative EM scale correction factor to obtain the LEP mass of about 91 GeV/c^2 for the Z$^\circ$. This factor was 1.072 for the CC cryostat, 1.025 for the EC north cryostat, and 1.012 for the EC south cryostat.

3.7 Summary of Calorimeter Calibration

In summary, the DØ calorimeter has proved to be very linear at energies greater than 10 GeV and deviated no more than 5% (but typically less than 2% [48]) from linearity at energies below 10 GeV. The response of the calorimeter was very uniform; away from cracks; the variations were less than 1%. Near cracks in the Uranium, the variations could be as much as 5% and 10% for cracks between modules. The calorimeter had a measured resolution in the energy for electrons of about $0.15\times\sqrt{E}$ and $0.5\times\sqrt{E}$ for pions. The position resolutions were on the order of 1 mm for electrons and 10 mm for pions. The study of the shower development of electrons and pions have shown that the calorimeter is behaving as expected. And the systematics are still being studied and have been shown so far to be small. Overall, the calorimeter is working very well and is an excellent device for the search of leptoquarks and other new phenomena. The correction to the EM scale does not have an impact on the usefulness of the calorimeter in the search for these particles.

Chapter 4

Data Selection

The search for a first generation leptoquark is based on 15 pb^{-1} of data collected during the 1992-1993 collider run at Fermilab. The accelerator reported a delivered luminosity of about 28 pb^{-1} giving DØ a dead time of about 46%. In order to obtain a workable set of data, the 15 pb^{-1} of data had to be reduced. The data was preselected by trigger cuts and loose cuts on off-line variables. Here, "off-line" refers to the processing of data, reconstruction, that occurs after the data is written to tape and usually occurs up to several days after the data is recorded. It is in the off-line processing that the various physics quantities such as transverse energy, $E_t = E \sin\theta$, associated with the various particles is determined with the highest precision. First, the full data set was preselected with cuts on various off-line quantities according to the physics interest of the entire DØ collaboration. This subset of data was reduced further with tighter off-line cuts specific to the various leptoquark signals to obtain a

workable set of events. For the two electron plus two jet signal, two EM objects, electron or photon, with E_t greater than 15 GeV for electrons and E_t greater than 10 GeV for photons were required. This sample includes the sample of Z°'s which will be used later to determine some efficiencies. For the electron plus $\not{E}_T$ plus two jets signal, one electron object with E_t greater than 15 GeV, one jet object with E_t greater than 15 GeV, a second jet object with E_t greater than 10 GeV, and $\not{E}_T$ greater than 20 GeV were required. After the trigger selection, described below, 14,780 of the two electron events and 11,480 of the electron plus $\not{E}_T$ events were left. The final off-line selection deals with various detector and physics background relative to the two signals.

4.1 The DØ Trigger and Filter Scheme

The DØ trigger scheme is divided into three levels and one sublevel. The Level Zero trigger comes from two sets of hodoscope counters mounted at the two ends of the calorimeter next to the beam pipe. These counters discriminate against beam-gas interactions. They also supply the next level of the trigger, Level One, with coarse vertex information and information on multiple interactions. Level One reduces the trigger rate from basically the crossing rate of about 300 kHz to about 200 Hz. The crossing rate, the number of times per second that a proton bunch intersects a bunch of antiprotons, from Level Zero

corresponds to a luminosity of about $5 \times 10^{30}\text{cm}^{-2}\text{sec}^{-1}$. For higher luminosities the interaction rate is greater than the crossing rate as multiple interaction come more into play. With the sublevel trigger, Level 1.5, the rate is reduced to no more than 100 Hz. The last level of the trigger system, Level Two, is the most complicated and it reduces the 100 Hz down to no more than 2 Hz, which is DØ 's maximum on-line data handling rate for writing data to tape.

4.1.1 Level One

The Level One trigger [49] [50] [51] is a hardware trigger and is divided into 31 sets of programmable trigger conditions. The conditions are thresholds on various detector variables. Some examples of these thresholds could be two EM trigger towers with E_t above 10 GeV, three jet trigger towers with E_t above 5.0 GeV, $\not{E}_T$ greater than 25 GeV, and many other similar conditions. The bandwidth for each of the 31 sets is determined by these thresholds. Table 4.1 list the various physics variables used for Level One plus Level 1.5. All the energy thresholds are in terms of E_t. A jet (or total) trigger tower includes energy from the first seven layers (about seven absorption lengths) of calorimetry; whereas, an EM trigger tower includes energy from the first four layers (about one absorption length) of calorimetry. The Level One variables are determined within 2.3 μsec of the beam crossing, where the beam crossing time

Table 4.1: Level One and Level 1.5 variables

Level-0 vertex information
–
muon P_t(transverse momentum) from Level 1.5
–
Number of muon tracks
–
Number of EM trigger towers above threshold
–
Number of jet trigger towers above threshold
–
Scalar $E_t = \sum \lvert E_t \rvert$
–
$\not{E}_T = \lvert \sum \vec{E}_t \rvert$

is 3.5 μsec. A better determination of muon momentum is done in Level 1.5 and is determined within 28 μsec.

The Level One decision process starts with the detector outputs. Coarse energy sums for the Level One trigger towers are made in the BLS's along with the precision readout. These energy sums get passed to faster versions of the ADC's called Flash Analog to Digital Converters (FADC). From the calorimeter, the coarsely (fast sampled) measured energy for all 1280 EM and 1280 hadronic (includes energy of the first three layers of hadronic calorimetry) trigger towers are passed into the Level One calorimeter trigger. A trigger tower is 0.2×0.2 in $\eta \times \phi$. The jet trigger tower energy is the addition of the EM trigger and hadronic trigger towers in a given 0.2×0.2 region. The global variables,

Scalar E_t and $\not{E}_T$, are calculated here by summing over EM and hadronic trigger tower E_t's. Included in these sums are only those trigger towers that have energy deposits above 0.5 GeV in E_t as measured by the calorimeter trigger electronics and have energy that is 2.5 standard deviations above the pedestals [52]. These global quantities and the trigger tower quantities are then compared to threshold criteria that are downloaded from the host computer. A series of bits are then generated containing the information on whether or not the calorimeter quantities satisfied the various threshold requirements. The generated bits from the calorimeter trigger and similar bits from the muon trigger and Level Zero are passed to the trigger framework where they are combined and compared to the 31 above mentioned trigger sets via an AND-OR network.

4.1.2 Level Two

The Level Two trigger, unlike the Level One trigger, is a software filter. For each of the 31 Level One triggers that are satisfied, a set of Level Two filters are called which are particle specific algorithms with various thresholds. For triggers using non-global calorimeter information, Level Two combines the η, ϕ information from a list of Level One trigger towers that have significant trigger energy with the energy information from the precision calorimeter readout for the $\Delta\eta \times \Delta\phi = 0.1 \times 0.1$ calorimeter towers associated with the trigger towers. Otherwise, all calorimeter information from the precision readout is

used, for example, in determining the $\not\!\!E_T$. This information along with similar information from the muon detector and trigger is passed to the Level Two particle algorithms for electrons, photons, jets, $\not\!\!E_T$, scalar E_t, muons, and taus.

The algorithms for the electron (photon is similar), jet, and $\not\!\!E_T$ are summarized as follows since only these objects are of relevance to a search for the first generation leptoquark. The electron algorithm [53] begins with a list of Level One EM trigger tower candidates. The precision readout tower (0.1×0.1 in $\eta \times \phi$) inside each Level One candidate with the highest E_t is found. This E_t includes the energy from the EM calorimetry and the first layer of hadronic calorimetry, the same as in the off-line electron finding algorithm. The E_t of a three by three array of towers (0.3×0.3 in $\eta \times \phi$) centered on this highest E_t tower is calculated. This quantity is taken as the E_t of the electron candidate after it has been corrected for the vertex z position. If the E_t of this candidate does not exceed a given threshold the candidate is rejected. If the candidate passes the E_t threshold, it is subjected to an assortment of longitudinal and transverse shape cuts. These cuts were tuned on test beam electrons (see chapter 3). Those candidates that pass these shape cuts can then be tested for isolation. For example, the energy inside a four by four array of towers but outside the three by three array must be less than 15% of the energy inside the three by three array. Finally, there can also be required a track

matching between the highest E_t tower and a central track within a specified distance. This track requirement was not used for the triggers considered in this leptoquark search. The photon filtering is essentially the same except for small variations in the shape cuts used, and tracking is not used.

The jet filtering [54] proceeds as follows. The jet algorithm starts with a list of Level One jet trigger towers which is ordered in E_t. This list of jet trigger towers is comprised of towers that pass the Level One thresholds. Starting with the first jet trigger tower, a cone of given radius in η, ϕ space is drawn about this tower. Most Level Two filters that require jets use a jet cone of radius R=0.7 (See section 4.2.2 below on reconstructed jets for the definition of R.) If the next trigger tower is inside this cone it is passed over. When a jet trigger tower is found outside any of the previously defined cones, it becomes the center of a new cone with the same given radius. When the list of jet trigger tower candidates is exhausted, a sum of the E_t of the $\Delta\eta \times \Delta\phi = 0.1 \times 0.1$ jet calorimeter towers inside each cone is added together to get the total E_t for each jet candidate. If two cones overlap, then the jet towers in the region of intersection are added into the energy sum of the jet candidate cone that was drawn first. The jet energy sums are then corrected for the vertex z position. The jet candidates are then required to pass a given E_t threshold.

The last two "particle" algorithms that will be described are the global quantities $\not{E}_T$ and scalar E_t [55]. For these two quantities the energy information from the entire calorimeter is used. The $\not{E}_T$ is constructed by a vector sum of the E_t of all the cells in the calorimeter and ICD. The scalar E_t is the scalar sum of the E_t of all the calorimeter and ICD cells. The cell E_t's are corrected for the vertex z position. Also used in these algorithms is a correction for anomalous "energy" deposits in the calorimeter. These "energy" deposits are believed to be caused by high voltage sparks and usually involve a single cell for a given event. The frequency and severity of these sparks varies widely, and they occur generally over the entire range of η and ϕ. Algorithms have been developed to find these "energy" deposits and eliminate their contribution to the $\not{E}_T$ and scalar E_t sums in both the Level Two code and the off-line code. Once the $\not{E}_T$ and scalar E_t energy sums have been computed, threshold cuts can be applied.

4.1.3 Triggers Used for Leptoquark Search

The following is a description of the triggers used in the leptoquark search. The triggers are divided according to the type of signal investigated. Listed in table 4.2 for each trigger are the Level One and Level Two conditions. The trigger thresholds and quality requirements were periodically changed during the 1992-1993 collider run. What is given in this table are the values used for the majority of the data taken. The Level One or Level Two thresholds for the electron terms changed by no more than 4 GeV for any of the three triggers used in the leptoquark analysis. The "major" change was in the two electron trigger, trigger A, where the requirements for Level Two given in table 4.2 were changed to two EM objects with $E_t > 10$ GeV with an isolation cut only. There were two additional Level One terms introduced into the triggers during the course of the run to solve the problem of the Main Ring noise. The first veto term is a simple gate from 0.1-0.5 seconds of the Main Ring cycle. During this time the protons are injected and proceed through "transition" (transition from non-relativistic to relativistic); the injection and transition produce large losses which need to be blanked out. This veto term was introduced into all the triggers. The second term is also a veto. This is the Main Ring Blanking (MB) [56] which is based on the accelerators signal of when beam is in the Main Ring at DØ and vetos events during the muon system's live time. Only some of the trigger which were considered to be sensitive to the presence of

Table 4.2: List of trigger used and their terms

Signal: LQ LQ $\rightarrow$ 2e + 2jets		
Trigger A:		
Object	Level One Terms	Level Two Terms
Electron	Two EM towers, E_t >7.0 GeV	Two EM objects, E_t >10.0 GeV with shape cuts One EM object with E_t >10.0GeV with shape and isolation cuts

Signal: LQ LQ $\rightarrow$ $\not\!\!E_T$ + e + 2jets		
Trigger B:		
Object	Level One Terms	Level Two Terms
Electron	One EM tower, E_t >10.0 GeV	One EM object E_t >20.0 GeV with shape and isolation cuts
$\not\!\!E_T$	—	Level Two $\not\!\!E_T$ > 20.0 GeV
Trigger C:		
Object	Level One Terms	Level Two Terms
Electron	One EM tower, E_t > 10.0 GeV	One EM object, E_t > 15.0 GeV with shape cuts
$\not\!\!E_T$	—	Level Two $\not\!\!E_T$ > 10.0 GeV
Jets	Two Jet Towers, E_t > 5.0 GeV	Two jet objects, E_t > 10.0 GeV with cone size = 0.3

the Main Ring particles have this veto; trigger B is one of them. The triggers with the MB term loose about 5% of the luminosity compared with triggers without the MB term.

4.2 Measurement of Electrons, Jets, and $\not\!\!E_T$

The search for first generation leptoquarks requires the measurement and identification of electrons and the measurement of jets and $\not\!\!E_T$. In what follows in

this section the off-line algorithms that are used in finding these objects will be described. Also some of the characteristics of these objects will be presented.

4.2.1 Electrons

The search for electrons begins with the clustering of calorimeter towers. To begin, the first electromagnetic (EM) tower, which includes the first five layers (the four layers of the EM calorimeter and the first layer of the hadronic calorimeter) of a full (jet) calorimeter tower, is selected from a list of such towers which are ordered in descending energy. Then the EM tower that is adjacent to this tower with the highest energy is added to the first tower. The highest energy EM tower that is adjacent to this second tower (excluding the first tower) is then added to the first two and so on. This adding of the highest nearest neighbor continues until the neighboring highest energy EM tower falls below 0.05 GeV. New clusters are found as energetic towers from the list that are not adjacent to the previously found clusters are encountered in the clustering algorithm. After the clustering, clusters with energy less than 1.5 GeV are dropped from the candidate list. Those clusters which have the fraction of their energy in the EM calorimeter less than 90% are rejected as candidates. An isolation cut is made by comparing the energy outside the central tower to that of the cluster; if the energy outside the central tower is greater than 60% of the energy of the cluster, the cluster is rejected as a candidate. The centroid

of the cluster is determined from a energy log weighted mean[57] of the cell positions in the third layer of the EM calorimeter where the η, ϕ segmentation is finer. This center of the cluster is used to determine a road in which if at least one track, coming from the primary vertex, is found in the cental tracking detector then the cluster is written into the electron candidate list. If no track is found inside the road, the cluster is written into a photon candidate list. This road is $\pm$ 0.1 radians about the centroid in ϕ. The road in θ (recall $\eta = -\ln(\tan(\theta/2))$) depends on the θ of the cluster center and the error in the z position of the vertex. For a cluster centered at $\theta = 90°$ or $\eta = 0.0$ the road has a minimum width of about $\pm$ 0.25 radians in θ. As the cluster is found at higher η's, the road becomes smaller; however, there is a set minimum in the θ road which is $\delta\theta_{min} = 0.1$ radians. The primary vertex mentioned is the vertex with the highest track multiplicity.

The above cuts constitute a first pass electron/photon analysis. Additional analysis to find a list of "golden" electrons was also done. The quantities that have been calculated and can be used are as follows. A more stringent isolation variable than the one discussed above is calculated from the energy contained within two cones of different radius, R, in η, ϕ space. This variable is calculated as the energy (sum of the four EM layers and the first hadronic layer) inside a cone of R=0.4 minus the electromagnetic energy (sum of the four EM layers) inside a cone of R=0.2 divided by the electromagnetic energy inside a cone

of R=0.2; Isolation = $\frac{\text{Energy}_{(R=0.4)}-\text{Energy}_{em}(R=0.2)}{\text{Energy}_{em}(R=0.2)}$. Another variable is the number of tracks inside the road defined above. This variable can be used to cut out events with jets faking electrons. Next is a quantity called the dispersion. This variable is the square root of the sum of the variances of the electron shower position in η and ϕ. These variances are associated with the log weighted mean mentioned above[57]. This dispersion gives a measure of the transverse spread of the electron shower; the larger the dispersion the wider the electron shower and the more likely the candidate is not an electron. The value of dE/dx of the track found in the road can be used to reject photons which convert to e^-e^+ pairs where the tracks of the two electrons are too close to be resolved. Also the distance of closest approach of the central detector track and the shower centroid can be cut on to reject, for example, π°'s that have associated low momentum charged particles. A related quantity is the track match significance defined as $\sqrt{(\frac{r\Delta\phi}{\sigma(r\Delta\phi)})^2+(\frac{\Delta z}{\sigma(\Delta z)})^2}$, where $r\Delta\phi$ and Δz are the distances between the shower centroid and central track respectively along the azimuthal arc and the $p\bar{p}$ direction, and $\sigma(r\Delta\phi)$ and $\sigma(\Delta z)$ are the respective errors in $r\Delta\phi$ and Δz. Finally, there is a H-matrix analysis[58],[59]

done on calorimeter information and event vertex position information from which a χ^2 like variable is determined. For a given event k, χ^2_k is calculated as:

$$\begin{aligned} \chi^2_k &= \sum_{i,j}(E^k_i - \langle E_i \rangle) H_{ij} (E^k_j - \langle E_j \rangle) \qquad (4.1) \\ H_{ij} &= C^{-1}_{ij} \\ C_{ij} &= \langle (E_i - \langle E_i \rangle)(E_j - \langle E_j \rangle) \rangle \end{aligned}$$

H_{ij} is trained on test beam electron data and plate level Monte Carlo electrons; specifically, C_{ij} is an average over several events at various energies of the electron for a given η. There are several choices for a set of variables E_i. The simplest H-matrix is one based on the longitudinal profile of an electron/photon shower. A set of E_i variables which was used for this type of H-matrix is described as follows:

E_1 = fractional energy in the first layer of the EM calorimeter
E_2 = fractional energy in the second layer of the EM calorimeter
E_3 = fractional energy in the third layer of the EM calorimeter
E_4 = fractional energy in the fourth layer of the EM calorimeter
E_5 = log(cluster energy); cluster energy includes EM layers plus first hadronic layer
E_6 = (vertex position Z)/σ_Z
σ_Z = error in Z

The fractional energies of the first four variables and the fifth variable allow the use of electrons at several energies to train the H-matrix. Other versions of the H-matrices take into account the transverse profile of the electron shower. These H-matrices hold more information about the typical electron and in principle are more efficient in identifying electrons. Although they are much larger and harder to manage, these larger H-matrices are preferred and in fact used. Since the transverse segmentation of the calorimeter diminishes at higher values of η, the dimensionality of these H-matrices also decreases at high η.

Not all of the above "golden" electron variables, which were described for completeness, were used in the leptoquark analysis. A description of which variables and how they were applied is given in chapter 5.

4.2.2 Jets

The jet finding algorithm that was used in the analysis of the data is based on a cone in η, ϕ space with radius $R = \sqrt{\delta\eta^2 + \delta\phi^2}$ where $\delta\eta$ and $\delta\phi$ are measured from the center of the cone. The energy of the jet is the energy contained within this cone. The algorithm proceeds as follows. First a list of jet calorimeter towers with energy is made in descending order of E_t. The tower E_t is vertex corrected. Here again, a calorimeter jet tower is a volume with a solid angle 0.1×0.1 in η and ϕ including all calorimeter layers. These towers are then grouped, starting with the towers with the highest E_t, into preclusters

of connected towers out to a radius of about R=0.3. Two precluster centers that are closer than R = 0.01 are combined. Towers with E_t less that 1 GeV cannot initiate a precluster or be included in a precluster. The η, ϕ center of the preclusters is now taken as the starting center of the jet cones. A new cone center is calculated by a E_t weighted mean of all tower positions within a cone of radius R about the precluster center. A new cone with radius R about the new position is determined, and the center is again calculated as before. The process is repeated until a stable center is found. [60] The total energy, transverse energy, and the cartesian components of the energy (energy and momentum are interchangeable) are calculated from the tower energies comprising the cone of radius R about this stable center. Also calculated is the fraction of the jet energy that was deposited in the EM calorimeter, the fraction of the jet energy that was deposited in the last layer of the hadronic calorimeter, and the ratio of the highest energy cell in the jet to the next highest energy cell. These last three quantities help in establishing any pathology for a given jet such as anomalous energy deposits due to high voltage sparks or jets that have a high degree of leakage out of the calorimeter. Unless otherwise noted, for the leptoquark analysis, a jet cone size of R=0.7 for the reconstructed jet is assumed.

The energy response and resolution of electrons and single pions to the DØ calorimeter was described in chapter 3. The response of the calorimeter to jets

is a more complicated matter. A jet energy scale has been determined [61] from actual data using E_t balancing for "two jet" events where one of the jets, a photon for example, deposits all of its energy into the EM calorimetry. One expects for such an event if the jet energies are perfectly measured no $\not{E}_T$. If there is a non-zero $\not{E}_T$, then one can assume that at least one of the jet energies was not measured well. One can further assume that the reason for this bad measurement is due to a reduced response of the full calorimetry to jets relative to the response of the EM calorimetry to electrons, photons or EM jets. With the assumption that the EM response is correctly calibrated, the energy of the jet that deposited all its energy in the EM calorimeter is assumed to be correctly measured. The $\not{E}_T$ of the event then gives a measurement of the absolute reduced response of the calorimeter to hadronic jets (from quarks). This measurement of $\not{E}_T$ is made as a function of η and uncorrected measured jet energy and is used to correct the response of the calorimeter to hadronic jets. The measured response of the calorimeter to jets at 25 GeV E_t is about 80% and increased to 88% for 200 GeV E_t jets. The jet energies were also corrected for zero suppression, out of cone, and underlying event effects. These additional corrections tend to bring closer the measured and predicted jet energies. A similar energy scale can also be derived by folding the response of electrons and pions from the test beam with the fragmentation function from a Monte

Carlo physics generator such as Pythia. The jet energy resolution derived from this method is about $70\% \times \sqrt{\mathrm{E}_{jet}}$ GeV [62].

4.2.3 Missing Transverse Energy

The missing transverse energy ($\not{E}_T$) is the quantity defined in equation 4.2.

$$\begin{aligned} \not{E}_T &= \sqrt{\left(\sum \mathrm{E_x}\right)^2 + \left(\sum \mathrm{E_y}\right)^2} \\ \mathrm{E_x} &= \mathrm{E} \sin\theta \cos\phi \\ \mathrm{E_y} &= \mathrm{E} \sin\theta \sin\phi \end{aligned} \tag{4.2}$$

Here the sum is done over all of the calorimeter cells that contribute energy above the zero suppression cutoff. Also note the sums are vector sums.

Events producing neutral weakly interacting particles will have $\not{E}_T$. Such an event might be a W boson decaying into an electron plus neutrino. For QCD two jet events one expects that the x and y components of the energy of the two jets to add to zero, giving no $\not{E}_T$. However, there are many factors which would give rise to a non-zero measurement of the $\not{E}_T$ for such an event. First, there are sampling fluctuations in the energy of a given jet. There is also the possibility of leakage of the very high energy jets out of the calorimeter. But most importantly, there are cracks and holes through which energy can escape. Therefore, there is a finite resolution in the measurement of $\not{E}_T$. One

method of quantifying this resolution is to measure the gaussian width of the distribution of $\not{E}_T$ for two jet events binned in a quantity called the scalar E_t.

$$\text{Scalar } E_t = \sum \sqrt{\left(E_x^2 + E_y^2\right)} \tag{4.3}$$

The function of $\not{E}_T$ resolution vs scalar E_t was parameterized with a second degree polynomial given in equation 4.4 [63].

$$\begin{aligned} \sigma_{\not{E}_T}(scalar\ E_t) &= A + B \times (scalar\ E_t) + C \times (scalar\ E_t)^2 \quad (4.4) \\ A &= 1.89 \pm 0.05\ GeV \\ B &= (6.7 \pm 0.7) \times 10^{-3} \\ C &= (9.9 \pm 2.1) \times 10^{-6}\ GeV^{-1} \end{aligned}$$

One hundred GeV mass, one electron plus $\not{E}_T$ leptoquark Monte Carlo events have an average scalar E_t of about 230 GeV which corresponds to about a 3.96 GeV resolution in $\not{E}_T$.

The electron scale correction mentioned in chapter 3 and the jet energy scale correction discussed above imply a correction to the $\not{E}_T$ due to these two corrections. The x and y components of the electrons and jets before the correction were added to the x and y components of the $\not{E}_T$. The components to the corrected electron and jet energies were then subtracted back from the $\not{E}_T$. The out-of-cone, zero suppression, and underlying event corrections for the jets were not added to the $\not{E}_T$. The $\not{E}_T$ ϕ was also corrected accordingly.

4.3 Off-line Selection

The off-line selection cuts for the two electron plus two jet sample are listed in table 4.3. The cuts used for the one electron plus $\not{E}_T$ plus two jet sample are given in table 4.4. The name of the cut, its value, and the number of events surviving after each cut are given in these two tables. In table 4.3 the detector background cuts refer to a set of cuts that eliminate events which are the result of electronic noise problems. In this case the specific problem is the anomalous deposits of energy, most likely from high voltage discharges, in the calorimeter which could fake jets. The cut used is as follows. If for a "jet" with E_t greater than 20 GeV, the fraction of electromagnetic energy (EMF) is less than 20%, then the event is rejected as having one of these anomalous energy deposits. The first five highest E_t "jets" are checked. Note here that a "jet" refers to a deposit of energy in the calorimeter which could have originated from a quark, electron, photon, or from electronic noise. Only a small fraction of real jets (originated by partons), about 3%, should have a EMF less than 20%. This cut is useful for those anomalous energy deposits that occur in the hadronic section of the calorimeter. For those that occur in the EM section of the calorimeter, that might fake an electron, the electron quality cuts, particularly the H-matrix cut, would eliminate these. The electron quality cuts are also intended to suppress QCD events with jets faking electrons. A jet can fake an electron by depositing most of its energy in the EM section of the calorimeter

which is possible when the jet contains mostly neutral pions, for example, that decay electromagnetically and hence produce electromagnetic showers. The quality cuts can also help in eliminating events with electrons emerging from the decay of b quarks; these electrons tend to be spatially close to the jet associated with the b quark decay and may fail the isolation cut.

The detector background and electron quality cuts deal with backgrounds that are due to mostly detector considerations rather than physics. The rest of the cuts are designed to eliminate the physics backgrounds. Requiring that there be two electrons with E_t greater than 25 GeV is a standard cut used for eliminating backgrounds from the Z° sample such as Drell-Yan production of electron-positron pairs, which are also backgrounds to leptoquarks. The two electron trigger used for the two electron plus two jet leptoquark search is about 100% efficient for Z°'s that pass the 25 GeV E_t cut on the electron and the electron quality cuts. After this cut the remaining sample contains mostly Z°'s, leptoquark candidates, and small backgrounds from QCD and Drell-Yan. The invariant mass distribution of the remaining sample is given in figure 4.1. Leptoquark events are also characterized by having at least two jets from the two quarks (more jets can come from initial state radiation or just the result of fragmentation of the final state partons) that come from the decay of the pair of leptoquarks. The data sample is required to have two jets with E_t greater than 25 GeV. The remaining sample should consist of Z° plus two jet events,

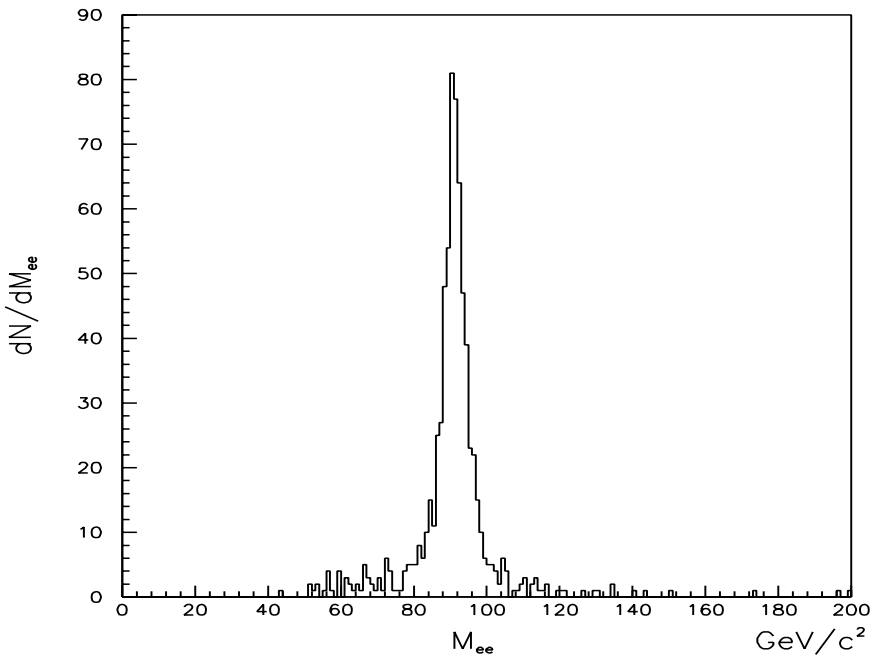

Figure 4.1: Invariant mass distribution of two electron data sample with 25 GeV cut on the electrons

leptoquark candidates, and very small if any backgrounds from QCD and Drell-Yan. The invariant mass distribution of these remaining events are shown in figure 4.2. It is clear from figure 4.2 that the invariant mass of these events are consistent with the invariant mass of the Z°. A cut of ± 10 GeV is made around the Z° mass peak which is approximately a 2.5 sigma cut. As a result no events are left in the two electron sample.

The detector background cuts for the electron plus $\not\!\!E_T$ plus two jet signal are more in number, and in combination they are a harsher cut than the ones for the two electron cut. The need for more detector background cuts for this signal is due to the $\not\!\!E_T$ term in the trigger which is a "magnet" for junk events

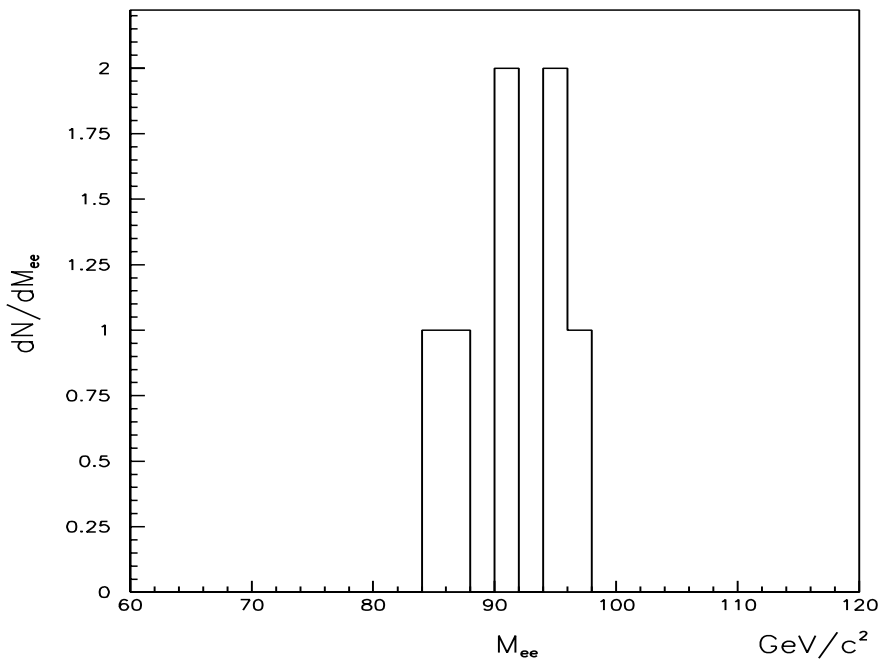

Figure 4.2: Invariant mass distribution of two electron data sample with 25 GeV cut on the electrons and jets

Table 4.3: Off-line cuts used for the two electron plus two jet sample

Number of events in initial sample = 14,780		
Cut Description	Cut Value	# Events
Detector backgrounds (electronic problems)	(see below)	14,119
Electron quality cuts:		1,040
Isolation for both electrons	< 0.15	—
Track match significance for highest E_t electron	< 10.0	—
Number of tracks for highest E_t electron	< 3	—
H-matrix χ^2 for highest E_t electron	< 100	—
H-matrix χ^2 for second electron	< 150	—
E_t for two electrons	> 25.0 GeV	725
E_t for two jets	> 25.0 GeV	7
Invariant mass of the two electrons	$81 < M_{ee} < 101$	0

coming from anomalous deposits of energy, events with Main Ring activity, or badly measured jets coming from, for example, jet leakage. In addition to the detector background cut described for the two electron case, there are four other types of cuts. First, if the $\not\!\!E_T$ is pointing within 0.15 radians of the direction or back-to-back direction of the Main Ring, provided that the $\not\!\!E_T$ is greater than 80 GeV, the event is removed. Events with Main Ring activity tend to have very large negative/positive deposits of energy in the coarse hadronic region of the calorimeter next to the Main Ring which goes through that part of the calorimeter. The last two detector background cuts are intended to reject those events that have anomalous energy deposits that occur inside an actual jet or simply have badly measured jets. For the first

three highest E_t "jets" with E_t greater than 50 GeV if the the ratio of the energy of the hottest jet cell with the next hottest cell is greater than 15.0, the event is rejected. For the two highest E_t jets (from quarks, i.e. jet list has had electron candidates removed) with E_t greater than 25 GeV, if the difference between the azimuthal angle, ϕ, of the jet in question and the $\not{E}_T$ is less than 0.45 radians, the event is rejected provided that the difference in the E_t of the jet and $\not{E}_T$ is less than 25 GeV. The electron quality cuts are the same as those for the highest E_t electron of the two electron sample. These again help in eliminating anomalous deposits of energy in the EM calorimeter and fake electrons from QCD.

The rest of the cuts are for rejecting physics backgrounds. Requiring an electron with E_t greater than 20 GeV is a standard cut for backgrounds to W coming from, for example, $b\bar{b}$ production. And whatever is background for W's is background for the electron-$\not{E}_T$ leptoquark signal. A standard $\not{E}_T$ cut for W's is also 20 GeV. The distribution for the transverse mass between the electron and $\not{E}_T$ for the remaining events in the electron-$\not{E}_T$ sample after the detector background, electron quality, and these two kinematic cuts is shown in figure 4.3 where one can see the characteristic transverse mass distribution of the W. Remember that this sample was preselected to have two jets with E_t greater than 15 and 10 GeV. To start eliminating the W background, the $\not{E}_T$ was required to be greater than 40 GeV. Two jets with E_t greater than 20

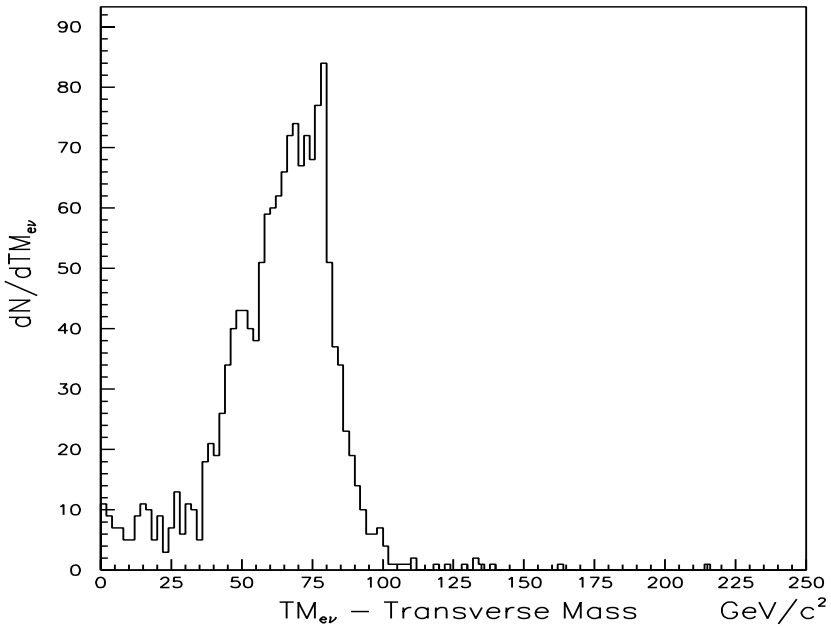

Figure 4.3: Transverse mass distribution of electron-$\not\!\!E_T$ data sample with 20 GeV E_t cut on electron, 20 GeV cut on $\not\!\!E_T$, and two jets with E_t of 15 and 10 GeV

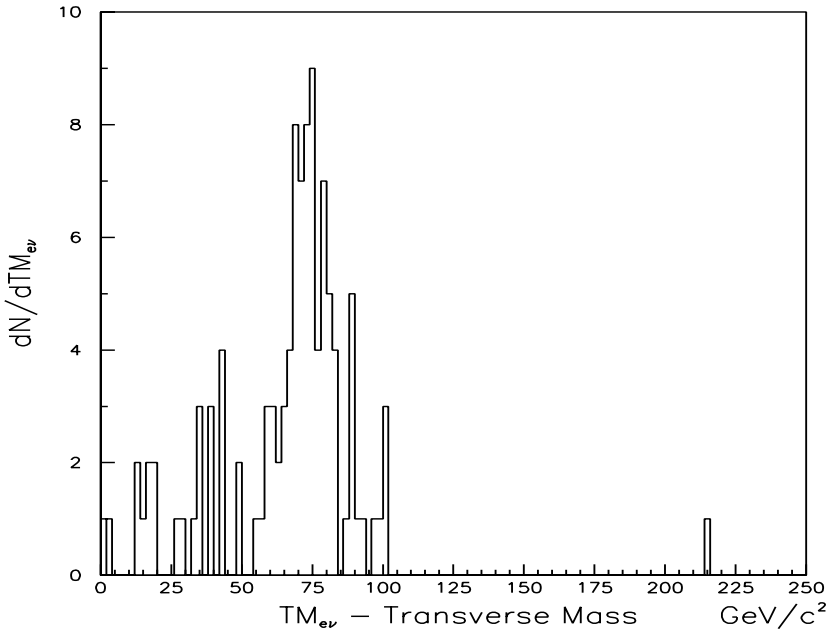

Figure 4.4: Transverse mass distribution of electron-$\not\!\!E_T$ data sample with 20 GeV E_t cut on electron and two jets and 40 GeV E_t cut on $\not\!\!E_T$

GeV are then required, and this cut greatly reduces the W background. What is left should be W plus two jet events, leptoquark candidates, and a small contribution from mostly QCD. As seen in the transverse mass distribution between the electron and $\not\!\!E_T$ shown in figure 4.4, almost all the remaining events have a transverse mass less than 105 GeV/c^2. Since a transverse mass of 105 GeV/c^2 is consistent with W's, a cut is made here, and one event is left. This remaining event contains a muon with E_t greater than 70 GeV, and muons with E_t greater than 15 GeV are rare in the first family leptoquark signals; therefore, a cut of 15 GeV for muons is made eliminating the last event.

Table 4.4: Off-line cuts used for one electron plus $\not\!\!E_T$ plus two jet sample

Number of events in initial sample = 11,480		
Cut Description	Cut Value	# Events
Detector backgrounds (electronic problems)	(see below)	5056
Electron quality cuts:		1691
Isolation	< 0.15	—
Track match significance	< 10.0	—
Number of tracks	< 3	—
H-matrix χ^2	< 100	—
E_t for electron	> 20.0 GeV	1570
$\not\!\!E_T$	> 40 GeV	425
E_t for two jets	> 20.0 GeV	98
Electron $\not\!\!E_T$ transverse mass cut	$TM_{e\nu} > 105$ GeV	1
No muons	E_t <15.0 GeV	0

Chapter 5

Analysis

The conclusion from the last chapter on the data selection was that there were no leptoquark candidates found in either the two electron or electron plus $\not{E}_T$ samples. With no candidates, a zero event upper limit on the leptoquark production cross section can be calculated, and with theoretical predictions on the cross section a lower limit on the mass can be determined. In what follows the efficiencies for the triggers, and the off-line cuts will be calculated from Monte Carlo and real data. These efficiencies along with the statistical and systematic errors will be used to derive the upper limit on the cross section. A choice of theoretical cross section will then be used to determine a lower limit on the mass of the leptoquark and this mass limit will be shown with its dependence on the branching ratio of the leptoquark into electron plus jet.

5.1 Monte Carlo

In order to set limits from data on physical quantities such as the mass for particles derived from theories beyond the standard model, the response of the detector to these new particles needs to be simulated in order to determine such quantities like the acceptance of the detector to these particles. The tools available for such a job are divided into two types of programs. The first group are the physics generators. These programs generate hard scatterings and subsequent production of various types of standard and non-standard particles. Some widely used generators are ISAJET, HERWIG [64], PAPAGENO [65] and PYTHIA [66]. The second group are the detector simulators. The most widely used is GEANT [67]. The DØ experiment has its own version of GEANT implementing the DØ geometry.

The ISAJET program and the DØ version of GEANT were used to generate Monte Carlo leptoquark event samples. These samples were pair produced, first generation leptoquarks which couple exclusively to first generation quarks and leptons. These samples were generated at leptoquark masses of 60, 65, 80, 90, 100, 110, 120, 140, and 160 GeV. The samples were also divided by the decay mode of the leptoquarks. The first set of samples contained two leptoquarks that each decayed into an electron plus jet. The second set has one leptoquark decaying into a charged lepton plus jet, and the other leptoquark decays into a neutrino plus jet.

There is no specific mechanism in ISAJET for producing leptoquarks, but there is a utility in ISAJET for producing supersymmetric squarks. As discussed in the theory section of chapter 1, the pair production of scalar leptoquarks is the same as that of squarks with the exception of gluino exchange in squark pair production. Therefore, by setting the mass of the gluino in ISAJET to a very high value, the production of leptoquark pairs can be simulated, and the leptoquarks can be forced to decay in any manner in which one wishes.

5.1.1 Distributions for Electrons, Jets, and $\not{E}_T$

It may be instructive to consider how the Monte Carlo signal and the real data compare in their electron, jet, $\not{E}_T$, and mass distributions. In the set of plots of figure 5.1 are the E_t distributions of the two highest E_t electrons and jets for the two electron plus two jet Monte Carlo, 100 GeV mass, leptoquark signal sample. The Monte Carlo GEANT raw data was processed with the full DØ reconstruction and a simulation of the DØ trigger. The distributions for the real two electron data sample with detector background and electron quality cuts is shown for comparison. The data preselection was applied to the Monte Carlo to make it and the real data as equivalent as possible in terms of kinematic constraints. Both the data and Monte Carlo distributions have been normalized to $d\sigma/dE_t$. The highest electron E_t Monte Carlo has a somewhat larger tail than the data and less so for the next highest E_t electron. But it is

in the distributions for the two highest E_t jets that the difference in the Monte Carlo and the data is more pronounced. It is the cut on the E_t of two jets that rejects most of the Z° background.

The set of plots in figure 5.2 are the corresponding E_t distributions to figure 5.1 for the one electron plus $\not{E}_T$ plus two jet Monte Carlo, 100 GeV mass, leptoquark signal sample and the electron plus $\not{E}_T$ data. The Monte Carlo distributions are not as distinctly harder than the data distributions as they are in the two electron case, and the background cuts are consequently less efficient for these variables. The cut on the transverse mass of the electron and the $\not{E}_T$ is the cut most responsible for eliminating the W background.

The invariant mass distributions for the two electrons in the two electron, 100 GeV mass, leptoquark Monte Carlo and two electrons data samples are shown in figure 5.3. Also shown in figure 5.3 is the transverse mass distribution for the electron plus $\not{E}_T$ leptoquark, 100 GeV mass, Monte Carlo and electron plus $\not{E}_T$ data samples. One can see the usefulness of using these variables in cutting the relevant backgrounds from the two leptoquark signatures.

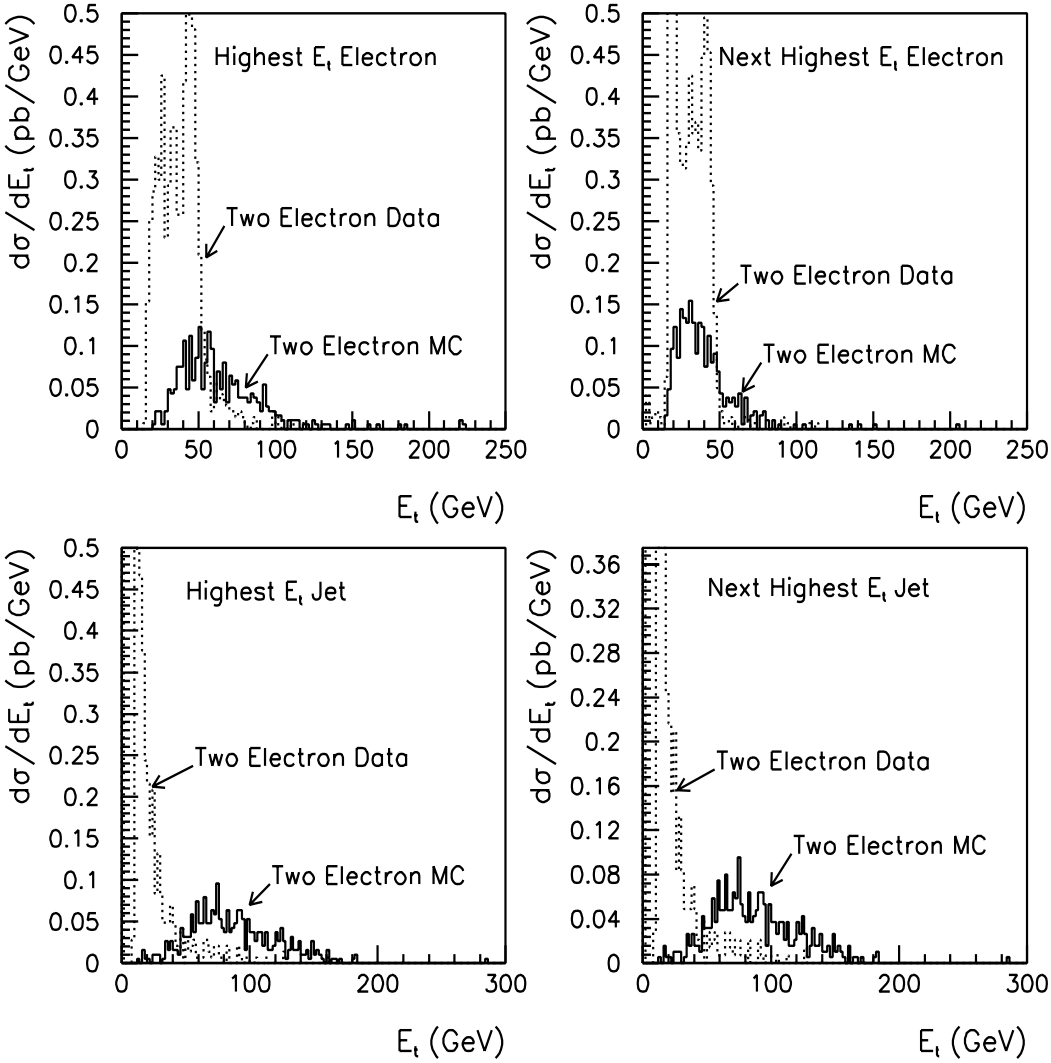

Figure 5.1: The 100 GeV, two electron plus two jet, Monte Carlo and two electron data distributions for the first two highest E_t electrons and jets

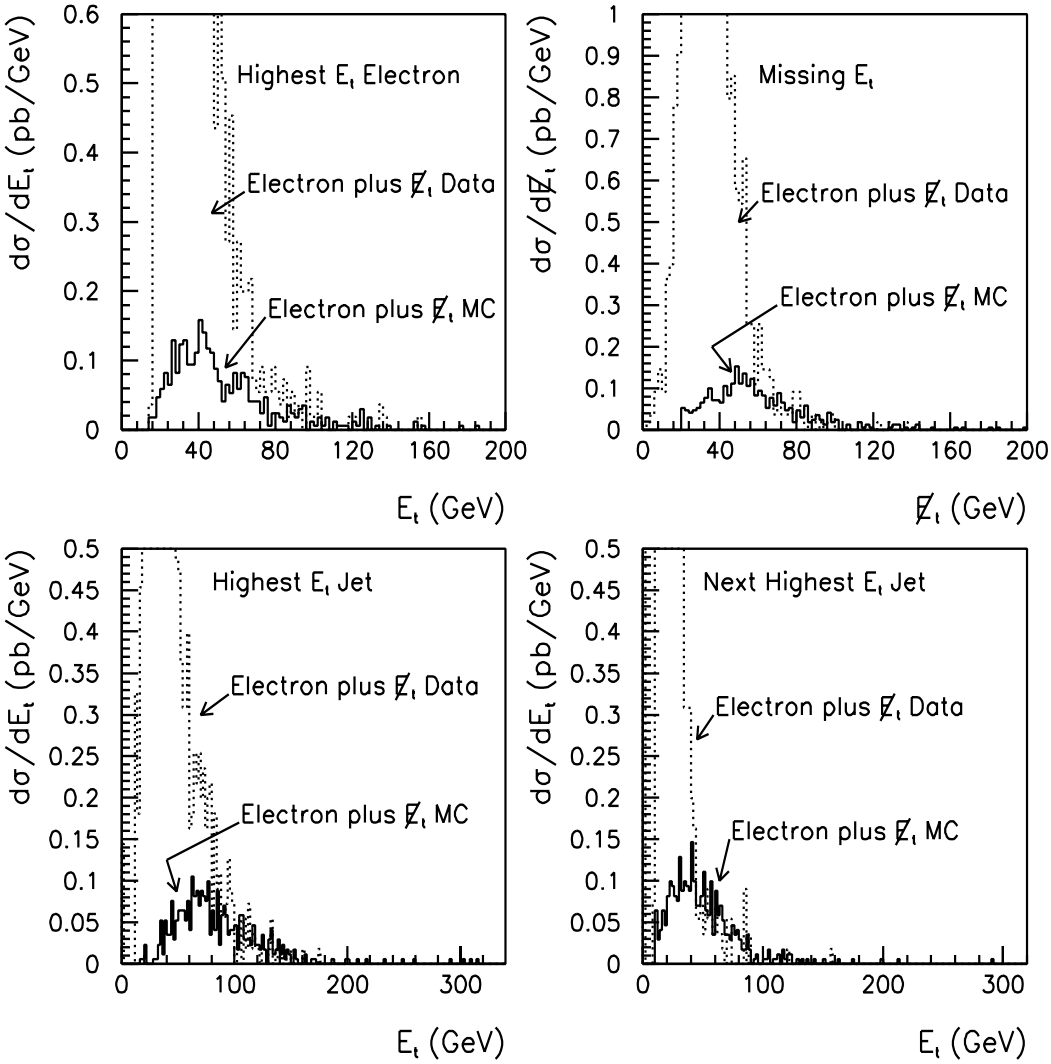

Figure 5.2: The 100 GeV, one electron plus $\not\!\!E_T$ plus two jet, Monte Carlo and electron plus $\not\!\!E_T$ data distributions for electron, $\not\!\!E_T$, and first two highest E_t jets

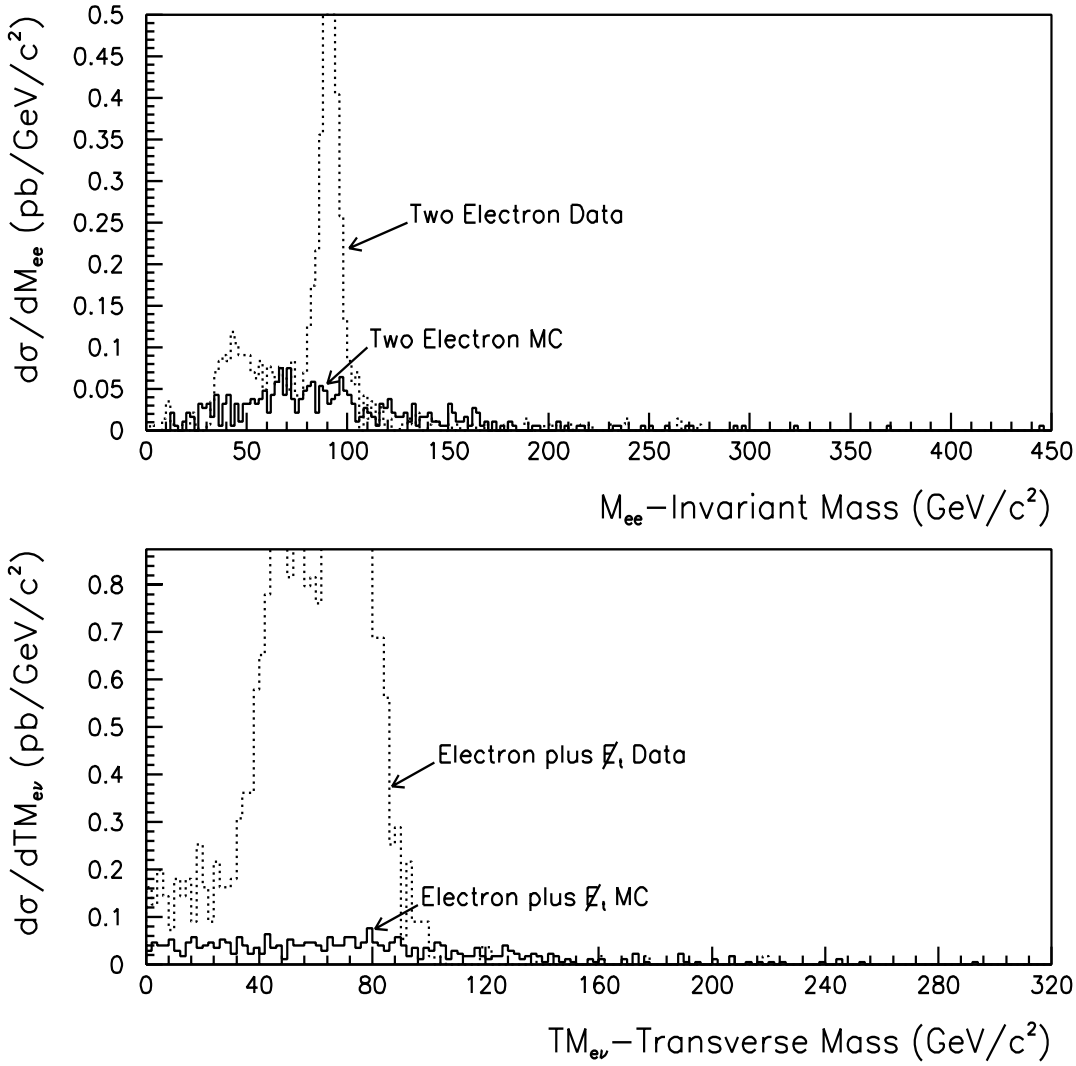

Figure 5.3: The invariant and transverse masses for the respective two electron and electron plus $\not{E}_T$, 100 GeV, Monte Carlo leptoquark and data samples

5.2 Efficiencies for a Leptoquark Signal

In terms of the efficiencies the cuts presented in chapter 4 are divided into two categories. The first is kinematic cuts and the second is quality cuts. The detector background, particle E_t, and angle cuts fall under the first category, and the off-line electron quality cuts and Level Two isolation and shape cuts fall under the second category. The reason for this distinction is that while the Monte Carlo represents real data well for such things as kinematic cuts, such quantities as jet and electron shapes are not as well mimicked; therefore, the quality cuts, which depend on the shapes of particles in question, and their efficiencies need to be studied using real collider data. The tracking efficiency must also be studied with collider data because the real detector environment is nosier than the Monte Carlo simulation due to the underlying event. Also the real tracking detectors suffer HV losses, gain fluctuations, and other hardware problems not present in the perfect world of the Monte Carlo.

5.2.1 Trigger Efficiencies

As mentioned before, the Monte Carlo leptoquark signal samples were processed with a simulation of the DØ trigger. Information on Level One trigger towers and global Level One quantities is provided as in collider data. Also Level Two information on electron and jet candidates and $\not\!\!E_T$ is given, the same as in collider data. This information can then be used to determine the efficiency of the leptoquark samples in terms of the DØ trigger. Specifically, the efficiency of the kinematic cuts in Level One and Level Two are determined. The kinematic thresholds used in Level One and Level Two were presented in table 4.2 for the three triggers used. The kinematic efficiencies, expressed in percent, after the Level One and Level Two cuts are given in table 5.1. The efficiencies take into account the shifts in the thresholds that occurred during the run, but the effect of these changes was small. The last column in table 5.1 is the efficiency for an event to pass both triggers B and C. The importance of this last number will be evident shortly. The binomial errors on these numbers are about $\pm$ 1.0%.

The efficiencies for the shape and isolation requirements in Level Two were determined from a sample of W events. First a sample of unbiased events with respect to electrons in Level Two was selected by requiring the events to pass a trigger which has a 20 GeV $\not\!\!E_T$ threshold at Level One and one Level One jet tower with E_t greater than 7.0 GeV. And the Level Two requirements were a

Table 5.1: Level One plus Level Two trigger kinematic efficiencies expressed as percent; errors are about 1%

Leptoquark Mass	Trigger A Efficiency	Trigger B Efficiency	Trigger C Efficiency	Trigger B∩C Efficiency
60 GeV/c^2	74	-	-	-
65 GeV/c^2	-	71	63	57
80 GeV/c^2	86	82	76	72
90 GeV/c^2	89	83	79	75
100 GeV/c^2	91	87	82	79
110 GeV/c^2	93	89	87	84
120 GeV/c^2	97	91	89	87
140 GeV/c^2	96	94	93	91
160 GeV/c^2	98	-	-	-

20 GeV jet object and $\not{E}_T$ greater than 25 GeV. The events were then required to contain at least one electron found with the off-line data reconstruction with E_t greater than 20 GeV and which passed the off-line quality cuts described in the chapter 4. These electrons were then matched to Level Two EM objects where the match was required to be within 0.1 radians in ϕ and η and within 10% in energy. One can then ask the question, which of these good electrons were matched to a Level Two EM object that passed the Level two shape or isolation cuts. The efficiencies were determined to be 98%±2% for the shape cuts, 96%±2% for the isolation cut, and 94%±2% for the combined isolation and shape cuts. For electrons with E_t greater than 20 GeV, the efficiency was independent of E_t within the errors.

The total trigger efficiency for the two electron channel is taken to be the product of the kinematic efficiency for trigger A with either the square of the isolation cut efficiency or the product of the shape only efficiency and the shape plus isolation efficiency since the Level Two quality cuts for this trigger were changed during the run as mentioned in section 4.1.3. The final trigger efficiency for the two electron channel is then the average of the two numbers just obtained, weighted by the luminosity collected under each condition.

The trigger efficiency for the electron plus $\not\!\!E_T$ channel is taken from triggers B and C. As indicated in table 4.2 trigger B had the shape plus isolation cut for a single electron, and trigger C the shape only cut. One can then construct the final trigger efficiency as follows. Let N_B represent the number of events that pass trigger B's kinematic requirements, N_C the number of events that pass trigger C's kinematic requirements, and $N_{B\cap C}$ is the number of events that pass both B and C's kinematic cuts. If ϵ_1 is the efficiency for the shape only cut and ϵ_2 is the efficiency for the shape plus isolation cut then the total number of events, N_{tot}, passing the two triggers can be written as:

$$\begin{aligned} N_{tot} &= N_B \times \epsilon_2 + N_C \times \epsilon_1 - N_{B\cap C} \times \epsilon_2 \qquad (5.1) \\ &\text{or} \\ \epsilon_{tot} &= \epsilon_B \times \epsilon_2 + \epsilon_C \times \epsilon_1 - \epsilon_{B\cap C} \times \epsilon_2 \end{aligned}$$

Table 5.2: The total trigger efficiencies in percent for the two electron and electron plus $\not\!\!E_T$ signal searches

Signal Sample	Trigger Efficiency (%)
two electron, 60 GeV	67.9±2.7
two electron, 80 GeV	78.8±2.1
two electron, 90 GeV	82.5±2.1
two electron, 100 GeV	84.7±2.0
two electron, 110 GeV	85.9±2.0
two electron, 120 GeV	89.5±2.0
two electron, 140 GeV	88.6±2.0
two electron, 160 GeV	90.6±2.0
electron-$\not\!\!E_T$, 65 GeV	75.5±1.7
electron-$\not\!\!E_T$, 80 GeV	83.6±2.1
electron-$\not\!\!E_T$, 90 GeV	84.7±2.2
electron-$\not\!\!E_T$, 100 GeV	87.6±2.3
electron-$\not\!\!E_T$, 110 GeV	89.9±2.2
electron-$\not\!\!E_T$, 120 GeV	91.0±2.2
electron-$\not\!\!E_T$, 140 GeV	93.1±2.1

Here ϵ_B, ϵ_C, and $\epsilon_{B\cap C}$ are the trigger kinematic efficiencies respectively for trigger B, C, and B∩C as given in table 5.1. The total trigger efficiencies for the two leptoquark signal searches are given in table 5.2.

5.2.2 Reconstruction Efficiencies

Again, the efficiency for the off-line kinematic cuts can be determined by applying them to the Monte Carlo. To determine the efficiency for the electron quality cuts and tracking, both the two electron (with photons) and electron plus $\not\!\!E_T$ preselected data samples, described at the beginning of chapter 4, were

used. To determine the electron quality cut efficiency, a sample of events with detector background cuts and two electrons with E_t greater than 20 GeV was selected from the two electron sample. The invariant mass distribution of the two electrons was then plotted and fitted from 60 GeV/c^2 to 120 GeV/c^2 with a Breit-Wigner plus first order polynomial functional form given in equation 5.2.

$$F(M_{ee}) = \frac{A^2}{(M_{ee}^2 - B^2)^2 + M_{ee}^2 C^2} + D \times M_{ee} + E \tag{5.2}$$

Here, M_{ee} is the two electron invariant mass; A is the square root of the overall normalization to the Breit-Wigner; B is the value of M_{ee} at the peak of the Breit-Wigner; C is the width of the Breit-Wigner, and D and E are respectively the slope and intercept of the straight line fit to the background. The fit is shown in figure 5.4 for the data before any quality cuts are applied. As seen in figure 5.4 the background to the Z° signal is substantial and is fit rather well with the straight line. One sees in figure 5.5 that after the quality cuts used in the two electron data selection described in chapter 4 are applied, the background is greatly diminished. The values of the parameters to the fits before and after the electron quality cuts are given in table 5.3. Also given in the table is the goodness of fit χ^2. The value of the parameter B in table 5.3 is about 91.2 GeV/c^2, the Z° mass, in all fits. The width of the Breit-Wigner for the two fits are almost within one standard deviation from each other. It was decided, to reduce the errors, to fix the value of parameter B to 91.2 GeV/c^2

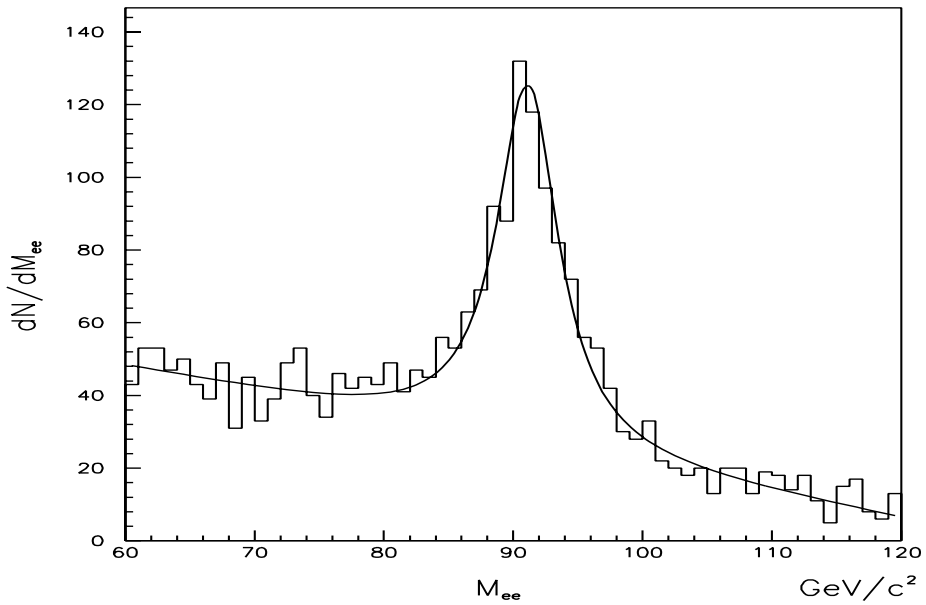

Figure 5.4: Breit-Wigner fit of two electron data before electron quality cuts

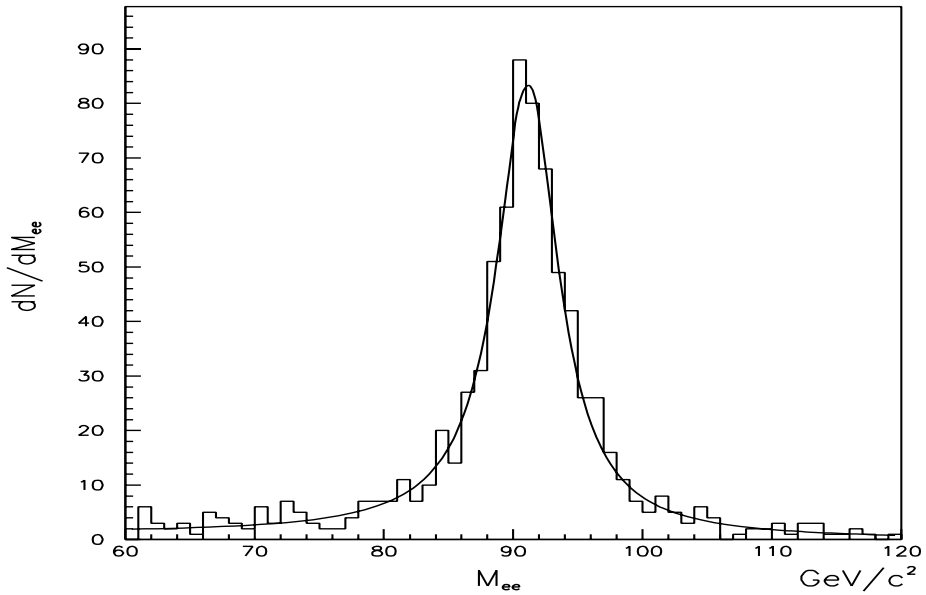

Figure 5.5: Breit-Wigner fit of two electron data after electron quality cuts

Table 5.3: Parameters for the fit of the Breit-Wigner function to two electron data for various electron quality cuts

Quality cut	A	B	C
None	5900±532	91.2±0.2	6.7±0.8
Isolation<0.15	5964±330	91.4±0.2	6.8±0.5
H-matrix χ^2 <100	5210±242	91.4±0.2	6.2±0.4
H-matrix χ^2 <150	5611±254	91.4±0.2	6.4±0.4
# tracks<3	5709±359	91.1±0.2	6.6±0.5
Track Significance<3	5319±289	91.3±0.2	6.1±0.4
Two electron signal combined quality cuts	4404±208	91.4±0.2	5.3±0.4
Electron-$\not\!\!E_T$ signal combined quality cuts	4356±210	91.3±0.2	5.4±0.4

Quality cut	D	E	χ^2
None	-0.68±0.04	86.5±4.4	1.0
Isolation<0.15	-0.30±0.03	37.3±2.9	0.93
H-matrix χ^2 <100	-0.03±0.01	3.3±1.3	0.64
H-matrix χ^2 <150	-0.05±0.02	5.6±1.5	0.68
# tracks<3	-0.42±0.03	54.9±3.4	0.90
Track Significance<3	-0.24±0.02	29.7±2.5	0.93
Two electron signal combined quality cuts	0.0±0.01	0.0±1.0	0.78
Electron-$\not\!\!E_T$ signal combined quality cuts	0.0±0.01	0.0±1.0	0.69

and the parameter C to a weighted by error average value of 5.8 GeV/c^2 and refit the distributions with only A, D, and E as free parameters. The value of the parameters for the new fit for the single and combined electron quality cuts are given in table 5.4 along with the goodness of fit, which changed little from the full fit. Note that the combined quality cuts applied to the one electron in the electron plus $\not{E}_T$ data sample during the data selection were applied presently to both electrons in the two electron sample in order to calculate the efficiency for the quality cuts in the electron plus $\not{E}_T$ data selection. This simply means that for the second electron, the H-matrix χ^2 cut was 100 rather than 150 as it is in the two electron data selection, and the tracking cuts were applied to the second electron as well. Also note that for the combined quality cuts for the two electron signal the fitted parameters were determined from a sample of Z°'s with E_t cut of 25 GeV on the electrons for consistency. The relevant parameter A for this case before the cuts was determined to be 5325$\pm$122 rather than 5299$\pm$132 given in table 5.4.

The efficiency for any cut would be the ratio of the number of true Z°'s after and before the cut. One can get the number of Z°'s, background subtracted, by integrating the Breit-Wigner portion of equation 5.2 with the fitted values of

Table 5.4: Parameters for the fit of Breit-Wigner to two electron data with reduced number of parameters

Quality Cut	A	D	E	χ^2
None	5299±132	-0.69±0.04	88.7±3.9	1.0
Isolation<0.15	5336±117	-0.30±0.03	38.9±2.7	1.0
H-matrix χ^2 <100	5001±104	-0.03±0.01	3.5±1.2	0.65
H-matrix χ^2 <150	5228±105	-0.05±0.01	6.1±1.4	0.72
# tracks<3	5182±125	-0.44±0.03	56.8±3.2	0.91
Track Significance<3	5144±115	-0.25±0.02	30.1±2.3	0.91
Two electron signal combined cuts	4634±104	0±0.01	0±1.0	0.81
Electron-$\not{E}_T$ signal combined cuts	4557±103	0±0.01	0±1.0	0.71

the parameters. The Breit-Wigner function was integrated using the method of calculus of residues and is given in equation 5.3.

$$\text{Area}(= \quad \#\text{events}) = \frac{2\pi A^2}{4B^2C - 2C^3} \tag{5.3}$$

Since the value of the parameters B and C were kept constant, the efficiency for a given cut is just the ratio of the square of the parameter A. The efficiency for the various electron quality cuts discussed are given in table 5.5. The efficiencies for the individual cuts are for the cuts applied to both of the electrons in the two electrons sample. To get the single electron efficiency take the square root of the double electron efficiency. The efficiency for the combined quality cuts in the two electron data selection is that given in table 5.5; however,

Table 5.5: Efficiency for electron quality cuts applied to both electrons in the two electron sample given in percent

Quality Cut	Efficiency	Error
Isolation < 0.15	100	6.8
H-matrix $\chi^2 < 100$	89.1	5.8
H-matrix $\chi^2 < 150$	97.3	6.2
# tracks < 3	95.6	6.6
Track Significance < 10	94.2	6.3
Two electron sample combined quality cuts	75.7	4.8
Electron-$\not\!\!E_T$ sample combined quality cuts	74.0	5.0

the efficiency for the one electron in the electron plus $\not\!\!E_T$ data selection is the square root of the number given in table 5.5 or 86.0±2.9%.

Since electrons are required to have tracks, an efficiency for finding these tracks must be determined. As mentioned in chapter 4 the preselected two electron sample also contained events with one photon and one electron or two photons. A certain number of electrons from Z° will be identified as photons if the tracking is not 100% efficient. By looking at the invariant mass distribution of two electron events and the one electron plus one photon events and counting the number of Z°'s in each distribution, one can determine the tracking efficiency. The two electron and one electron plus one photon distributions were fitted with equation 5.2. These distributions and their fits are shown in figure 5.6. Detector background cuts and electron quality cuts, H-matrix χ^2 and isolation, were applied to both data samples. Also an E_t cut of 25 GeV

Table 5.6: Parameters of fit of equation 5.2 to two electron and one electron plus one photon data

Sample	A	B	C	D	E	χ^2
Two electron	4829±228	91.5±0.2	5.8±0.4	0±0.01	0±1.0	0.91
Electron-photon	3439±256	90.9±0.3	6.4±0.6	-0.02±0.01	3.2±1.2	0.98

Table 5.7: Parameters from refit of equation 5.2 to the two electron and one electron plus one photon data with reduced number of parameters

Sample	A	D	E	χ^2
Two electron	4928±106	0±0.01	0±1.0	0.95
Electron-photon	3288±112	-0.03±0.01	3.6±1.1	0.97

was applied to both electrons and photons. The value of the fitted parameters are given in table 5.6 along with their goodness of fit. Again the value of the fitted mass of the Z° peak is averaged to 91.2 from both fits and the values of the parameters C are within one standard deviation. So the two distributions were refitted with the B parameter set to 91.2 and the C parameter set to the weighted average value of 6.03. The value of the parameters of the resulting refit with their goodness of fit are given in table 5.7.

The single electron tracking efficiency, given the number of Z°'s found in the two electron distribution and found in the one electron plus one photon distribution, is given by equation 5.4 where the number of two electron Z°'s is N_{ee} and the number of electron - photon Z°'s is $N_{e\gamma}$.

$$\epsilon_{track} = \frac{2}{\frac{N_{e\gamma}}{N_{ee}} + 2} \tag{5.4}$$

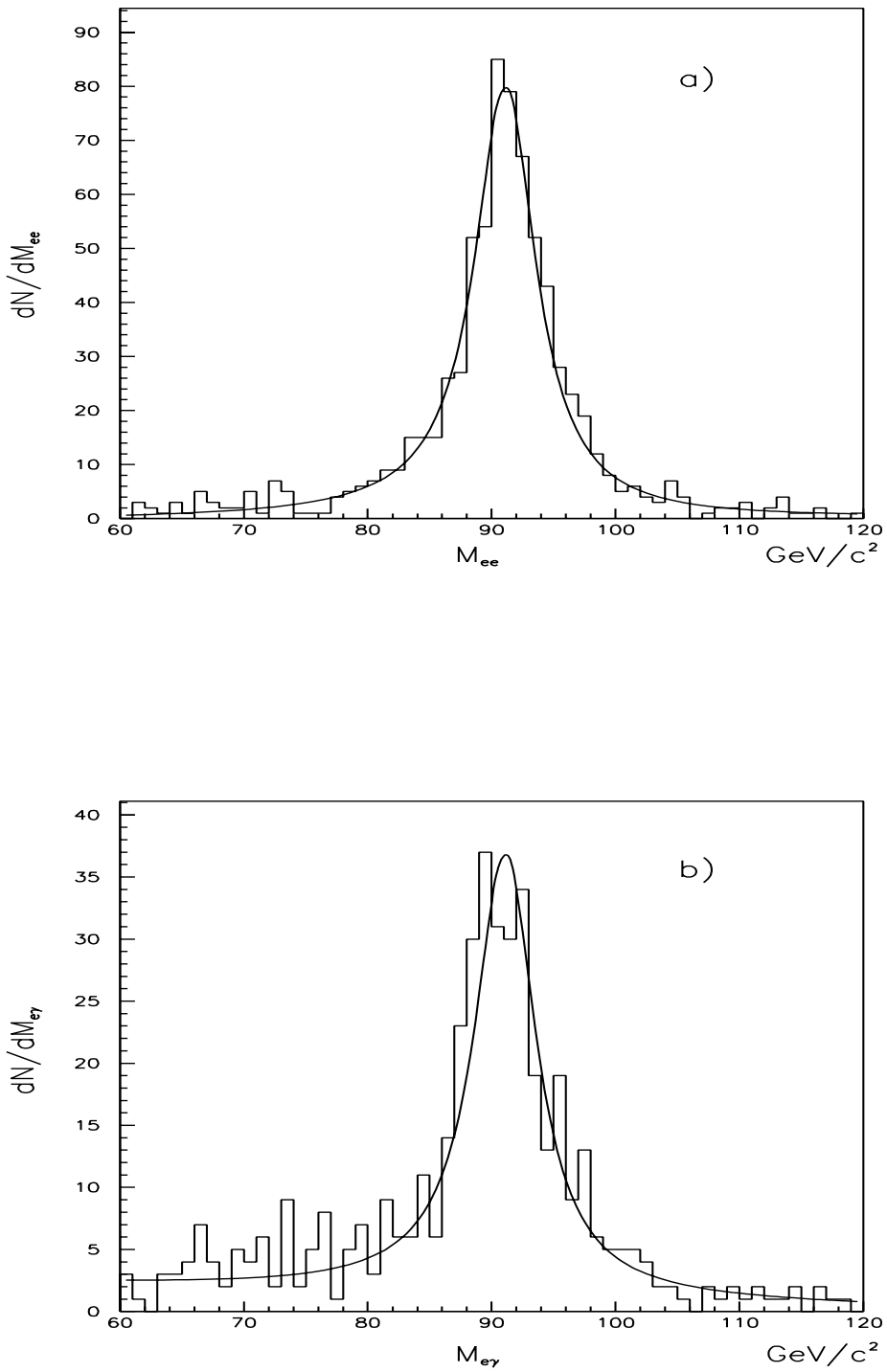

Figure 5.6: Z° mass plots used in tracking efficiency study: a) Two electron invariant mass distribution, b) One electron plus one photon invariant mass distribution

With the values of the parameters B and C in equation 5.3 fixed, the ratio $\frac{N_{e\gamma}}{N_{ee}}$ is equal $(\frac{A_{e\gamma}}{A_{ee}})^2$. Therefore, the single electron tracking efficiency is 81.8± 1.2%. Applying a 20 GeV cut on the electron and photons results in an efficiency that is not statistically different from the efficiency given.

Because in the Monte Carlo the tracking efficiency is not 100%, it is necessary to determine this efficiency and factor it out of the total efficiency when applying the tracking efficiency determined from the data. Following the same procedure as described for the data the single electron tracking efficiency was determined from a sample of Monte Carlo Z events. It was determined to be 95.0±0.74%.

The last consideration in determining the efficiency for the electron quality cuts is what happens to these cuts for a good electron as it gets closer to a jet. The efficiencies for the quality cuts were derived from a sample of Z° which consisted mostly of events with two electrons and no jets; whereas, leptoquark events have at least two jets in addition to the one or two electrons. For electrons, coming from leptoquarks, which are far enough away from any jet, which are most of the leptoquark electrons, the efficiency for the quality cuts calculated from the Z° sample is sufficient. However, this method may not be completely sufficient for those electrons near jets. In terms of calorimeter based quantities such as the isolation and H-matrix χ^2 variable, one would expect that as more energy from the jet overlapped with the energy of the

electron that these quantities would increase indicating a degraded electron quantity. This effect would become greater as a given electron and jet draws closer together or as the jet energy increases or electron energy decreases.

To study this effect the electron - $\not{E}_T$ sample was used. First, a subset of this sample was selected with the detector background cuts and a E_t cut of 20 GeV on the electron and the first two highest E_t jets to make the data sample look more like leptoquarks. The $\not{E}_T$ has a cut of 20 GeV from the preselection of the data discussed in chapter 4. Next, this subset of events is divided into two parts. The first part are those events that have the electron within 0.7 in R of any of the first four highest E_t jets. The second part consist of the remaining events. The idea is to see how the fraction of $R < 0.7$ events changes as the electron quality cuts are applied to the full subset. Two assumptions need to be made in order to make sense of the results. First, those good electrons with $R > 0.7$ are affected the same as those electrons from the Z° sample by the electron quality cuts. This is basically by definition. Secondly, the fake or bad electrons in either the $R > 0.7$ or $R < 0.7$ groups are effected the same by the quality cuts; that is to say that a fake electron in the $R > 0.7$ group is just as likely to fail one of the cuts as a fake electron in the $R < 0.7$ group. This second assumption was determined to be reasonably true by applying the isolation cut for those events of both groups that had an "electron" with a H-matrix value greater than 100; the fraction of $R < 0.7$ events remained constant

Table 5.8: The fraction of events in the R < 0.7 part of the W sample with detector background cuts and 20 GeV E_t cut on electron, jets and $\not\!\!E_T$ for each successive quality cut and efficiency for each cut

Quality cut	Fraction of R < 0.7 events	% Efficiency
None	0.201	–
Isolation < 0.15	0.123	61.5±6.9
H-matrix $\chi^2 < 100$	0.106	52.7±8.0
H-matrix $\chi^2 < 150$	0.114	56.7±7.6
# tracks < 3	0.101	50.2±7.95
Track Significance < 10	0.076	38.0±7.7

within errors. This assumption is at least is conservative. In other words the efficiency for good electrons near jets will be less if the fake electrons are also failing the quality cuts more often due to the presence of jets near them. So, if good electrons are unaffected by the close proximity of a jet, then the fraction of R < 0.7 events should remain unchanged as the electron quality cuts are applied. If the good electrons are being cut due to the presence of the jets, then the ratio of the fraction of R < 0.7 events after and before a given cut can be interpreted as the additional inefficiency for electrons that come within 0.7 in R of a jet. The fraction of R < 0.7 events before and after each successive quality cut is given in table 5.8. The number of events lost after each cut is cumulative. Also given are the efficiencies of the quality cuts due to the presence of jets. The efficiency for the H-matrix $\chi^2 < 150$ is for substituting this cut for the H-matrix $\chi^2 < 100$ cut; so, the cumulative efficiency for this cut includes in addition only the isolation cut. The efficiency quoted for the H-matrix χ^2 cut

of 150 corresponds to the additional efficiency for a second highest E_t electron coming near a jet. The efficiency quoted after the track significance cut of 10.0 is the additional efficiency for the highest E_t electron coming near a jet. This parallels the definition of the quality cuts for the highest E_t electron and second highest E_t electron. The same analysis was done with a tighter R cut of 0.5 and it was found that the efficiencies decreased as expected.

To determine the full and final efficiency for each of the leptoquark signal samples, each sample is divided into three sets. The first set has two electrons (one electron for the electron - $\not{E}_T$ leptoquark samples) that are isolated from the first four highest E_t jets, i.e. R $>$ 0.7. The next set has one electron that is not isolated, and the third has two electrons (for the two electron leptoquark sample) that are not isolated. The number of events surviving the kinematic cuts (trigger and off-line) was evaluated for each set of each sample. These are given in table 5.9. Column A is the total number of events in the sample. Column B is the number of events that pass the trigger and off-line kinematic cuts and have two electrons that are isolated (R$>$0.7). Column C is the number of events, weighted by the near-a-jet efficiency for one electron (38% for the highest E_t electron and 56.7% for the next highest E_t electron), that have one electron within 0.7 in R of any of the first four highest E_t jets with $E_t >$ 15 GeV and that passes the kinematic cuts. And column D is the number of events with two electrons within 0.7 in R of any of the first four highest

E_t jets with $E_t > 15$ GeV. The number of events in column D are weighted by the product of the near-a-jet efficiencies for the highest E_t electron and next highest E_t electron ($38.0\% \times 56.7\% = 21.5\%$). The near-a-jet efficiencies came from table 5.8. Column E is the total number of events surviving the kinematic cuts where the efficiencies for the Level Two shape and isolation cuts have been included. The errors in columns B through C come from the binomial errors in the kinematic cuts and the statistical error for the electron isolation weights. Column F is the percent total kinematic efficiency (including the Level two shape and isolation cut efficiencies) for each sample. The effect of near-a-jet efficiency is less than 10% in the total efficiency; therefore, the uncertainty in calculation of the near-a-jet efficiency has a negligible effect on the overall results even if the uncertainty is large.

The remaining efficiencies from the tracking (data and Monte Carlo) and electron quality cuts are lumped into two multiplicative factors, one for the two electron case and one for the electron -$\not{E}_T$ case. These are expressed in equations 5.5 and 5.6.

$$\epsilon_{ee}^{tot} = \left(\frac{\epsilon_{data}^{track}}{\epsilon_{MC}^{track}}\right)^2 \times \epsilon_{ee}^{\text{elec. qual.}} \tag{5.5}$$

$$= 0.56 \pm .04$$

$$\epsilon_{e\nu}^{tot} = \left(\frac{\epsilon_{data}^{track}}{\epsilon_{MC}^{track}}\right) \times \epsilon_{e\nu}^{\text{elec. qual.}} \tag{5.6}$$

Table 5.9: The (off-line and trigger) kinematic efficiency for leptoquark samples with weighting of portions of samples according to geometric isolation of electrons

Sample	A	B	C	D	E	F(%)
ee , 60 GeV/c^2	598	28±5.2	2.27±1.2	0.22±0.22	28.1±4.9	4.7±0.82
ee, 80 GeV/c^2	898	94±9.1	7.38±2.1	0.22±0.22	93.7±8.6	10.4±0.92
ee, 90 GeV/c^2	901	134±11	12.5±2.9	0.22±0.22	135±10	15.0±1.1
ee, 100 GeV/c^2	899	148±11	15.5±3.2	0.43±0.32	151±11	16.8±1.2
ee, 110 GeV/c^2	887	168±12	16.4±3.5	0.86±0.48	171±11	19.3±1.3
ee, 120 GeV/c^2	897	180±12	19.5±3.8	0.65±0.4	184±12	20.6±1.3
ee, 140 GeV/c^2	899	210±13	20.6±3.9	0.65±0.4	213±12	23.7±1.4
ee, 160 GeV/c^2	893	252±13	16.5±3.5	0±0	248±13	27.7±1.5
e-ν, 65 GeV/c^2	2874	42±6.4	6.1±2.0	-	47.0±6.8	1.64±0.24
e-ν, 80 GeV/c^2	1400	61±7.6	2.66±1.1	-	62.4±7.7	4.45±0.55
e-ν, 90 GeV/c^2	900	54±7.1	1.14±0.7	-	54.0±7.0	6.0±0.78
e-ν, 100 GeV/c^2	898	72±8.1	2.66±1.1	-	73.1±8.1	8.14±0.9
e-ν, 110 GeV/c^2	999	92±9.1	4.94±1.7	-	94.9±9.3	9.5±0.9
e-ν, 120 GeV/c^2	900	104±9.6	5.32±1.8	-	107±9.8	11.9±1.1
e-ν, 140 GeV/c^2	900	147±11	10.6±2.9	-	154±12	17.2±1.3

Table 5.10: Final efficiencies with total statistical errors for the leptoquark signal samples

Signal sample	A	B(%)	C(%)
Two electron, 60 GeV/c^2	ϵ_{ee}^{tot}	2.63±0.5	18.9
Two electron, 80 GeV/c^2	ϵ_{ee}^{tot}	5.82±0.66	11.4
Two electron, 90 GeV/c^2	ϵ_{ee}^{tot}	8.46±0.87	10.3
Two electron, 100 GeV/c^2	ϵ_{ee}^{tot}	9.47±0.95	10.1
Two electron, 110 GeV/c^2	ϵ_{ee}^{tot}	10.8±1.06	9.8
Two electron, 120 GeV/c^2	ϵ_{ee}^{tot}	11.6±1.1	9.6
Two electron, 140 GeV/c^2	ϵ_{ee}^{tot}	13.3±1.2	9.3
Two electron, 160 GeV/c^2	ϵ_{ee}^{tot}	15.5±1.4	8.9
Electron - $\not\!\!E_T$, 65 GeV/c^2	$\epsilon_{e\nu}^{tot}$	1.21±0.18	14.9
Electron - $\not\!\!E_T$, 80 GeV/c^2	$\epsilon_{e\nu}^{tot}$	3.28±0.42	12.9
Electron - $\not\!\!E_T$, 90 GeV/c^2	$\epsilon_{e\nu}^{tot}$	4.42±0.6	13.6
Electron - $\not\!\!E_T$, 100 GeV/c^2	$\epsilon_{e\nu}^{tot}$	5.99±0.7	11.7
Electron - $\not\!\!E_T$, 110 GeV/c^2	$\epsilon_{e\nu}^{tot}$	6.99±0.73	10.4
Electron - $\not\!\!E_T$, 120 GeV/c^2	$\epsilon_{e\nu}^{tot}$	8.76±0.88	10.0
Electron - $\not\!\!E_T$, 140 GeV/c^2	$\epsilon_{e\nu}^{tot}$	12.7±1.07	8.4

$$= \quad 0.74 \pm .03$$

The final efficiencies are given in table 5.10. Column A indicates the efficiency factor, equation 5.5 or 5.6, used in the calculation. Column B is the final percent efficiency. Column C is the total statistical error in percent defined as the error in the efficiency divided by the efficiency.

5.3 Error Analysis

In the previous section the total statistical errors were given. Their sources were binomial errors from the counting of events passing the kinematic cuts and the errors on the fits of the two electron and electron - $\not{E}_T$ data used to study the tracking and electron quality cut efficiencies. In order to calculate the upper limit on the cross section the systematic errors and error on the luminosity must be considered.

The systematic errors come from the uncertainty in the electron and jet energy scales and in the electron and $\not{E}_T$ resolutions since the resolutions in the MC are somewhat better than in real data. As discussed in chapter 4 the $\not{E}_T$ resolution was given as a second order polynomial. The error on the jet energy scale was determined to be about on average 9% for the two electron sample and 6% for the electron - $\not{E}_T$ sample. This was determined by changing the jet energy scale correction by the plus and minus errors on that correction and determining the average effect on the data. The uncertainty in the EM scale correction is small, about 0.4%. The resolution for electrons in the Monte Carlo is a little better than that measured from the data. An additional resolution of $0.051 \times \sqrt{\mathrm{E}_t}$ was added to the Monte Carlo electrons. The jet energy resolution in both the data and Monte Carlo is about the same; so, it is not included in the calculation of the systematic errors. Applying the errors in the jet energy scale, electron energy scale, and $\not{E}_T$ resolution to the background had no effect since

Table 5.11: Total errors for leptoquark signal samples in percent

Signal sample	Total error(%)
Two electrons, 60 GeV/c^2	23.6
Two electrons, 80 GeV/c^2	19.0
Two electrons, 90 GeV/c^2	16.6
Two electrons, 100 GeV/c^2	16.7
Two electrons, 110 GeV/c^2	16.3
Two electrons, 120 GeV/c^2	15.5
Two electrons, 140 GeV/c^2	15.3
Two electrons, 160 GeV/c^2	15.0
Electron - $\not\!\!E_T$, 65 GeV/c^2	24.0
Electron - $\not\!\!E_T$, 80 GeV/c^2	19.3
Electron - $\not\!\!E_T$, 90 GeV/c^2	19.4
Electron - $\not\!\!E_T$, 100 GeV/c^2	17.5
Electron - $\not\!\!E_T$, 110 GeV/c^2	16.2
Electron - $\not\!\!E_T$, 120 GeV/c^2	15.9
Electron - $\not\!\!E_T$, 140 GeV/c^2	14.9

the backgrounds are small. However, applying all the errors and resolutions to the Monte Carlo signal samples as shifts in the jet and electron energies and $\not\!\!E_T$, the systematic errors in the efficiencies were calculated to be between 3% and 15% for the electron plus $\not\!\!E_T$ signal sample and between 2% and 7% for the two electron signal sample. The smaller systematic errors correspond to the larger leptoquark masses.

The systematic error on the luminosity is reported to be 12% [68]. Adding the statistical and systematic errors in quadrature, the total error is given in table 5.11 in percent for each signal sample.

5.4 Upper Limit on leptoquark Cross Section

From Poisson statistics for zero events observed, the upper limit at 95% CL on the mean number of leptoquark events expected is 3.0 provided that there are no statistical or systematic errors. Then the upper limit on the cross section for leptoquark pair production for the two electron signature is given as :

$$\sigma = \frac{3.0}{L \times \epsilon \times \beta^2} \tag{5.7}$$

L is the integrated luminosity, ϵ is the total efficiency calculated for a given leptoquark Monte Carlo signal sample, and β is the branching ratio of a leptoquark into an electron plus jet (quark). Equation 5.8 shows the equivalent relation for the electrons plus $\not{E}_T$ signature.

$$\sigma = \frac{3.0}{L \times \epsilon \times 2\beta(1-\beta)} \tag{5.8}$$

To include the errors in the estimate of the upper limit on the cross section, one can consider the calculated value of L$\times\epsilon$ as an unbiased estimation for the mean of a gaussian distribution with a standard deviation equal to some error on L$\times\epsilon$, σ(L $\times$ ϵ). The fractional error on σ(L $\times$ ϵ), σ(L $\times$ ϵ)/L$\times\epsilon$, is equal to the total error given in table 5.11. This gaussian can be convoluted, integrating over the interval $-\infty <$ L$\times\epsilon < \infty$ (effectively $0 <$ L$\times\epsilon < \infty$), with the Poisson probability distribution function for zero events observed. From

this integration a modified Poisson probability distribution function for zero observed events results [69]. And from this function a modified value for the average number of events expected for any confidence level can be determined. The 95% CL upper limit on the mean number of events expected with no events observed is given in table 5.12. Also given in table 5.12 is the upper limit on the production cross section times β^2 for the two electron plus two jet signature and the upper limit on the production cross section times $2\beta(1-\beta)$ for the electron plus $\not{E}_T$ plus two jet signature. The integrated luminosity used was L=15pb^{-1}.

5.5 Lower Limit on Leptoquark Mass

The upper limit on the cross section for pair production of leptoquarks for the two electron plus jets signal vs leptoquark mass is plotted in figure 5.7 as the solid line. A 100% branching of leptoquark into electron plus quark was chosen. If a theoretical cross section for the pair production of scalar leptoquarks is over-layed on top of this as shown in the figure as a dashed line; then, the intersection of the two curves gives the lower limit on the mass of the leptoquark for a 100% branching into electron plus quark. In this case the lower limit on the mass is 139 GeV/c^2. For the theoretical cross section the KMRSB0 structure functions were selected, and the value of the momentum transfer was taken to equal the subprocess center of mass energy $\hat{s}$.

Table 5.12: The upper limit at a 95% CL for the number of events expected and the leptoquark production cross section times β^2 for each two electron plus two jet signal samples and the leptoquark production cross section times $2\beta(1-\beta)$ for the electron plus $\not\!\!E_T$ plus two jet signal samples

Signal Sample	# events	Upper Limit (pb)
Two electron, 60 GeV/c^2	3.31	8.39
Two electron, 80 GeV/c^2	3.18	3.64
Two electron, 90 GeV/c^2	3.13	2.47
Two electron, 100 GeV/c^2	3.13	2.20
Two electron, 110 GeV/c^2	3.13	1.92
Two electron, 120 GeV/c^2	3.11	1.80
Two electron, 140 GeV/c^2	3.11	1.56
Two electron, 160 GeV/c^2	3.10	1.33
Electron - $\not\!\!E_T$, 65 GeV/c^2	3.31	18.2
Electron - $\not\!\!E_T$, 80 GeV/c^2	3.18	6.47
Electron - $\not\!\!E_T$, 90 GeV/c^2	3.19	4.81
Electron - $\not\!\!E_T$, 100 GeV/c^2	3.15	3.51
Electron - $\not\!\!E_T$, 110 GeV/c^2	3.12	2.98
Electron - $\not\!\!E_T$, 120 GeV/c^2	3.12	2.37
Electron - $\not\!\!E_T$, 140 GeV/c^2	3.10	1.63

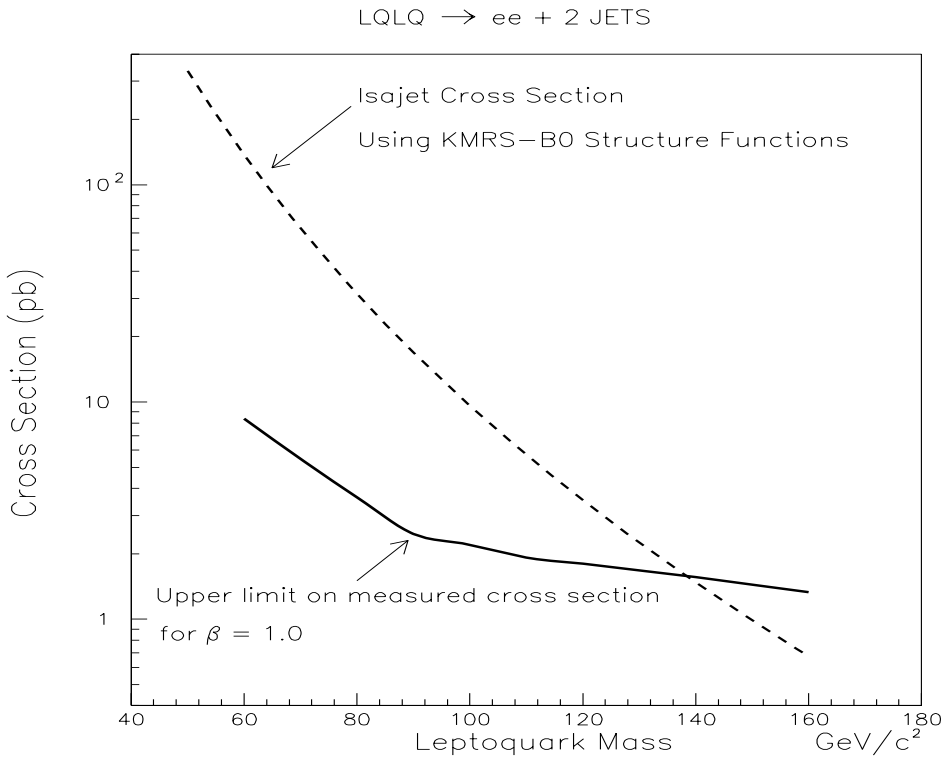

Figure 5.7: The upper limit on the cross section for the pair production of scalar leptoquarks for a 100% branching into electrons, $\beta = 1.0$, (for the two electron signature) vs the mass of the leptoquark is plotted as the solid line. Also plotted is the theoretical cross section as the dashed line.

For the electron plus $\not\!\!E_T$ plus jets signal the upper limit on the leptoquark cross section is plotted vs the leptoquark mass in figure 5.8. A 50% branching of leptoquark into electron plus quark was chosen for this case to show the lowest upper limit on the cross section. Again, the theoretical cross section is over-layed as the dashed line, and here the intersection of the two curves, 109 GeV/c^2, is the lower mass limit for a 50% branching of the leptoquark into electron plus quark for this signature.

By scaling the upper limit on the cross section by the appropriate factors of the branching ratio, the lower limit on the mass of the leptoquark vs branching ratio can be determined. Table 5.13 has the lower limits on the mass at various values of the branching ratio for both the two electron and electron - $\not\!\!E_T$ signatures. Also given in table 5.13 is the combined lower mass limit from the two electron plus jets and electron plus $\not\!\!E_T$ plus jets searches. The upper limit on the cross section was calculated according to equation 5.9.

$$\sigma^{combined} = \frac{\mathrm{n}^{avg}}{\epsilon^{eff} \times L} \tag{5.9}$$

where

$$\epsilon^{eff} = \beta^2 \times \epsilon^{ee} + 2\beta(1-\beta) \times \epsilon^{e\nu}$$

Here ϵ^{ee} is the total efficiency calculated from the two electron Monte Carlo leptoquark signal samples and $\epsilon^{e\nu}$ is the total efficiency calculated from the

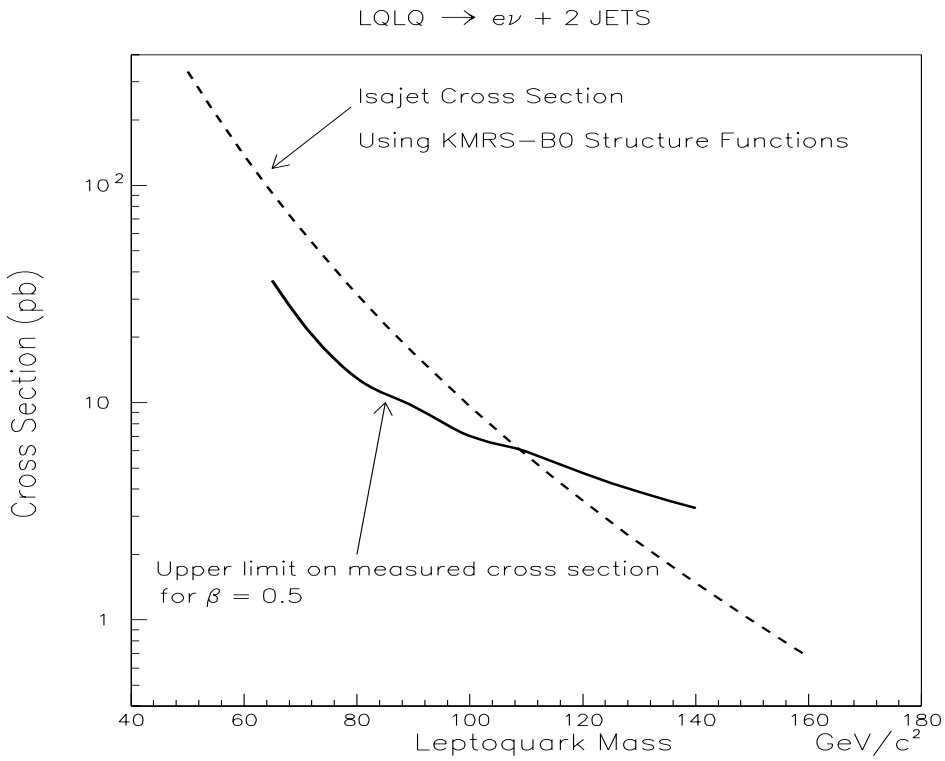

Figure 5.8: The upper limit on the cross section for the pair production of scalar leptoquarks for $\beta = 0.5$ (for the electron - $\not{E}_T$ signature) vs the mass of the leptoquark is plotted as the solid line. Also plotted is the theoretical cross section as the dashed line.

Table 5.13: Lower limits on the mass of the leptoquark for various values of the branching ratio β

β	2e signal (GeV/c^2)	e-$\not{E}_T$ signal (GeV/c^2)	Combined limit (GeV/c^2)
0.075	-	-	65
0.1	-	-	79
0.12	-	82	85
0.15	-	87	93
0.2	-	95	102
0.25	61	-	108
0.3	72	105	113
0.4	92	108	121
0.5	102	109	129
0.6	112	108	134
0.7	119	105	137
0.8	126	95	138
0.85	-	87	138
0.88	-	82	138
0.9	133	-	138
1.0	139	-	139

electron - $\not{E}_T$ Monte Carlo leptoquark signal samples. n^{avg} is the average upper limit on the number of events expected at a given leptoquark mass.

The numbers given in table 5.13 are plotted in figure 5.9 as branching ratio vs leptoquark mass. The regions in the β vs Mass space left of the three curves are the excluded regions for the two electron, electron - $\not{E}_T$, and combined limits. As one can see, the mass of the leptoquark from the combined limit is excluded up to 139 GeV/c^2 for a branching of 100% into electrons and 129 GeV/c^2 for a 50% branching into electrons. The value of the branching fraction has been excluded down to the value of 0.075 for a mass limit of 65 GeV/c^2.

5.6 Backgrounds

To complete the analysis a discussion of the backgrounds is needed even though no events were observed. If more background is expected passing the cuts than found, then there may be a problem with the analysis. As mentioned in chapter 4 the major background contributors to the two electron signal are Z°'s and γ^* plus two or more jets and QCD, where in events with four for more jets, two of the jets fluctuate into electromagnetic showers. For the electron plus $\not{E}_T$ signal the dominate backgrounds are W's plus two or more jets, QCD where one of the jets in a three or more jet event fluctuates into an electromagnetic shower and the energy of one or more of the jets is badly measured (or simply due to jet energy fluctuations) such that an significant $\not{E}_T$ is produced, and $b\bar{b}$

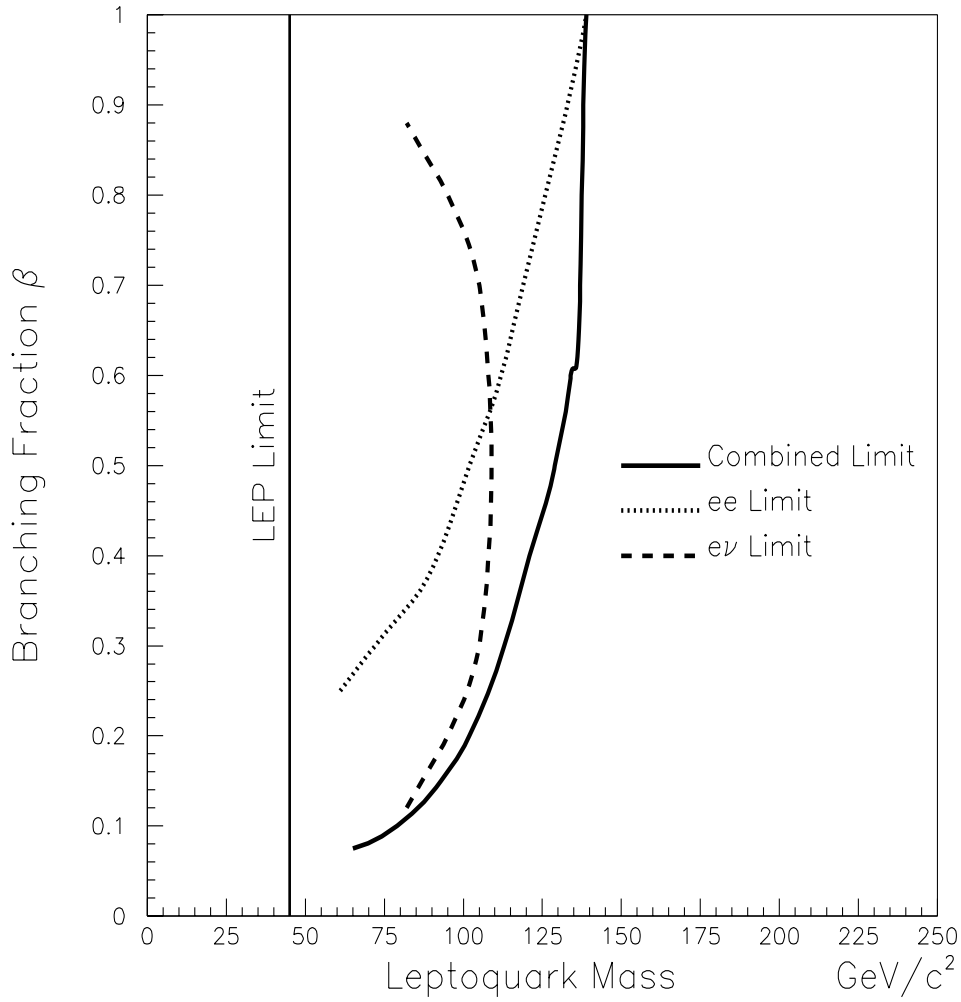

Figure 5.9: The branching ratio of leptoquark into electron plus jet vs leptoquark mass excluded region

production where the b's decay simi-leptonically. In order to try to estimate these backgrounds, Monte Carlo was used for the Z°'s, W's and b'S and real data was used for the QCD because it is very difficult to produce enough of the QCD background with Monte Carlo methods.

5.6.1 Monte Carlo Generated Backgrounds

Monte Carlo was used to estimate the backgrounds coming from Z°, γ^* plus two jets for the two electron plus two jet leptoquark signal. The physics generator used was version 3.67 of PAPAGENO, where Z° plus two jets and Drell-Yan plus two jet samples were generated. Each sample had a 25 GeV cut on the E_t of the electrons and the jets. The total cross section for the Z° plus two jet events with the 25 GeV E_t cuts was 0.71 pb. The total cross section with invariant mass between 81 and 101 GeV/c^2 was 0.70 pb leaving 1.0×10^{-2} pb outside this mass range. If the efficiencies for the electron quality cuts, tracking, and trigger were applied to the 0.70 pb, then with 15 pb^{-1} of data one would expect to see about 4.9 events. Seven events were seen in the data; this is reasonably close to the predicted value. Assuming a deficit in the Monte Carlo, all the cross sections from PAPAGENO for the Z° and Drell-Yan plus two jet events were scaled by the factor $7/4.9 = 1.4$ to estimate the number of background events to the two electron plus two jet leptoquark signal that should be expected after all the background cuts. The total cross section for

Drell-Yan plus two jet events with E_t cuts of 25 GeV on the electrons and jets with the invariant mass being outside of the range 81 to 101 GeV/c^2 was determined by generating samples of Drell-Yan plus two jet events at specific values of the invariant mass, which is how PAPAGENO generates Drell-Yan plus jet events. Masses that were a multiple of 10 were used. The value of the cross section between these masses were interpolated. The cross section for Drell-Yan plus two jets with invariant mass between 5 and 81 and between 101 and 200 GeV/c^2 were summed. The total cross section from Drell-Yan plus two jet outside of the 81 to 101 GeV/c^2 mass cut was 2.0×10^{-2} pb. The gives a total from Drell-Yan and Z°'s of 3.0×10^{-2} pb outside of the mass cut of 81 to 101 GeV/c^2. Multiplying by the above efficiencies and scale factor, one would expect 0.3 events in 15 pb^{-1} of data. This is consistent with the zero events seen. Lowering the E_t cuts to 20 GeV, two events from the data were found to pass the background cuts. The corresponding number of events predicted from PAPAGENO was 1.2 events.

The $b\bar{b}$ background was studied [70] using ISAJET Monte Carlo. From a sample of 350,000 $b\bar{b}$ events only 3 passed the kinematic cuts for the electron plus $\not{E}_T$ plus two jet signal search. The cross section for the 350,000 event sample was 14.3 nb. None of the three events passed the electron quality cuts. It was estimated that the quality cuts give an additional rejection factor of about 45 for electrons coming from the decay of b quarks. The 95% CL

number of events to expect in the 15 pb^{-1} of collider data is 3/350,000 $\times$ 14.3 nb $\times$ 15 pb^{-1} $\times$ 1/45 = 0.041 events.

5.6.2 Background Studies from Data

The expected number of events coming from QCD where one or more of the jets fluctuates into a fake electron must be derived from data. The probability for jets faking electrons has been studied [71]. For the quality cuts and E_t cuts used, the probability per jet of a jet faking an electron is about 1×10^{-3}. The cross section for four or more jets with E_t greater than 20 GeV is about 25×10^3 pb [72]. For two jets faking electrons this give in 15 pb^{-1} of data $10^{-6} \times 25 \times 10^3\,\mathrm{pb} \times 15\,\mathrm{pb}^{-1} = 0.04$ events. So, from QCD there are about 0.04 background events to the two electron plus two jet leptoquark signal, which again is consistent with the zero events seen.

For the electron plus $\not{E}_T$ plus two jet leptoquark signal, the QCD background comes in the form of one jet from a three or more jet event faking an electron and a badly measured jet producing sufficient $\not{E}_T$. The rejection factor for a three jet event giving $\not{E}_T$ greater than 40 GeV is about 100. The cross section for three jet events with a 20 GeV E_t cut on the jets is about 3.0×10^5 pb. So the number of event to expect in 15 pb^{-1} is

$10^{-3} \times 10^{-2} \times 3.0 \times 10^{5}$ pb $\times$ 15 pb^{-1} = 45 events. These 45 events are distributed in the transverse mass of the fake electron and $\not{E}_T$. They would tend to have a transverse mass less than 60 GeV. To get a fake electron - $\not{E}_T$ transverse mass above 105 GeV/c^2 would require at least a combined fake electron E_t and $\not{E}_T$ of 105 GeV. This would mean at least two orders of magnitude in rejection leaving at most a conservative estimate of about 0.5 events passing the background cuts.

The background for the electron plus $\not{E}_T$ leptoquark signal coming from W plus two jets was determined mostly from real data, but some help from Monte Carlo simulations of this background was also needed. Basically, an estimate for cross section for W plus two jet event with an E_t cut of 20 GeV for all objects was obtained from the measured cross sections in reference [73]. This estimate was 25 pb. The efficiencies for W plus two jets events for the kinematic cuts used in the electron plus $\not{E}_T$ plus jets leptoquark search (except the E_t cuts on the electrons, jets and $\not{E}_T$ already made on the W data) were determined from a sample of W plus two jet VECBOS [74] Monte Carlo. The electron quality cut efficiencies used are those already determined and presented. The total efficiency is 3.5 $\times$ 10^{-3}. In 15 pb^{-1} the number of W plus two jet events is then $25\,\mathrm{pb} \times 3.5 \times 10^{-3} \times 15\,\mathrm{pb}^{-1} = 1.3$ events. The total error on this estimate is rather large, about 48%.

5.6.3 Summary of Backgrounds

The background studies can be summarized as follows. The background to the two electron plus two jet leptoquark signature came mostly from Z° plus two jets, Drell-Yan plus two jets, and QCD with fake electrons. The sum total background expected from these sources was 0.34 events which is consistent with the zero events observed. The backgrounds for the electron plus $\not{E}_T$ plus two jet leptoquark signal were W plus two jets, $b\bar{b}$ production, and QCD with fake electron and $\not{E}_T$. The total expected background is less than 1.84 events. The error in these estimates is large, about one event; so, the 1.84 events expected is not inconsistent with the zero events seen.

Chapter 6

Conclusion

In conclusion, no signal for leptoquarks was observed in either the two electron plus two jet or electron plus $\not\!\!E_T$ plus two jet signatures for 15 pb^{-1} of data collected with the DØ detector at Fermilab. As a result a substantial portion of the β vs leptoquark mass space was excluded. Specifically, for a 100% branching of leptoquark into electron plus quark, $\beta = 1.0$, the least massive a first generation leptoquark can be is about 139 GeV/c^2. For $\beta = 0.5$ the mass limit is 129 GeV/c^2. The value of β has be excluded down to about 0.075 for a mass limit of 65 GeV/c^2.

This thesis has been devoted to the search for a *scalar* leptoquark. However, one may be more motivated to search for a vector leptoquark since all known forces are mediated by vector particles. The cross section for these vector leptoquarks is not readily available. However, theorist have begun to calculate the cross section and have found that it is somewhat larger than the cross

section for scalar leptoquarks. If the cross section for vector leptoquarks is assumed to be twice that of scalar leptoquarks, we could set a limit for vector leptoquarks also, since the signature and acceptance for the vector leptoquark should be very similar to that of the scalar leptoquark. The mass limit for a vector leptoquark given the present acceptance for scalar leptoquarks would be something around 150 to 160 GeV/c^2 depending on the branching fraction into electrons.

Before the turn of the next century with the implementation of Fermilab's main injector, yearly integrated luminosity in the hundreds pb^{-1} are expected. Either leptoquarks will be found with this amount of luminosity or the mass limits will be pushed to about 250 GeV with something like 500 pb^{-1} of data. If the discovery is not to be made at Fermilab then the SSC has a very good chance. Theoretical cross sections [75] at the SSC energy of 40 TeV are about a factor of four orders of magnitude greater than the cross sections at 2 TeV at a mass of 250 GeV/c^2. Indeed, the field is rich for the discovery of new physics at the SSC.

Appendix A

Parameterization of the Longitudinal Development of Hadron Showers in the D0 Calorimeter

The longitudinal development of hadronic showers was parameterized using the Bock parameterization [77]. The data used consisted of 75 and 125 GeV pions at a value of η of 2.3, and 50 and 100 GeV pions at an η of 2.55 for maximum shower confinement. These data were taken during the Load One test beam. The parameterization was minimized with respect to the data using MINUIT [76]. The fitted parameters were then used in the parameterization to simulate the data.

The following parameterization was used.

$$dE = \frac{E_0}{,(A)} W(s \cdot B)^{(A-1)} \exp^{-s \cdot B} d(s \cdot B) + \frac{E_0}{,(C)} (1 - W)(t \cdot D)^{(C-1)} \exp^{-t \cdot D} d(t \cdot D) \quad \text{(A.1)}$$

The parameters to be fitted are A, B, C, D, and W . The number of radiation lengths is s, and t is the number of interaction lengths, both measured from the origin of the shower. Therefore, the electromagnetic part of the shower is parameterized by the first term in the equation above, and the second term parameterizes the hadronic portion of the shower. , is the gamma function. E_0 is the total average energy determined from a gaussian fit to the data. The shower origin was fluctuated such that a distribution of such origins is an exponential decay shown in figure A.1. Here the probability that the shower starts at an interaction depth of λ, measured from the face of the EC EM, see figure 3.1, is proportional to $\exp^{-\lambda}$. Note that upstream interactions were excluded; hence, no showers began prior to the EC EM. Also note that the shower origin was randomly selected from the distribution of figure A.1 to use in the minimization of the parameterization. The length of the shower was also

Figure A.1: Distribution of shower origins as a function of interaction lengths

fluctuated by rescaling the values of s and t [78]. The rescaling was achieved as follows. First, two quantities were calculated as given in equation A.2.

$$
\begin{aligned}
g_1 &= \frac{\sum_{layer=1}^{9} E_{layer} X_0^{layer}}{\sum_{layer=1}^{9} E_{layer}} \\
g_2 &= \frac{\sum_{layer=1}^{9} E_{layer} \lambda^{layer}}{\sum_{layer=1}^{9} E_{layer}}
\end{aligned}
\tag{A.2}
$$

E_{layer} is the energy in a given layer, four EC EM layers and five EC IH layers, determined from 100 gev pion data. X_0 is the number of radiation lengths measured from the face of the EC EM to the end of the given layer and λ is

Figure A.2: Distribution of shower length rescaling factors: a) f_1, b) f_2

the corresponding number of interaction lengths. Therefore, g_1 and g_2 are the centroids of the longitudinal shower shape in terms of radiation and interaction lengths respectively. These two values were determined on a event by event basis, and distributions were made. These distributions were then normalized so that the average value of both distributions was 1.0. These renormalized distributions are shown in figure A.2. Numbers f_1 and f_2 were randomly selected from these distributions using, and these numbers were used to rescale s and t as follows.

$$s \Rightarrow s' = s/f_1, \quad t \Rightarrow t' = t/f_2 \tag{A.3}$$

It was determined that these normalized distributions were energy independent. The mean of the normalized distribution did not deviate from unity by

more that 2% when determined from pion data of varying energy. Hence, the distributions determined from the 100 GeV data were used in fitting the other data.

Equation A.2 was numerically integrated in the manner indicated by equation A.4.

$$E_{layer}^{parameterized} = \sum_{i=1}^{N} \left(dE_i^{em}(s_i')\Delta s_i' + dE_i^{had}(t_i')\Delta t_i' \right) \tag{A.4}$$

Here $\Delta s_i'$ and $\Delta t_i'$ are respectively the radiation and interaction lengths of one plate of absorber material and two gaps of active material except in the first interval of IH layers one through four where additional length was added to account for stainless steal plates found in front of each of the layers just mentioned. N is the number of intervals in each layer, N = 2, 2, 6, 8, 15, 15, 15, 15, 13 corresponding to the nine layers of the Load One. s_i' and t_i' are determined at the center of each of the intervals.

So, the procedure is to select a shower origin, select rescaling factors, and calculated the energy per layer. This is repeated a few thousand times. An average parameterized energy is then calculated for each layer. An average energy per layer is also calculated from the data which was cut to exclude

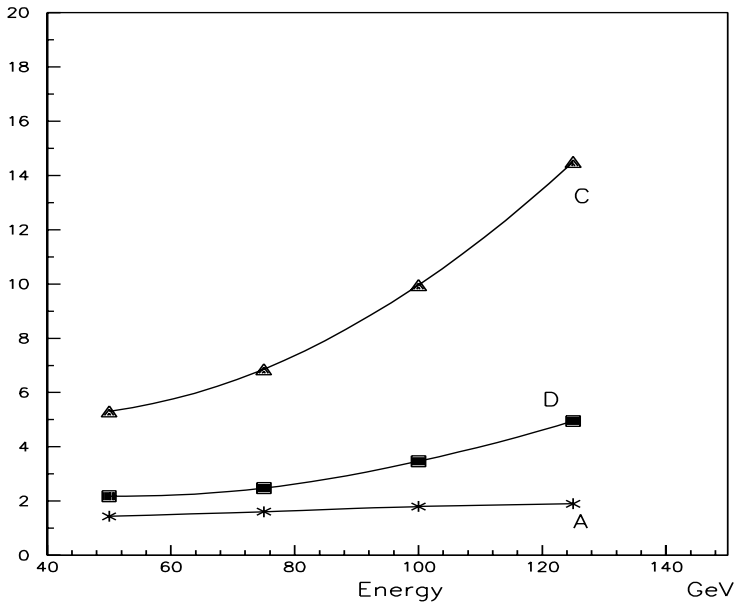

Figure A.3: Values of the parameters A, C and D as a function of energy

upstream interactions. The following value is calculated and minimized by MINUIT.

$$val = \sum_{layer=1}^{9} \left(\bar{E}_{layer}^{data} - \bar{E}_{layer}^{parameterization}\right)^2 \Big/ \bar{E}_{layer}^{parameterization} \tag{A.5}$$

The above procedure was done separately for the 50, 75, 100, and 125 GeV pion data runs. The results are given in figure A.3 and table A.1. After completing the 50 and 100 GeV fits, it was seen that the parameters b and w were constant within errors. Therefore, these parameters were fixed in the fit of the 75 and 125 GeV data, where good fits were obtained. The errors from the fit greater than 1% are indicated in parenthesis in table A.1. An energy

Table A.1: Fitted parameters at various energies

Energy(GeV)	A	B	C	D	W
50	1.44	0.110(0.006)	5.31	2.18(0.08)	0.69(0.02)
75	1.61	0.11(-)	6.86	2.48(0.04)	0.69(-)
100	1.80	0.110(0.003)	9.96	3.47(0.08)	0.70(0.01)
125	1.90(0.02)	0.11(-)	14.5	4.95(0.05)	0.69(-)

Table A.2: Parameter $= C_1 + C_2 \times E + C_3 \times E^2 + C_4 \times E^3$

Parameter	C_1	$C_2 \times 10^3$	$C_3 \times 10^5$	$C_4 \times 10^7$	error
A	1.18	3.13	5.44	-2.67	$\pm$0.01
B	0.110	-	-	-	$\pm$0.005
C	6.025	-59.7	83.1	15.0	$\pm$ 0.0001
D	4.75	-104.0	119.0	-27.7	$\pm$0.054
W	0.690	-	-	-	$\pm$0.015

dependent parameterization for parameters A, C, and D was determined by fitting a third degree polynomial to the parameters as functions of energy, as seen in figure A.3. A general parameterization of the Load One data is presented in table A.2. Energy E is in units of GeV, and the error is the overall error for each parameter.

The energy deposited per interaction length for each of the nine layers and for each of the four energies is shown in figure A.4. The open circles connected by a line are the data, and the asterisk are the parameterization. There is good agreement between the data and the parameterization. The shower reaches its maximum dE/dλ in EM layer four. Note that the value of dE/dλ for the last IH layer for 50 GeV pions drops below the value one on the log scale; the values

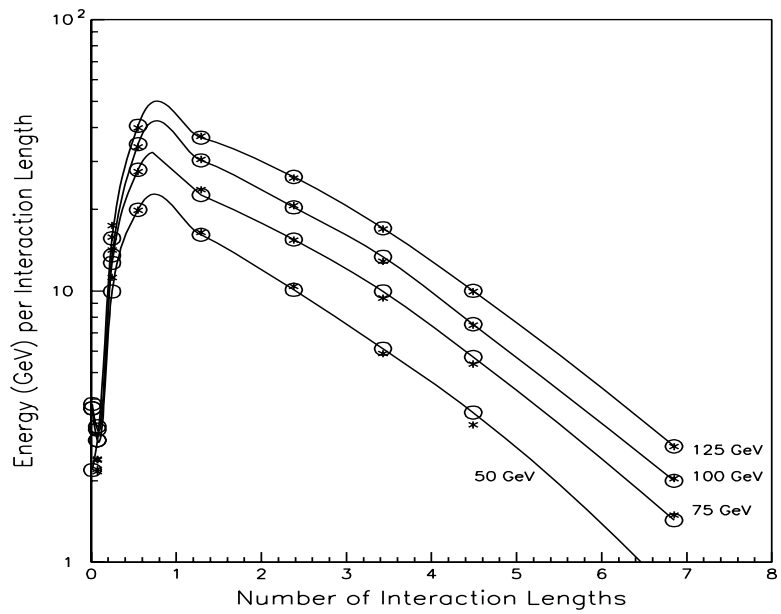

Figure A.4: Longitudinal development of hadronic shower

are 0.77 GeV per unit interaction length for the data and 0.85 GeV per unit interaction length for the parameterization.

A simulation was done using the parameterization. The parameters fitted to the pion data were taken and used in equation A.2 to generate 'events'. A shower origin was randomly selected as before. Also shower length rescaling factors were randomly selected as previously discussed. Then equation A.2 was integrated to give the energy for each of the layers. If the layer was upstream of the shower origin, it received an energy of zero. Sampling fluctuations were introduced by smearing separately the electromagnetic and hadronic energies in each of the layers according to Gaussian distributions with sigmas of $0.17/\sqrt{E_i^j}$

and $0.59/\sqrt{E_i^j}$ respectively. Here E_i^j is the hadronic or electromagnetic energy of the jth interval of layer i. The 0.17 and 0.59 constants along with a cutoff of 77.2 adc counts (0.303 GeV) for E_i^j were chosen to reproduce the total energy resolution of the 100 GeV pion data. If E_i^j is less than the cutoff then the energy is not smeared. The resolution was most strongly dependent on the cutoff which needed to be set lower in simulating data at lower energies. The electromagnetic fraction of the shower was also fluctuated by randomly selecting the value of the w parameter such that the distribution of selected w's is a gaussian distribution with a mean equal to the fitted value of w from MINUIT. The width of this distribution of w's was selected to give the best visual comparison to the data. A sigma of 0.2 for 100 GeV pions was used. The introduction of these fluctuations into the parameterization introduced less than a percent change in the mean total energy and no more that a 3% change in the mean energy in some of the layers with the largest deposits of energy. The parameterization and the actual data for 100 GeV pions are compared in figures A.5 and A.6 for IH layers one and two, respectively, near the shower maximum.

The parameterization reproduces the data well in the mean energy deposited in the various layers of the Load One configuration and, with the various fluctuations introduced, gives good agreement in the distribution of

Figure A.5: IH layer one: comparison of data and parameterization

Figure A.6: IH layer two: comparison of data and parameterization

energy in the layers. Also with these fluctuations, the energy resolution was reproduced.

Bibliography

[1] Ta-Pei Cheng and Ling-Fong Li. *Gauge theory of elementary particle physics.* Oxford: Clarendon Press, 1988

[2] J. C. Pati and Abdus Salam. "Leptonic Number as the Fourth 'Color'". Physical Review D 10 (1974) p.275.

[3] W. Buchmüller and D. Wyler. "Constraints on SU(5)-Type Leptoquarks". Physics Letters B 177 (1986) p.377.

[4] V. D. Angelopoulos *et al.* "Search for New Quarks Suggested by the Superstring". Nuclear Physics B292 (1987) pp.59-92.

[5] E. Eichten *et al.* "Signatures for Technicolor". Physical Review D 34 (1986) p.1547.

[6] J.L. Hewett and T.G. Rizzo. "Leptoquark-boson Signals at e^+e^- Colliders". Physical Review D 36 (1987) p.3367.

[7] P.R. Harrison and C.H. Llewellyn Smith. "Hadroproduction of Supersymmetric Particles". Nuclear Physics B213 (1983) p.223.

[8] S.Dawson *et al.* "Search for Supersymmetric Particles in Hadron-Hadron Collisions". Physical Review D 31 (1985) p.1581.

[9] Vernon D. Barger and Roger J.N. Phillips. *Collider Physics.* Redwood City, California: Addison-Wesley Publishing Company, 1987, p. 159.

[10] H. Plothow-Besch. "Parton Density Functions". Proceedings of the 3rd Workshop on the Detector and Event Simulation in High Energy Physics, Amsterdam, 8-12 April 1991. and references therein.

[11] F.E. Page and S. D. Protopopescu. Brookhaven National Labratory Report No. BNL-37066, 1985, unpublished.

[12] J. Alitti *et al.* "A Search for Scalar Leptoquarks at the CERN $\bar{p}p$ collider". Physics Letters B 274 (1992) pp.507-512.

[13] G. Alexander *et al.* "A Search for Scalar Leptoquarks in Z° Decays". Physics Letters B 263 (1991) pp.123-134.

[14] B. Adeva *et al.* "Search for Leptoquarks in Z° Decays". Physics Letters B 261 (1991) pp.169-176.

[15] P. Abreu *et al.* "Search for scalar leptoquarks from Z° decays". Phys. Letters B 275 (1992) pp. 222-230.

[16] The ALEPH Collaboration. "Searches for new particles in Z decays using the ALEPH detector". Phys. Reports C 216 (1992) pp.253-340.

[17] Steven M. Moulding. "New Limits on Generation-1 Leptoquarks". Proceedings of the Division of Particles and Fields Meeting, Fermi National Accelerator Labrotory, Batavia, Il., Novenber 10-14, 1992.

[18] M. Derrick, *et al.* "Search for Leptoquarks with the ZEUS Detector". preprint DESY 93-017, March, 1993.

[19] I. Abt *et al.* "A search for leptoquarks, leptogluons, and excited leptons in H1 at HERA". Nuclear Physics B 396 (1993) pp. 3-23.

[20] S. Van der Meer. "Stochastic cooling and the accumulation of antiprotons". Rev. Mod. Phys., 57 (1985) p699.

[21] E. Oltman *et al.* "DØ Vertex Chamber Construction and Test Results". DØ note 1169, Fermilab, unpublished.

[22] A. R. Clark. "The DØ Vertex Chamber Status Report". Presented at the DØ Colaberation Meeting 17 November, 1988. D0 Note 776, Fermilab, unpublished.

[23] Jean-Francois Detoeuf *et al.* "The DØ Transition Radiation Detector". Nucl. Instr. and Meth. A265(1988) pp.157-166. and references therein.

[24] J.F.Detoeuf *et al.* "Status of the Transition Radiation Detector for the DØ Experement". Nucl. Instr. Meth. A279 (1989) pp.310-316.

[25] A. R. Clark *et al.* "The Central Tracking Detectors For DØ". Nucl. Instr. and Meth. A279 (1989) pp.243-248.

[26] D. Pizzuto. "DØ Central Tracking Chamber Performance Studies". Dissertation, State University of New York at Stony Brook, 1991.

[27] S. Rajagopalan. "The dE/dx Capabilities of the DØ Tracking System". Dissertation, Northwestern University, 1992.

[28] P. Grannis. "Specifications for the DØ Detector". DØ note 560, Fermilab, May 22, 1987, unpublished.

[29] M.L. Good *et al.* "Massless Gaps for the Central Calorimeter". DØ note 635, Fermilab, Nov. 20, 1987, unpublished.

[30] H. Aihara *et al.* "The Design, Construction, and Performance of the DØ End Calorimeter ElectroMagnetic Module". Nucl. Instr. and Meth. in Phys. A325 (1993) pp.393-416.

[31] Terece Louise Geld. "The DØ Intercryostat Detector: Design Considerations, Test Beam Studies and Initial Performance". Dissertation, The University of Michigan, 1993.

[32] R. D. Schamberger. "DØ Calorimeter Electronics". DØ note 1026, Fermilab, unpublished.

[33] M. Demarteau. "DØ Calorimeter Electronics Performance". Talk given at the International Conference on Calorimetry in High Energy Physics, Fermilab, Batavia, Il., Oct. 29-Nov. 1, 1990. D0note 1087, Fermilab, unpublished.

[34] "SAMUS - Small Angle Muon Spectrometers, Design and Status". Institute of High Energy Physics, Serpukhov. DØ note 768, Fermilab, Sept. 29, 1988, unpublished.

[35] C. Brown *et al.* "DØ Muon System With Proportional Drift Tube Chambers". Nucl. Instr. and Meth. A279(1989) pp.331-338

[36] T.Diehl. "Milestones Passed in CRC II - WAMUS Triggering and Tracking". DØ note 1365, Fermilab, February 13, 1992, unpublished.

[37] D. Denisov. "Small Angle Muon System for the DØ Detector at Fermilab". DØ note 1367, Fermilab, Feb. 13, 1992, unpublished.

[38] R. Partridge. "The Level 0 Trigger". DØ note 1218, Fermilab, Oct. 1, 1991, unpublished.

[39] K. McFarland. "Design and Testing of a Calibration System for the Level-0 Trigger at DØ". DØ note 840, Fermilab, unpublished.

[40] S. Abachi *et al.* "Beam Tests of the DØ Uranium Liquid Argon End Calorimeters". NIM A 324 (1993) pp.53-76.

[41] M. Fatyga. "Load 2 status report". DØ note 1371, Fermilab, Feb. 13, 1992, unpublished.

[42] Marc Paterno, Dhiman Chakraborty, Mirek Fatyga. "CCEM Module Sampling fractions and Uniformity of Response". DØ note 1375, Fermilab, May 4, 1992, unpublished.

[43] W.G.D.Dharmaratna. "CCEM Responce vs η – Test Beam Load2". DØ note 1577, Fermilab, December 1, 1992, unpublished.

[44] Sarah Joy Durston. "A Study of Electromagnetic and Hadronic Shower Shapes and Position Resolution, and the Jet Energy Response of the D-Zero Calorimeter". Dissertation, University of Rochester, 1993.

[45] R. Engelmann *et al.* Nucl. Instr. and Meth. 216 (1983) p.45.

[46] Jonathan Kotcher. "Response of the DØ Calorimeter to Cosmic Ray Muons". Dissertation, New York University, October, 1992.

[47] Ulrich Heintz, private communications.

[48] R. Hirosky. " The Response of the D-Zero Central Calorimeter to Electrons and Pions from 2 through 150 GeV/c". DØ Note 1499, Fermilab, March 29, 1993, unpublished.

[49] J. Guida. "The DØ Calorimeter Trigger". Proceedings of The Third International Conference on Calorimetery in High Energy Physics, Sept. 29 - Oct. 2, 1992 at Corpus Chisti, Tx.

[50] M. Abolins, D. Edmunds, P. Laurens, J. Linnemann, and B. Pi. "The Level One Calorimeter Trigger for DØ". DØ note 706, Fermilab, Oct. 25, 1988, unpublished.

[51] M. Abolins, D. Edmunds, P. Laurens and B. Pi. "The Fast trigger for the DØ Experiment". Nucl. Instr. and Meth. in Phys. Research A289 (1990) pp.543-560.

[52] Philippe Laurens, private communications.

[53] J. Mckinley and J. Linnemann. "Description of the Level 2 Electromagnetic Filter Algorithm and Study of the Effects of Shower Generation Method, Zero Suppresion, and Event Generation Methos on the Level 2 Electromagnetic Filter for DØ". DØ note 1354, Fermilab, January 20, 1992, unpublished.

[54] Richard Vincent Astur. "A Study of the Ability of the DØ Detector to Measure the Single Jet Inclusive Cross Section". Dissertation, Michigan State University, 1992.

[55] Amber Boehnline. "Changes Made to L2ETMISS and L2ETSUM During Run Ia". DØ note 1664, Fermilab, March 29, 1993, unpublished.

[56] John M. Butler. "Main Ring Deadtime". DØ note 1682, Fermilab, February 28, 1993, unpublished.

[57] T.C. Awes *et al.* "A Simple Method of Shower Localization and Identification in Laterally Segmented Calorimeters". Nucl. Instr. Meth. A311 (1992) pp.130-138.

[58] R. Raja, private communications.

[59] M. Narain, private communications.

[60] N.J. Hadley. "Cone Algorithm for Jet Finding". DØ note 904, Fermilab, November 29, 1989, unpublished.

[61] Richard V. Astur, John Borders, David Cullen-Vidal, Andrew Milder. "Determining the Jet Energy Scale Using Test Beam". DØ note 1683, Fermilab, March 11, 1993, unpublished.

[62] Chip Stewart. "Jets in the DØ Calorimeter". Proceedings of The Third International Conference on Calorimetery in High Energy Physics, Sept. 29 - Oct. 2, 1992 at Corpus Chisti, Tx.

[63] Marc Paterno. "A Study of the DØ Calorimeter $\not{E}_T$ Resolution Using Low E_t Jet Triggers". DØ note 1782, Fermilab, July 13, 1993, unpublished.

[64] G. Marchesini and B. R. Webber. Nucl. Phys. B310 (1988) p.461.

[65] I. Hinchliffe, private communications.

[66] H. U. Bengtsson, T. Sjostrand, Computer Phys. Comm. 46 (1987) p.43.

[67] R. Brun and F. Carminati. "GEANT Detector Description and Simulation Tool". Cern, Cern Program Library Long Writeup W5013, July, 1993.

[68] Norman Amos, private communications.

[69] R.D. Cousins and V.L. Highland. "Incorporating systematic uncertainties into the upper limit". Nucl. Instr. and Meth. A 320 (1992) pp.331-335.

[70] Nick Hadley, private communications.

[71] M. Fatyga, and Dhiman Chakraborty. "QCD backgrounds to electroweak signals. A study of fake electron and fake photon probability". DØ note 1753, Fermilab, unpublished.

[72] Mirek Fatyga, private communications

[73] F. Abe *et al.* "Measurement of Jet Multiplicity in W Events Produced in $p\bar{p}$ Collisions at $\sqrt{s} = 1.8$ TeV". Physical Review Letters 70 (1993) pp.4042-4046.

[74] F.A. Berends, H. Kuijf, B. Tausk, and W.T. Giele. "On the Production of a W and Jets at Hadron Colliders". Nucl. Physics B357 (1991) pp.32-64.

[75] Marc De Montigny and Luc Marleau. "Pair production of leptoquark scalars in hadron colliders". Can. J. Phys. 68 (1990) pp.612-619.

[76] F. James, M. Roos, CERN Computer Centre Program Library D506.

[77] R.K. Bock *et al.* "Parameterization of the Longitudinal Showers in Sampling Calorimeters". Nucl. Instr. and Meth. 186 (1981) pp.533-539.

[78] M. De Palma *et al.* "Measurement, Parameterization, and Fast Simulation of Hadronic Showers in Lead". Nucl. Instr. and Meth. 219 (1984) pp.87-96.